Universidad
Carlos III de Madrid

PhD Thesis

DEVELOPMENT OF PHOTONIC INTEGRATED CIRCUIT TECHNIQUES FOR WIDELY TUNABLE MID-IR SOURCES BASED ON QUANTUM CASCADE LASERS

Author: Luis Jorge Orbe Nava

Director: Dr. Guillermo Carpintero del Barrio

DEPARTMENT OF ELECTRONIC TECHNOLOGY

Leganés, November 2015

Universidad Carlos III de Madrid

TESIS DOCTORAL

DEVELOPMENT OF PHOTONIC INTEGRATED CIRCUIT TECHNIQUES FOR WIDELY TUNABLE MID-IR SOURCES BASED ON QUANTUM CASCADE LASERS

Autor: D. Luis Jorge Orbe Nava

Director: Dr. Guillermo Carpintero del Barrio

DEPARTAMENTO DE TECNOLOGÍA ELECTRÓNICA

Leganés, Noviembre de 2015

TESIS DOCTORAL

DEVELOPMENT OF PHOTONIC INTEGRATED CIRCUIT TECHNIQUES FOR WIDELY TUNABLE MID-IR SOURCES BASED ON QUANTUM CASCADE LASERS

Autor: Luis Jorge Orbe Nava

Director: Prof. Dr. D Guillermo Carpintero del Barrio

Firma Del Tribunal Calificador

Presidente: Tadao Nagatsuma _____

Vocal: Sebastian Lourdudoss _____

Secretario: Horacio Lamela _____

Calificación:

_____

En Leganés, a ____ de _____ 2015

Este documento es el resultado de 6 años de trabajo, experiencias e innumerables emociones que tranquilamente podrían merecer su propio texto.

No es hasta el momento en que te sientas a escribir estas líneas en que te das cuenta de la cantidad de factores y actores que forman parte de su desarrollo, no escribiéndola (que se agradecería bastante) pero sí estando alrededor durante su proceso.

Lo dicho, la cantidad de actores es mucha y sus aportaciones varias. Con algunos he compartido infinidad de cañas, tercios, jarras y pintas, mientras con otros no más que alguna que otra conversación a las 5 de la mañana cualquier día de la semana en la que por enésima vez no podía dormir.

A todos ellos GRACIAS.

Gracias también a Guillermo, que lo que ha tenido es paciencia. A Julio, que al fin ya borró la imagen que siempre ponía en su pantalla cuando tenía que fingir que trabajaba. A Robinson, que se tuvo que comer mi regaño aquella vez que no aparecí a cuidar examen. Al otro Guillermo, que todo lo sabe. A Luca por compartir su filosofía de vida basada en reguetón. A Daniel, jefe de laboratorios, por las historias donde denota paciencia con su alumnado. A la gente del MIOLog, que redefinió lo que es una fiesta. Al Xuxe y a Xuxín, por dejar claro que en Panamá la vida es más sabrosa.

Y a los más importantes…

A mis padres y a Diana… mi compañera de viaje

Resumen

En los últimos años, la fotónica en rangos de frecuencia del infrarrojo medio ha recibido renovado interés para una gran variedad de aplicaciones. Esta región del espectro electromagnético presenta una serie de retos desde el punto de vista tecnológico, ya que las fuentes de luz que trabajan en ella presentan una limitada capacidad de sintonización sin el uso de sistemas complejos.

En consecuencia, los esfuerzos de miniaturización que permitan el desarrollo de fuentes de luz ampliamente sintonizables en el infrarrojo medio son extensamente discutidas, ya que el desarrollo de esos productos consiste en dispositivos independientes, tales como fuentes de luz y componentes pasivos, que son ensamblados y por tanto presentan limitaciones individuales y cuellos de botella que limitan un mayor desarrollo de esas tecnologías.

Los láseres de cascada cuántica son, desde el punto de vista de la óptica, una de las formas más comunes de generar luz infrarroja. Sus propiedades tales como su alta integrabilidad, operación en temperatura ambiente y reducido costo, los convierten en grandes opciones tecnológicas para integrar nuevos sistemas. Sin embargo, la limitada capacidad de sintonización de los mismos requiere la introducción de fases adicionales de multiplexado para generar dispositivos de una sola salida capaces de combinar múltiples fuentes de luz.

La presente tesis investiga el diseño y la caracterización de funciones ópticas pasivas basadas en plataformas de InP/InGaAs para el desarrollo de multiplexores ópticos para el rango de longitudes de onda de 7 – 10 μm.

Este trabajo es descrito en una serie de pasos lógicos, iniciando con la descripción de funciones ópticas básicas y un análisis de guías de onda que permite identificar los parámetros de diseño más importantes en guías de onda rectas y curvas, tales como el ancho, profundidad de guía y radio mínimo de curvatura. Al simular distintas combinaciones de valores para esos parámetros hemos estudiado el comportamiento modal y las características de pérdidas en función de la longitud de onda.

Basado en esos resultados, el primer enfoque ha sido el desarrollo y simulación de estructuras basadas en uniones en Y. Sin embargo, estas presentan una gran superficie, limitando su escalabilidad y aumentando las pérdidas de propagación asociadas, ya que el tamaño y el número de ramificaciones involucradas aumenta en función del número de láseres que se desean multiplexar.

Un segundo enfoque propuesto, basado en estructuras de rejilla (del inglés *grating*) del tipo Echelle, presenta menor superficie y mejor escalabilidad. Del mismo modo, se ha diseñado un esquema dual de estos dispositivos con el objetivo de mejorar aún más características como la interferencia entre canales y reducir el área total del dispositivo al dividir el número de entradas a multiplexar entre los distintos "subdiseños" que son después acoplados en una sola guía de onda de salida.

Los resultados de la fabricación de estas funciones ópticas y *Building Blocks* corresponden con los resultados de la fase de diseño y simulación, confirmando la viabilidad de una plataforma basada en InP/InGaAs para la fabricación de bloques de funciones fotónicas operando en longitudes de onda en el infrarrojo medio. La caracterización de estos

multiplexores ópticos basados en Echelle *gratings* demuestra el potencial de integración monolítica de funciones ópticas pasivas y fuentes de luz láser en un mismo dispositivo.

Abstract

In the last years, mid-infrared photonics has received renewed interest for a variety of applications. This spectral region provides a series of challenges from the technological point of view as light sources working in this span present limited wavelength tunability without the use of complex systems.

Consequently, miniaturization efforts allowing for the development of widely tunable mid-infrared sources are extensively discussed, as product development consists of separated mechanisms, such as light sources and passive components that are put together and therefore present individual limitations and bottlenecks that hinder the further development of these technologies.

Quantum Cascade Laser diodes are, from the optics point of view, one of the most common ways to generate mid-infrared light. Their properties, such as high integrability, operation at room temperature and reduced cost make them good technologies to implement in new systems. However, the limited tunability characteristics of these devices require the introduction of additional multiplexing stages in order to generate a single output device from the combination of several light sources.

The present thesis investigates the design and characterization of InP/InGaAs passive optical functions for the development of multiplexer structures for the 7 – 10 μm wavelength range.

This work is described in a series of logical steps, starting with the description of basic passive optical functions and a waveguiding analysis that allows for the identification of the most important design parameters in straight and bent waveguides, such as waveguide width, etching depth and minimum bending radius. By simulating different combination of those parameters, we have studied the modal behavior and loss characteristics as a function of the injected wavelength.

Based on those results, Y-junction based structures are designed and simulated as a first approach. However, they present large footprint areas, limiting their scalability and increasing propagation losses, as the size and number of ramifications increase as a function of the number of lasers to combine.

A second approach, based on Echelle grating structures, is proposed as an alternative, presenting smaller footprints and better scalability. A dual Echelle grating multiplexer was designed in order to further improve the channel crosstalk and crossing levels, with the added objective of reducing the footprint in these multiplexer schemes by dividing the number of multiplexed inputs into multiple subdesigns which are later coupled into a single waveguide output.

Results for the fabricated optical functions and basic Building Blocks are in agreement with the design and simulation results, confirming the feasibility of an InP/InGaAs epilayer structure to fabricate photonic building blocks to operate in the mid-infrared range. The characterization of the Echelle grating based multiplexers demonstrates the potential to monolithically integrate light generation and passive optical functions with an individual device. Despite having high insertion losses, a comprehensive review allows for better

understanding of the device and suggests solutions for further improvements in the development of grating based mid-infrared multiplexers.

Nomenclature

Symbols

∂x ∂y ∂z	Partial differentiators as a function of an axis
B	Magnetic flux density
c	Phase velocity of a wavelength through a medium with a refractive index n
c_0	Speed of light at vaccum; $c_0 = 299\,792\,458\ m/s$
D	Electric flux density
d	Width of the propagation area of a light wave (core width)
E	Electric field
H	Magnetic field
J	Current density
k	Propagation constant; $\alpha + i\beta$
k0	Propagation constant at vacuum; $k_0 = 2\pi/\lambda$
M	Number of modes
MTE	TE mode
MTM	TM mode
n	Refractive index of the medium
ñ	Complex refraction index; $\tilde{n} = n(\omega) + i\kappa(\omega)$
n(ω)	Real part of the complex refraction index as a function of the angular speed of the wavelength
NA	Numerical aperture
û	Unitary vector $\hat{u} = \hat{u}_x + \hat{u}_y + \hat{u}_z$
α(ω)	Absorption coefficient
β	Propagation constant of a mode

Δx Δy Δz	Spatial steps as over an axis
ε	Electric permittivity for a specific material
ε0	Electric permittivity at vacuum; $\varepsilon_0 = 8.85x10^{-12}$
θm	Incidence angle of the light wave mode
κ(ω)	Imaginary part of the complex refraction index as a function of the angular speed of the wavelength
λ	Wavelength at a medium with a refractive index n
λ0	Wavelength at vaccum
μ	Magnetic permeability for a specific material
μ0	Magnetic permeability at vacuum; $\mu_0 = 4\pi x10^{-7}$
ω	Angular speed
ω0	Angular speed of the wavelength at vaccum

Acronyms

APCI	Atmospheric-Pressure-Chemical-Ionization
BB	Building Block
BPM	Beam Propagation Method
DBR	Distributed Bragg Reflector
DFB	Distributed FeedBack
DFB-QCL	Distributed FeedBack Quantum Cascade Laser
DMS	Differential Mobility Spectrometry
EC	External Cavity
EC-QCL	External Cavity Quantum Cascade Laser
FDTD	Finite-Difference Time-Domain
FMM	Film Mode Matching
FPR	Free Propagation Region
FTIR	Fourier Transform Infrared
FWHM	Full-Width Half-Maximum
InGaAs	Indium Gallium Arsenide
InP	Indium Phosphide
IR	InfraRed
MIR	Mid-infrared
MIRIFISENS	Mid InfraRed Innovative lasers For Improved SENsor of hazardous Substances
MPW	Multi-Project Wafer
NIR	Near InfraRed
PIC	Photonic Integrated Circuit
PML	Polymer Multi-Layer
QCL	Quantum Cascade Laser
TDL	Tunable Diode Laser
TDLAS	Tunable Diode Laser Absorption Spectroscopy
TE	Transverse Electric
TEM	Transverse ElectroMagnetic
TM	Transverse Magnetic

Index

Introduction

1.1 - Motivation

The mid-infrared (MIR) region is emerging as the favorite wavelength band for a number of applications, including high sensitivity trace detection [1] [2] . This region span from 2.5 to 25 μm[3] and its importance arises from the fact that photon energies associated with this part of the infrared are below the level to excite individual electrons in chemical compounds (it is not an ionizing radiation), while it is able to induce vibrational excitation of covalently bonded atoms and complex molecules, causing the molecule to absorb part of the energy of the light source allowing the identification of the molecules [5] [6] .Virtually all organic compounds will absorb infrared radiation that corresponds in energy to these vibrations[7] . The exact frequency at which a given absorption occurs is determined by the strengths of the bonds involved in the mass of the component atoms and there are not always exclusive, which means that a molecule could present multiple or a large range of these frequencies [6] .

MIR detection takes advantage of this effect by detecting absorption frequencies that are a unique reflection of the molecular structure of complex substances and compounds, allowing for their identification [6] [8] . The absorption spectrum for a specific substance is called fingerprint, Figure 1.1 shows an example fingerprint of an organic compound. The devices used for this detection scheme are called absorption spectroscopes [9] .

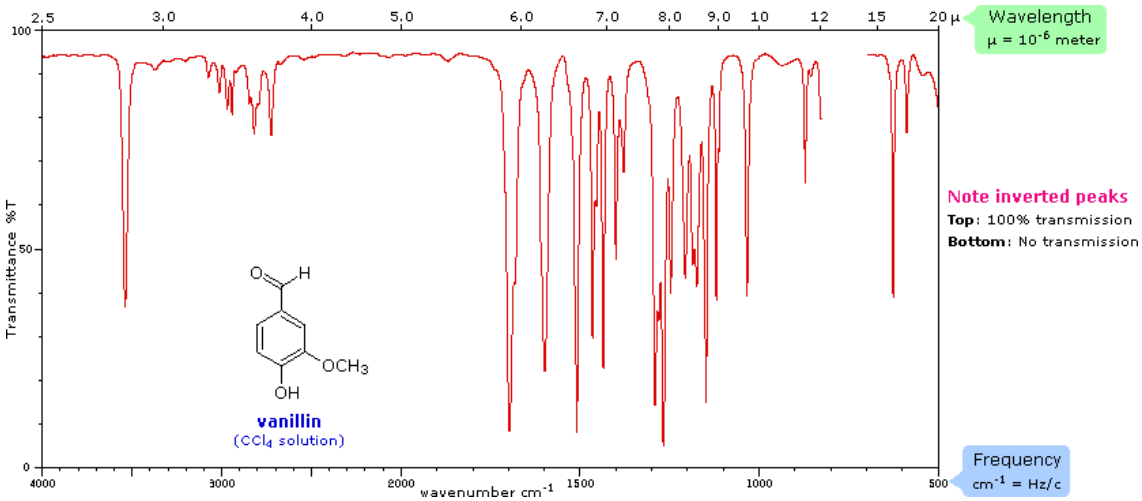

Figure 1.1. Example of an organic compound absorption spectra (fingerprint)

MIR absorption spectroscopes principle is to guide light through a compound sample and compare the resulting absorption spectrum against a reference, containing no sample [9] . The objective is to process the spectral differences between the sample and the references in order to identify the compounds. A basic scheme of an infrared spectroscope is shown in Figure 1.2.

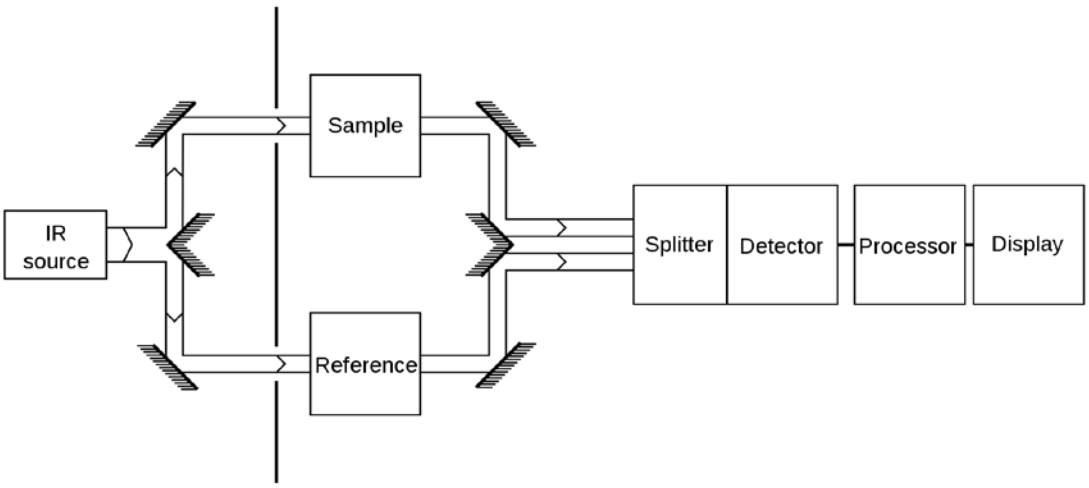

Figure 1.2. Basic block diagram for an IR spectroscope

With the correct wavelength source, these sensing technologies allow to identify the absorption characteristics for different substances. An example of multiple sensing of complex organic molecules is shown in Figure 1.3. In addition to the concentration, it is also possible to determine the temperature, pressure, velocity and mass flux of the gas under observation [1] [2] [10] .

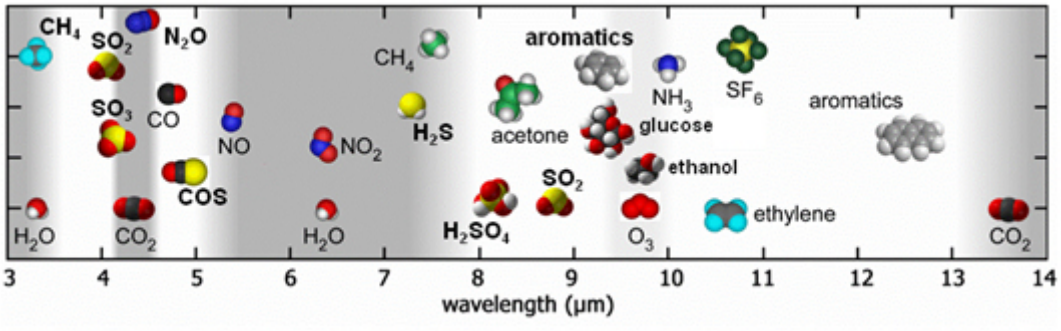

Figure 1.3. Graphical representation of the location of strong absorptions of complex molecules in the infrared range

The performance of these sensing technologies is limited primarily by the wavelength quality and generated power of the IR source. There are different kinds of MIR sources, (Figure 1.4a), each one of them with their own characteristics of size, stability and operational mode, which can be continuous wave (CW) or pulsed.

Among those technologies, the use of semiconductor laser sources in the form of Tunable Diode Lasers (TDLs) is the most used approach because of their size, cost and integration capabilities, despite the similarity in wavelength ranges in comparison with other technologies (Figure 1.4b)[8] , as other different MIR generation approaches require external complex control instrumentation.

Quantum Cascade Lasers (QCLs) are laser sources capable of IR light emission. There are semiconductor sources based on resonant tunneling and optical transitions between electronic levels within the conduction band of a multi-quantum well structure [11] ; this allows for a wide spectral range and the possibility of single-mode design in the form of Distributed Feedback (DFB) lasers with emission wavelengths as short as 2.5 µm and ranging up to 250 µm without any external effort to improve such range[12] . They are favored over other similar TDLs, such as interband cascade lasers (ICLs) given their increased quantum efficiency, which leads to higher output powers [11] .

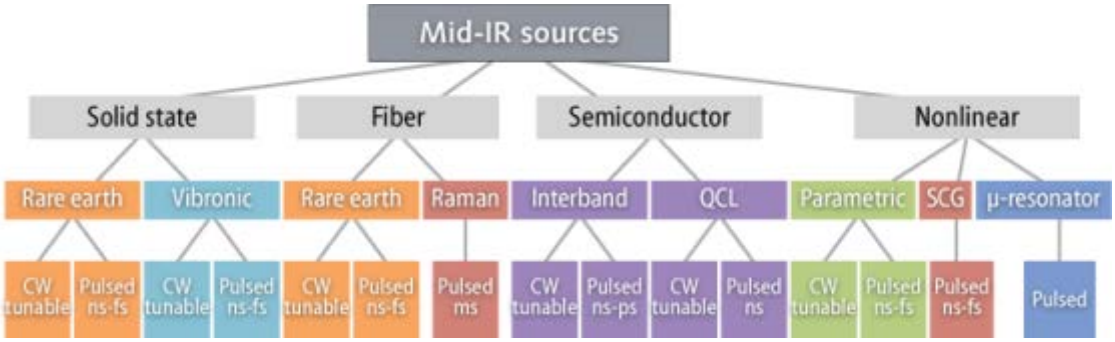

(a)

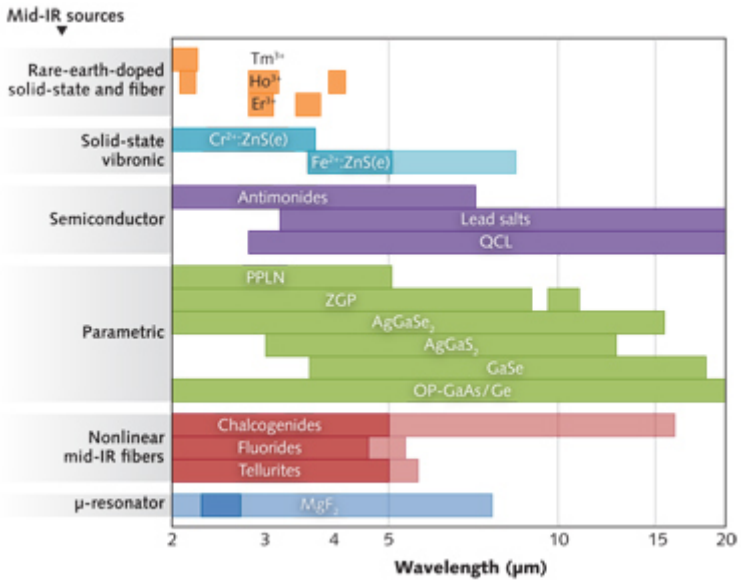

(b)

Figure 1.4. MIR sources division by technology (a). MIR wavelength range comparison between different technologies (b)

However, crucial bottlenecks hindering the further development of this technology exist in the range of tunability, as individual laser sources in the MIR region can only be tuned on a limited range by heating the laser with a DC bias current or by changing the heatsink temperature [13] . Also, single-mode emission is required for most applications.

In order to be able to implement MIR-QCL sources along with absorption spectrometers, QCL material is processed into external cavity (EC) DFB lasers [14] [15] [16] or in the form of DFB-QCL arrays, composed by a large number of individual lasers[13] [17] .

External cavity quantum cascade lasers (EC-QCLs) offer the possibility of widely tunable ranges, but they are very complex to build as they require high quality antireflection coatings, well-aligned external optical components, including a grating for tuning, and piezoelectric controllers (Figure 1.5)[18] .

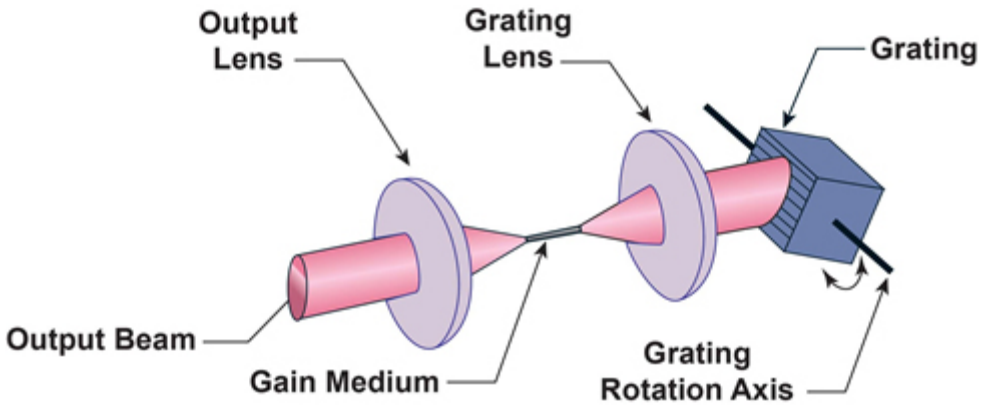

Figure 1.5. EC-QCL design

The application of an EC configuration allowed selection of the QCL wavelength anywhere within the available QCL spectral gain without changing the chip temperature, as they cannot be implemented along with other photonic circuits in the same chip, which

significantly increased the laser spectral coverage and allowed much more efficient utilization of the available QCL spectral gain[13] [14] [15] [16] . Figure 1.6 shows the tuning range advances over time for this technology [19] .

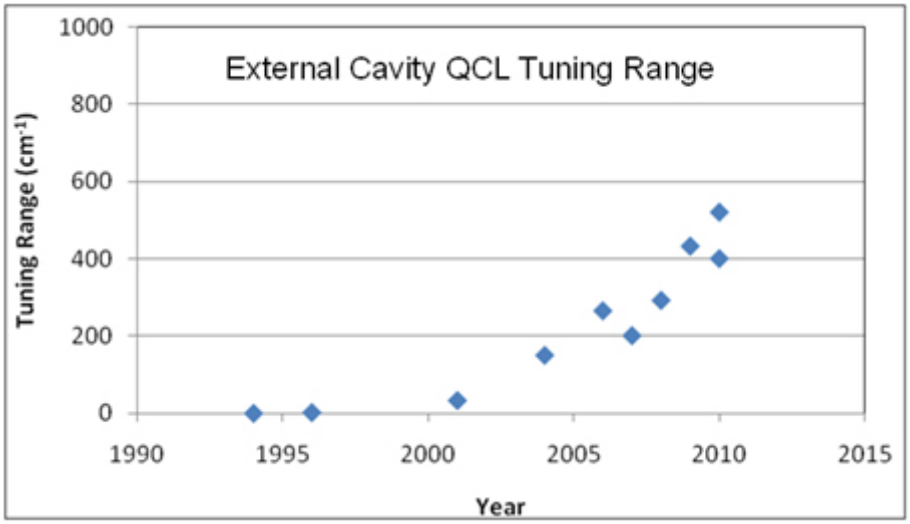

Figure 1.6. Graph of literature values of EC-QCL tuning ranges over time

A different approach on the design of widely tunable MIR sources is the implementation of multiple DFB-QCL arrays. These arrays are design so that adjacent lasers share part of their spectrum and quasi-continuous tunability can be achieved by selectively activating individual lasers [20] . A basic array configuration can be seen in Figure 1.7.

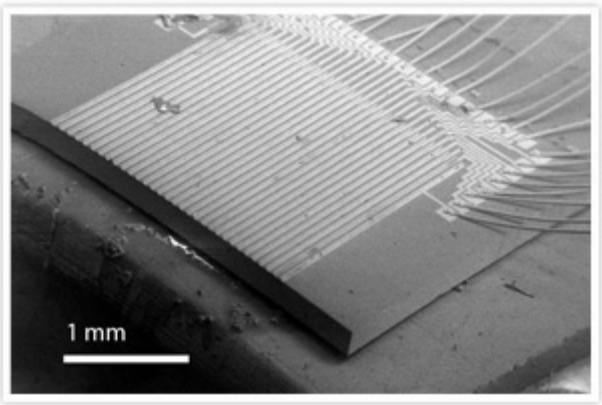

Figure 1.7. Scanning Electron Microscope (SEM) image of a DFB-QCL array

This configuration has size advantages over EC-QCLs and also offers the possibility of monolithic integration along with other photonic circuits. The range of tunability is limited by the number of lasers and the individual tuning range for each DFB-QCL [12] [21] .

In order for DFB-QCL arrays to work as a widely tunable MIR source, further effort is necessary to multiplex all the lasers into a single output, and therefore be conformed into a Photonic Integrated Circuit (PIC)[22] [23] [24] .

This approach has already been proved into Indium Phosphide platforms in the Near Infrared (NIR) for 1.5 μm wavelengths [25] . However, recent efforts report smaller tunability ranges to in comparison to the ones achieved with the use of EC-QCLs.

1.2 - Objectives and original contributions

The FP7-MIRIFISENS (Mid InfraRed Innovative lasers For Improved SENsor of hazardous Substances) project proposes a solution with the design of a widely tunable monolithically integrated MIR-QCL source for its use in spectroscopy applications in selected wavelength ranges.

The design of this source conjugates the use of a DFB-QCL array along with a multiplexer stage. The combination of the individual lasers is proposed by the use of

photonic functions or Building Blocks (BB), in the form of a multiplexer function to conform a monolithic tunable source with a single output.

The operation wavelengths of these monolithic tunable sources are to be divided into two different ranges:

- 7.00 – 8.50 μm (1176.5 – 1428 cm^{-1})
- 7.00 to 10.00 μm (1000 - 1428 cm^{-1})

Based on those wavelength requirements, the first step is to complete a waveguide analysis in order to obtain the valid values and optimize basic design parameters. Taking those results as base, optical functions are defined along with their BB parameters for characterization efforts.

These BB are developed by using a passive epitaxy provided by III-V Lab, which is optimized for monolithic integration (active + passive), and are defined by their input and output parameters.

In the same design effort, a series of (de)multiplexer structures are proposed in two different configurations: Y-junction based and Echelle grating (de)multiplexers, which should comply with the wavelength range requirements as mentioned. Sample designs were fabricated using the same epitaxy and their characterization efforts are presented and studied.

The main objectives of this work can be enumerated as follows:

- Development of a waveguiding analysis procedure to obtain basic design parameters for straight and bent waveguides capable of guiding MIR light in the 7-10 μm range.
- Determination of necessary design parameters for complex building block design and optimization of each design into a building block.
- Elaboration of design proposals for multiplexer structures based on the previously parameterized building blocks and the project objectives.
- Experimental characterization of all the building blocks and multiplexer structures.

The completion of these objectives should prove the practicability of BB based multiplexer design in the MIR for a comparative experimental analysis between two different (de)multiplexing approaches: a Y-junction based and a Rowland based Echelle grating structures.

The experimental results detailed in this work will demonstrate the feasibility of combining light sources and passive multiplexing to achieve broadband tunability in InP platforms.

1.3 - Outline

The structure of this work is presented as follows:

There are two main blocks clearly differentiated in this work: first a design approach is proposed and supported by simulations for the different BBs, starting with an introduction to the design platform and concluding with the simulation of two different multiplexer schemes. The second block presents the experimental results of the previously detailed designs, as well as their integration capabilities along with laser light sources.

In more detail, in Chapter 2, an introduction to the MIRIFISENS project and III-V Lab platform is made, along with a proposal for basic optical functions, and their redefinition as Building Blocks. The simulation results for those basic optical functions are presented and the basis for more complex designs is set.

Chapter 3 takes those basic designs into the definition of Y-Junction and Echelle grating based multiplexer structures. Following the same pattern as Chapter 2, the different designs are redefined as building blocks in complain with the project needs. A series of simulation results are presented for all the proposed designs.

One step further, in Chapter 4, an overview of the project fabrication procedure is presented along with the mask design including all the aforementioned structure designs. After that, a brief description of the experimental setup is briefly described as the first step

to the presentation of the results for the characterization efforts over the multiplexer samples.

Finally, Chapter 5 presents the conclusions of the Thesis and proposes the future working lines.

1.4 - References

[1] Cassidy, D. T.; Reid, J.; "Atmospheric pressure monitoring of trace gases using tunable diode lasers," Appl. Opt. 21(7), 1185–1190 (1982)

[2] Werle, P.; Slemr, F.;Maurer, K.; Kormann, R.; Mucke, R.; Janker, B.; "Near- and mid-infrared laser-optical sensors for gas analysis," Opt. Las. Eng. 37(2–3), 101–114 (2002)

[3] Imanaka, H.; et al; “Optical constants of Titan tholins at mid-infrared wavelengths (2.5–25 μm) and the possible chemical nature of Titan’s haze particles”

[4] Kosterev, A.; Tittel, F.; "Chemical sensors based on quantum cascade lasers," IEEE J. Quantum Electron. 38, 582 (2002)

[5] Belkin, M. A.; Loncar, M.; Lee, B. G.; Pflügl, C.; Audet, R.; Diehl, L.; Capasso, F.; Bour, D.; Corzine, S.; Höfler, G.; “Intra-cavity absorption spectroscopy with a narrow-ridge microfluidic quantum cascade laser,” Opt. Express 15, 11262 (2007)

[6] Reusch, W.; "Infrared Spectroscopy"; Michigan State University, Chem Ed. 2013

[7] Tsai, T. R., Rose, R. A., Weidmann, D. & Wysocki, G. Atmospheric vertical profiles of O3, N2O, CH4, CCl2F2, and H2O retrieved from external-cavity quantum-cascade laser heterodyne radiometer measurements. Appl. Opt. 51, 8779-8792 (2012).

[8] Curl, R. F. et al. Quantum cascade lasers in chemical physics. Chem Phys Lett 487, 1-18 (2010).

[9] Wang, Y., Wysocki, G. a., Lyon, S. c. m., Gmachl, C. c. m. & Wysocki, G. c. m. Development of Novel Mid-Infrared Spectrometers Based on Quantum Cascade Lasers, Princeton University, (2014).

[10] Herrmann, Karin. "Tunable Diode Laser Spectroscopy." 1995

[11] Faist, J.; et al; "Quantum cascade laser". Science, Vol. 264, No. 5158, pg. 553, 22 Apr (1994)

[12] J. Faist, et al, "Distributed feedback quantum cascade laser", APL 70, 2670 (1997)

[13] Gmachl, C., et al., "Single-Mode Tunable Distributed-Feedback and Multiple-Wavelength Quantum cascade lasers," IEEE J. Quant. Elec., 38 (6), pg. 569 (2002)

[14] R. Maulini, A. Mohan, M. Giovannini, J. Faist, and E. Gini, Appl. Phys. Lett. 88, 201113 (2006)".

[15] G. Wysocki, R. F. Curl, F. K. Tittel, R. Maulini, J. M. Bulliard, and J. Faist, Appl. Phys. B: Lasers Opt. 81, 769 (2005)".

[16] R. Maulini, M. Beck, J. Faist, and E. Gini, Appl. Phys. Lett. 84, 1659 (2004)".

[17] Wittmann, M. Giovannini, J. Faist, L. Hvozdara, S. Blaser, D. Hofstetter, and E. Gini, Appl. Phys. Lett. 89, 141116 (2006)"

[18] Hugi, A., et al.,"External Cavity Quantum cascade laser Tunable from 7.6 to 11.4 μm", Appl. Phys. Lett., 95, pg. 061103 (2009).

[19] “Luo, G.P., et al., "Grating-Tuned External-Cavity Quantum-Cascade Semiconductor Lasers,” Appl. Phys. Lett., 78, pg. 2834 (2001).

[20] Lee, Benjamin G., et al, "Broadband Distributed-Feedback Quantum Cascade Laser Array Operating From 8.0 to 9.8 \mu m" Photonics Technology Letters, IEEE , vol.21, no.13, pp.914,916, July1, (2009)

[21] Carras, M.; et al; "Advances toward monolithic broadly-tunable QCL sources," Proc. SPIE 8993 (2014)

[22] L. J. Orbe, G. Carpintero, C. Gilles, F. Boulila, G. Maisons, M. Carras, "Characterization of an InGaAs/InP-based Echelle Mirror Multiplexer for Widely Tunable Mid-IR Sources Based on Quantum Cascade Lasers," SPIE Photonics West (2015)

[23] L. J. Orbe, G. Carpintero, G. Maisons, C. Gilles, F. Boulila, M. Carras, "MIR Photonic Integrated Circuits for Laser Spectroscopy," MIOMD (2014)

[24] L. J. Orbe, G. Carpintero, G. Maisons, M. Carras, "QCL-based photonic integrated circuits on InP and other platforms," IPRM (2014)

[25] Kuindersma, P.I.; Leijtens, X.J.M.; van Zantvoort, J.H.C.; de Waardt, H., "A dual purpose, all optical multiplexer circuit in InP: Muxing clock and data, and transmultiplexing WDM to TDM," in Optical Communications (ECOC), 2012 38th European Conference and Exhibition on , vol., no., pp.1-3, 16-20 Sept. 2012

Analysis, Design, and Simulation of Passive Optical Functions for Optical Integration

2.1 - Optical integration technologies

Photonics and its uses are rapidly growing across many application areas. The European Commission has stated that around 18% of world photonics production is based on European research, with outstanding developments in communications, lighting, medical applications, laser-based manufacturing and safety & security applications. Given the potential of photonics to enhance innovation across several industries, it has been recognized as one of Europe's Key Enabling Technologies (KETs) of the 21st Century [1] [2] .

Advances of optoelectronic materials and devices have played a critical role in this development. Optoelectronic materials and devices make it possible to drastically expand the wavelength range and sensitivities of optical sensors. Discoveries and advances have been made in active materials over a wide wavelength range, with high quantum efficiencies spanning the UV to the far IR [3] [4] [5] [6] [7] .

Nanoscale processing technologies are being developed to facilitate the engineering of optical properties by effects due to the quantization of electron or optical wavelengths. Finally, remarkable progress on the integration of dissimilar materials for new applications has been made.

In general, the concept of integrated optics[8] [9] has been included in this development, hoping to partially replicate the remarkable progress that photonics in general

has seen, including reductions in cost and size, as well as increased performance and reliability

Integrated optics [10] [11] is defined as the technology and techniques of integrating various optical devices and components for the generation, focusing, splitting, combining, isolation, polarization, coupling, switching, modulation and detection of light, all on a single substrate. A photonic integrated circuit (PIC) or integrated optical circuit is a semiconductor chip in which multiple photonic functions are integrated providing signal processing functionalities on the optical domain. However, even though we can find numerous efforts in photonic integration in the range from 1200 to 1650 nm as well as in the Near Infrared (NIR), from 0.8 to 2.5 μm[5] [13] , limited effort has been reported in the important mid-infrared (MIR) range and longer waveguides given the difficulties that light generation over those wavelengths present[5] .

So far, light generation in the MIR has been achieved with multiple technologies with the development of InP and GaSb based semiconductor sources emitting in the wavelength range from 2.5 μm to 25 μm[13] [14] , however, the possibility of photonic integration is only coped with the development of ICLs and QCLs, as mentioned in Chapter I, and the usual approach for this is via butt-coupling schemes, which introduce external alignment and dispersion losses[15] , as the light generation circuit has to be aligned to match the passive waveguides Figure 2.4(left).

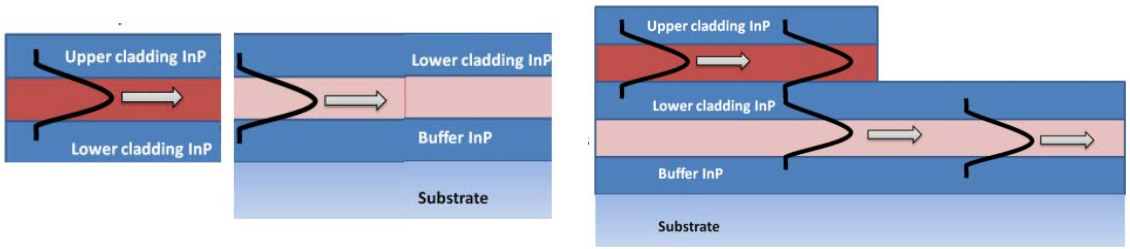

Figure 2.1. Butt-coupling integration scheme (left) and monolithic integration scheme (right)

In order to improve photonic integration, the development of platforms composed by both active and passive regions in the same wafer can be achieved by the use of vertical couplers (Figure 2.3)[16] , which guide the light from the active region (the top layers) to the lower layers, containing the passive waveguides Figure 2.4(right). This design scheme offers the opportunity to apply miniaturization efforts and considerably reduce the overall device footprint, as well as costly optical interconnections. The increased reliability (as the laser source needs no external alignment) eliminates additional losses due to diffraction angle, which is a function of the wavelength (Figure 2.2), as there is no space between the laser source and the waveguides[5] [17] [18] .

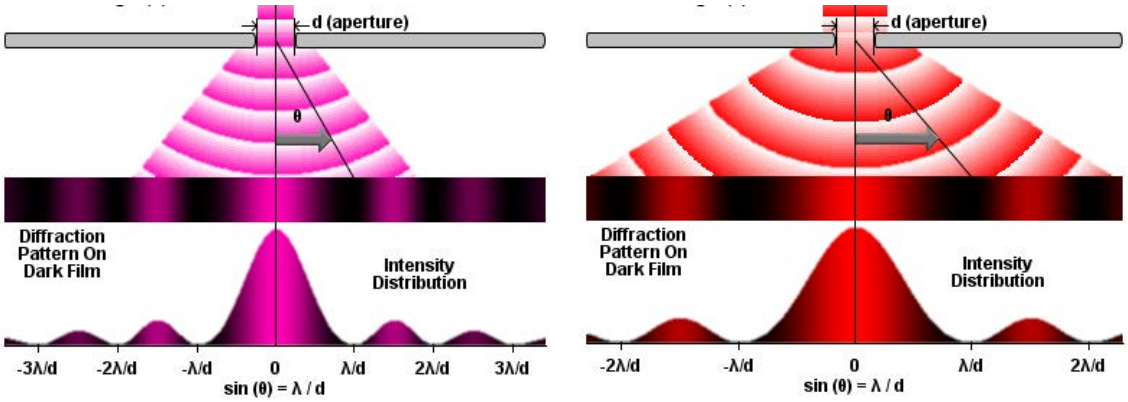

Figure 2.2. Diagram of diffraction patterns for different wavelengths when propagating through the same aperture distance

This is especially important for the case of higher wavelength values and multiple monolithic laser sources, as the diffraction angle increases with the wavelength and the

alignment is constant for all sources, increasing injection losses for higher wavelength values. Figure 2.2 exemplifies this effect by showing the intensity distribution of two different wavelengths propagating through the same media

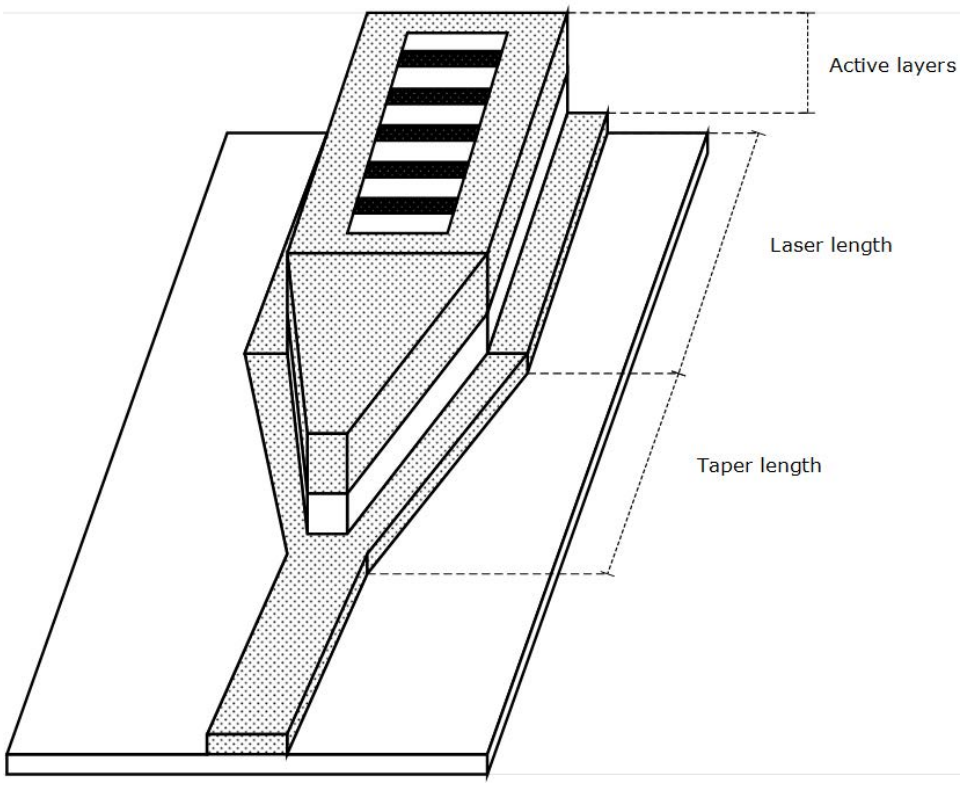

Figure 2.3. Monolithic integration of a semiconductor laser using vertical coupling

Distributed feedback quantum cascade lasers (DFB-QCLs) are one of the solutions capable of monolithic integration using vertical coupling schemes. They exhibit single-mode and narrow linewidth operation by periodically structuring a metal grating on the active region of the device, which have opened the door for sensing applications [19] [20] [21] [22] .

However, the current key limitation of these sources is their narrow tuning range, on the order of few nanometers [23] . Photonic integration can be used to overcome this limitation through the development of an integrated multiplexer structure that combines

the output of several emitters onto a common output waveguide [24] . The main challenge is the development of a technology that supports a small set of building blocks (BBs) and Photonic Integrated Circuit (PIC) Functions[12] .

This challenge must be address through the development of integration technology platforms capable of integrating both active and passive layer structures on the same wafer, allowing to combine active and passive components, providing increased optical integration capabilities of passive functional building blocks - like Distributed Bragg Reflectors (DBR) - with optical gain sections, to develop DBR lasers[25] current state-of-the-art devices integrated by hundreds of functions onto a single chip[26] [27] .

2.1.1 - Building blocks (BBs) in photonic integration

In order for a photonic integration platform to establish an effective technology it needs to offer a set of accurately modeled and characterized building blocks that offer a given range of required functions with which one can design a photonic integrated circuit for a given application just by combining these building blocks. In this form, a hierarchy of building blocks can be defined by inheriting the properties and characterization of individual blocks [28] .

Establishing these Building Blocks allows the foundry to focus their efforts in the fabrication processes required to produce this fixed set of components, significantly reducing the technology development and validation burden [29] while allowing the designers to concentrate on the development of the photonic integrated circuits that meet their needs using this set of components.

2.2 - The III-V InP MIR platform

The III-V Lab platform is an InP based epilayer structure combining an active and a passive regions for monolithic integration. This platform was created with the objective of the design and fabrication of a Mid-Infrared broadband monolithic tunable source for spectroscopy applications in the 7 – 10 μm spectral range [17] [18] .

The values for the characteristic parameters of this epilayer structure (thickness and refractive index) have been defined by III-V according to their own internal wafer growth procedure. The details of such procedure are not within the scope of this work, but certain optimization will be described when the epilayer parameters are presented.

The basic structure, shown in Figure 2.4, is a multiple layer scheme in which the active section is grown on top of the passive epi-layers, producing a wafer supporting active-passive integration. Coupling of light between the active and passive waveguides is achieved through evanescent vertical coupling [30] .

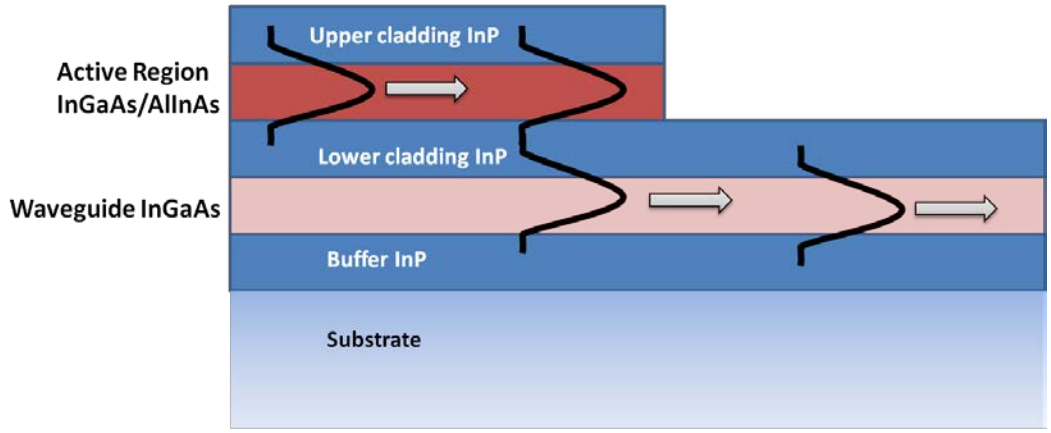

Figure 2.4. Active + passive layer structure given by III-V Lab

The active layer in this multilayer scheme was developed in III-V Lab exclusively for the production of multimode and single mode QCLs. The passive section in the epilayer structure is proposed as part of effort to achieve a monolithic multi-wavelength source without in the framework of the MIRIFISENS project. However, as there was no previous experience on passive waveguide epilayers compatible with the active layer growth, three different epilayer scenarios for passive component design were proposed by III-V Lab to ensure compatibility. The three scenarios, while having the same epilayer structure, include slight variations in material composition to vary modal confinement and propagation losses.

The first passive epilayer design is composed by the following parameters as given by III-V Lab. The fabrication procedure includes a doping of the lower cladding and the substrate layers.

Layer	Thickness (μm)	Optical index
Upper cladding (InP)	2.4	3.0675 + 0.0003i
Active region	2.1	3.3441 + 0.0002i
Lower cladding (InP)	2.4	3.0675 + 0.0003i
Waveguide core (InGaAs)	0.9	3.458 + 0.0i
Buffer (InP)	3.5	3.0792 + 0.0i
Substrate (InP)	>100	2.9608 + 0.0034i

Table 2.1. Structure dimensions and optical indexes for the **first epilayer scenario**

A second step in the optimization process of the epilayer introduced a modification in the doping procedure, as preliminary measurements showed propagation losses in the lower cladding layer.

This second scenario removes the doping of such layer, theoretically reducing modal propagation losses through the waveguide core. However, this decrease in propagation losses was matched with a decrease of modal vertical confinement. The details of this are detailed in the following table.

Layer	Thickness (μm)	Optical index
Upper cladding (InP)	2.4	3.0675 + 0.0003i
Active region	2.1	3.3441 + 0.0002i
Lower cladding (InP)	2.4	3.0792 + 0.0i
Waveguide (InGaAs)	0.9	3.458 + 0.0i
Buffer (InP)	3.5	3.0792 + 0.0i
Substrate (InP)	>100	2.9608 + 0.0034i

Table 2.2. Structure dimensions and optical indexes for the **second epilayer scenario**

A third and final scenario was introduced to further reduce modal propagation losses. In this scenario, all doping procedure is removed from both the lower cladding and substrate layers. The parameters are listed in the following table.

Layer	Thickness (μm)	Optical index
Upper cladding (InP)	2.4	3.0675 + 0.0003i
Active region	2.1	3.3441 + 0.0002i
Lower cladding (InP)	2.4	3.0792 + 0.0i
Waveguide (InGaAs)	0.9	3.458 + 0.0i
Buffer (InP)	3.5	3.0792 + 0.0i
Substrate (InP)	>100	3.0792 + 0.0i

Table 2.3. Structure dimensions and optical indexes for the **third epilayer scenario**

Given the difference in parameter values for the three epilayer scenarios, a comparative waveguiding analysis is proposed in order to help us understand the effects of these variations in terms of modal loss.

2.3 - Simulation of basic optical functions in the III-V Lab platform

2.3.1 - Waveguiding analysis

Due to the novelty of the passive layer structure for the passive components, we required the design of the most basic component, the waveguide, to establish the waveguide dimensions and understand the origin of the propagation losses for each of the different epilayer structures described in the previous section. One key point in this analysis rises from the fact that in the final monolithic tunable source, very different wavelengths must be propagated through a unique waveguide design[18] [31] , following the objective of the MIRIFISENS project, as mentioned in Chapter I.

In order to approach this problem, a first step is to apply a series of simulations in order to optimize the passive waveguide design, establishing the values for the etch depth and waveguide width. These parameters can be seen in Figure 2.5.

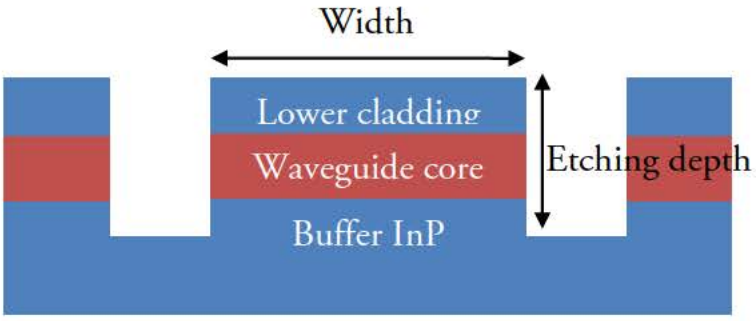

Figure 2.5. Cross-section schemes of the definition of a waveguide

The optimization of these parameters is based on the results for the different combination of the waveguide width and etching depth values. The results are presented in terms of two parameters of interest: modal loss (in dB/cm) and number of modes. The first

of them indicates the propagation losses of the fundamental mode for a given wavelength while propagating through. The second indicates the number of modes that can affect the fundamental propagating mode. However, propagation results will show no effect of these additional modes, as the design model is composed only by a cross section of the waveguide.

For the target application, we must take into account that DFB-QCLs emit in a transverse magnetic (TM) polarization. Therefore, our analysis will include both, the transverse electric (TE) and transverse magnetic (TM) polarizations.

The simulations were done using the Film Mode Matching (FMM) method, which allows for a fast identification of the propagating modes in a cross section. This method was applied for obtaining the single mode behavior for different combinations of both etching depth and waveguide width values in a deep etch configuration.

In order to cover the entire range of the MIRIFISENS requirements for a widely tunable source, the results are also presented as a function of the propagating wavelength, which values were taken within the desired tunable range of the project objective (λ = 7-10 μm).

The following simulation results show the results for the propagation loss and number of modes for both TE and TM polarizations over the different combination values for the waveguide width and etching depth parameters when applied to different wavelength values in the 7 – 10 μm range for the three different epilayer structure scenarios.

A summary of the simulation parameters are:

- Waveguide width range: 5 to 12 μm with a step of Δ=0.5 μm
- Etching depth range: 2 to 5 μm with a step of Δ=0.1 μm
- Wavelength range: 7 to 10 μm with a step of Δ=1.0 μm
- Polarizations: TE and TM
- Number of epilayer scenarios: 3

λ	Fundamental Mode loss (dB/cm)	Number of guided modes
7 µm	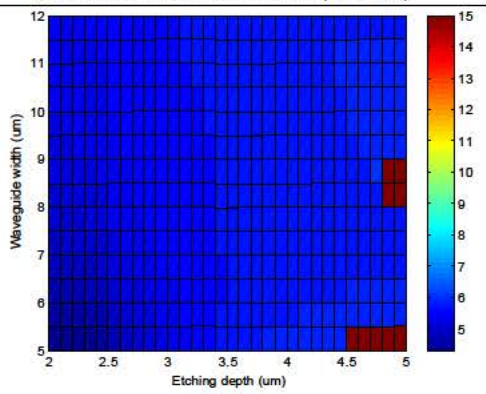	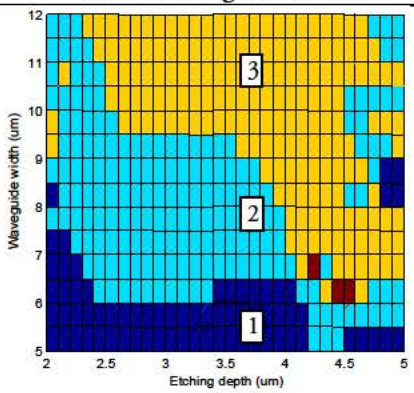
8 µm	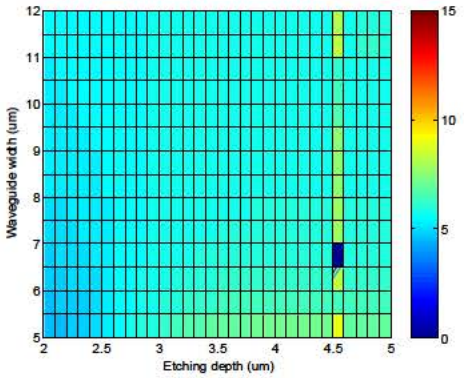	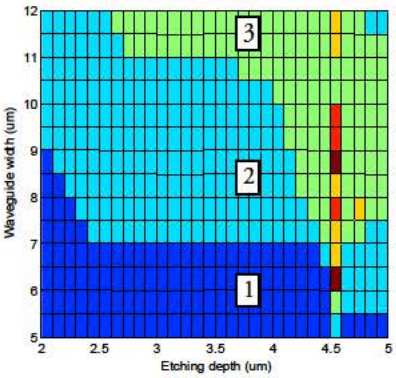
9 µm	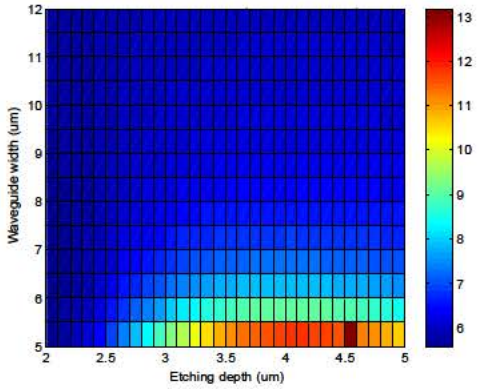	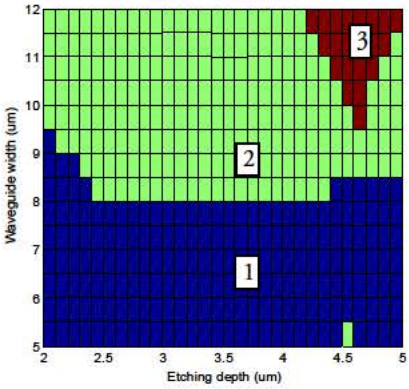
10 µm	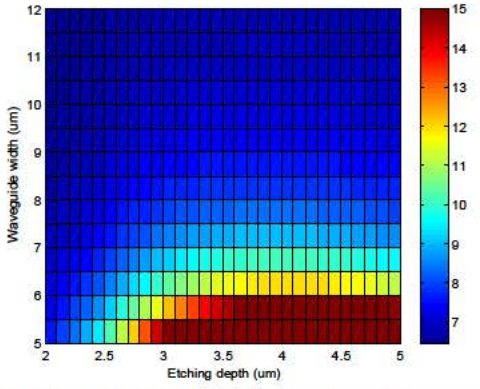	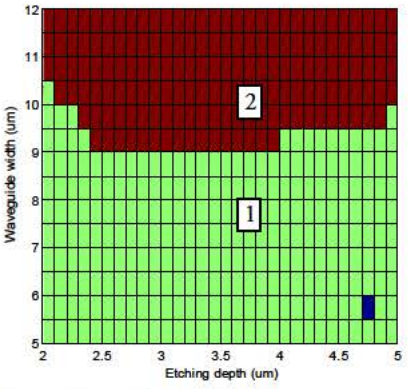

Table 2.4. TE etching and width waveguide analysis for **epilayer scenario 1**

λ	Fundamental Mode loss (dB/cm)	Number of guided modes
7 µm	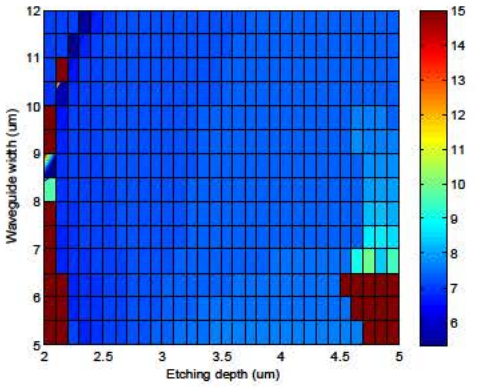	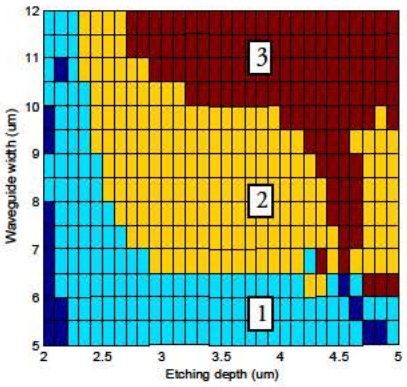
8 µm	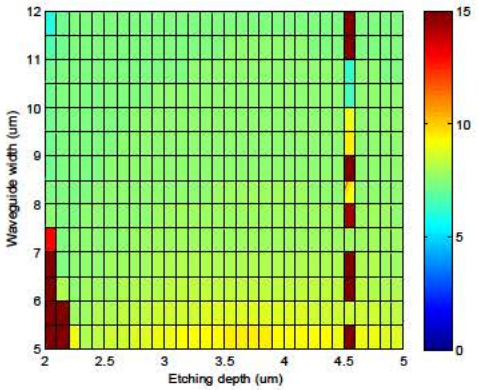	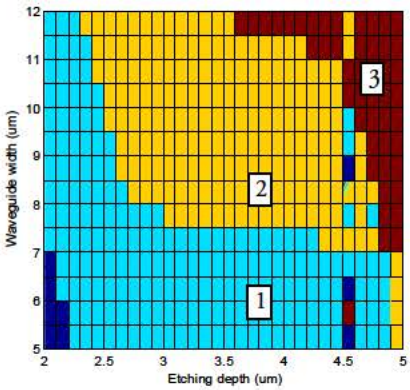
9 µm	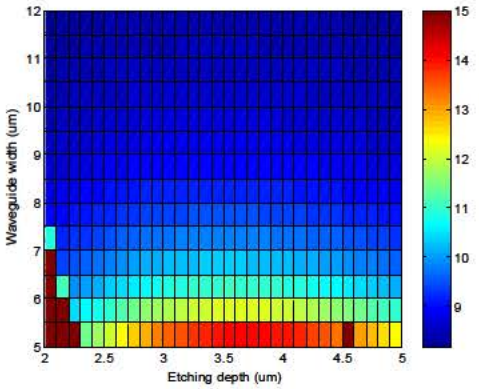	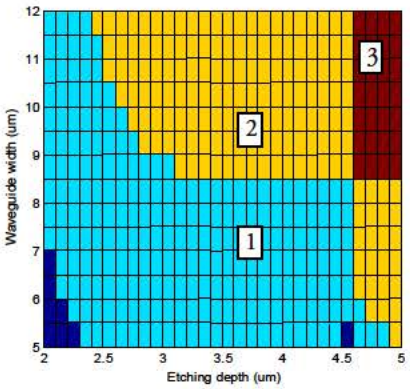
10 µm	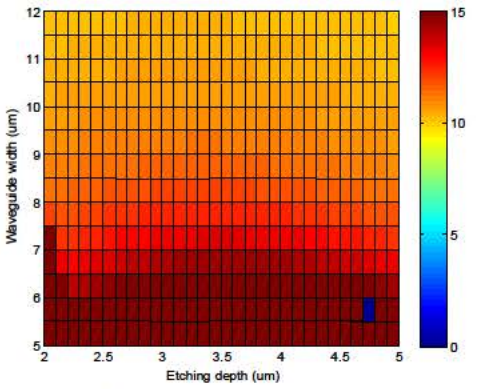	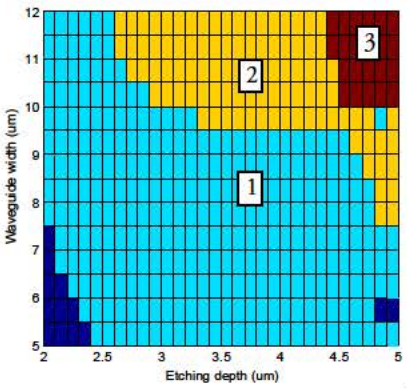

Table 2.5. TM etching and width waveguide analysis for **epilayer scenario 1**

λ	Fundamental Mode loss (dB/cm)	Number of guided modes
7 µm	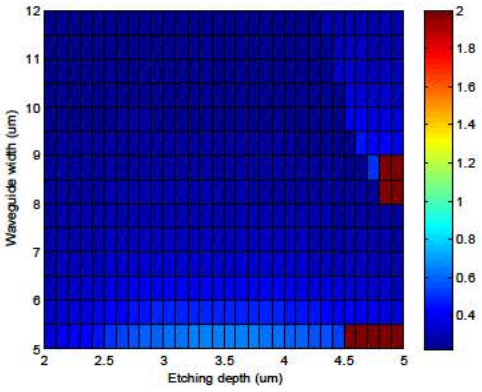	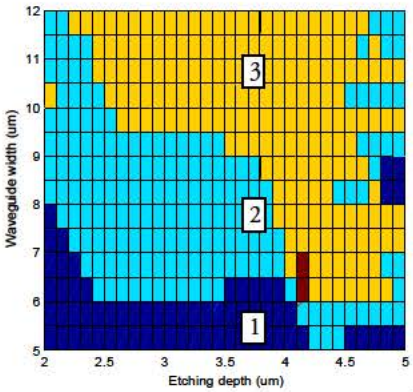
8 µm	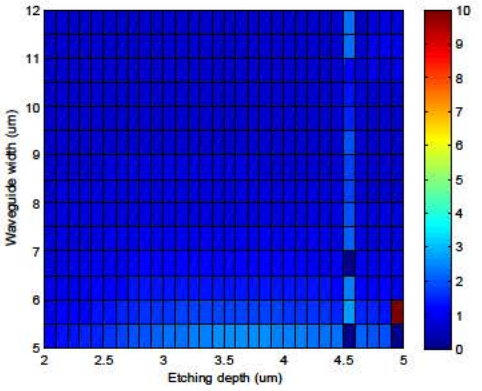	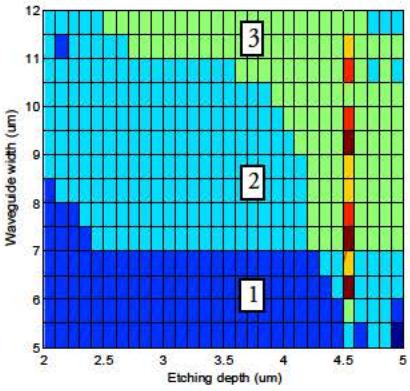
9 µm	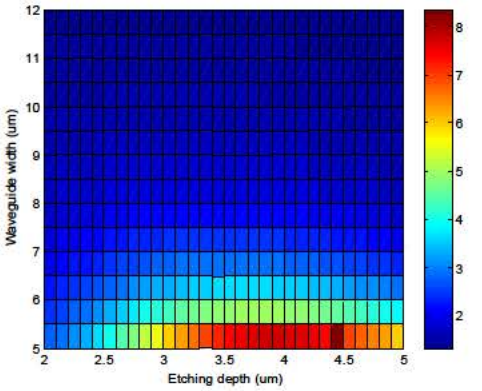	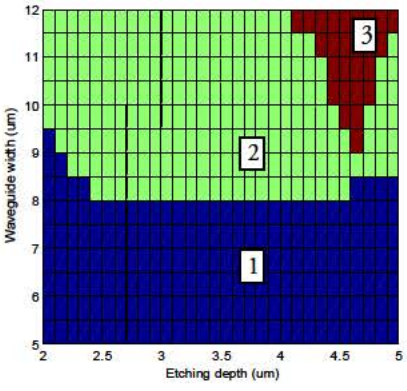
10 µm	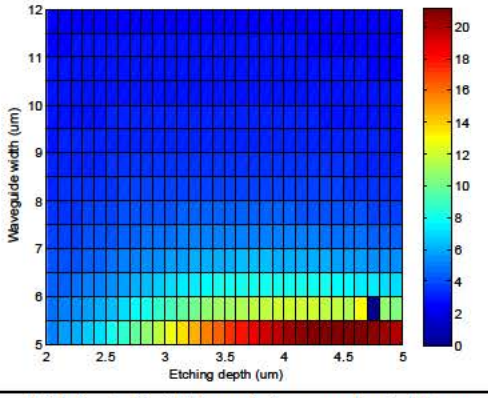	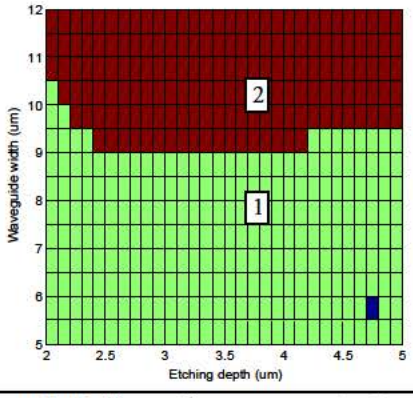

Table 2.6. TE etching and width waveguide analysis for **epilayer scenario 2**

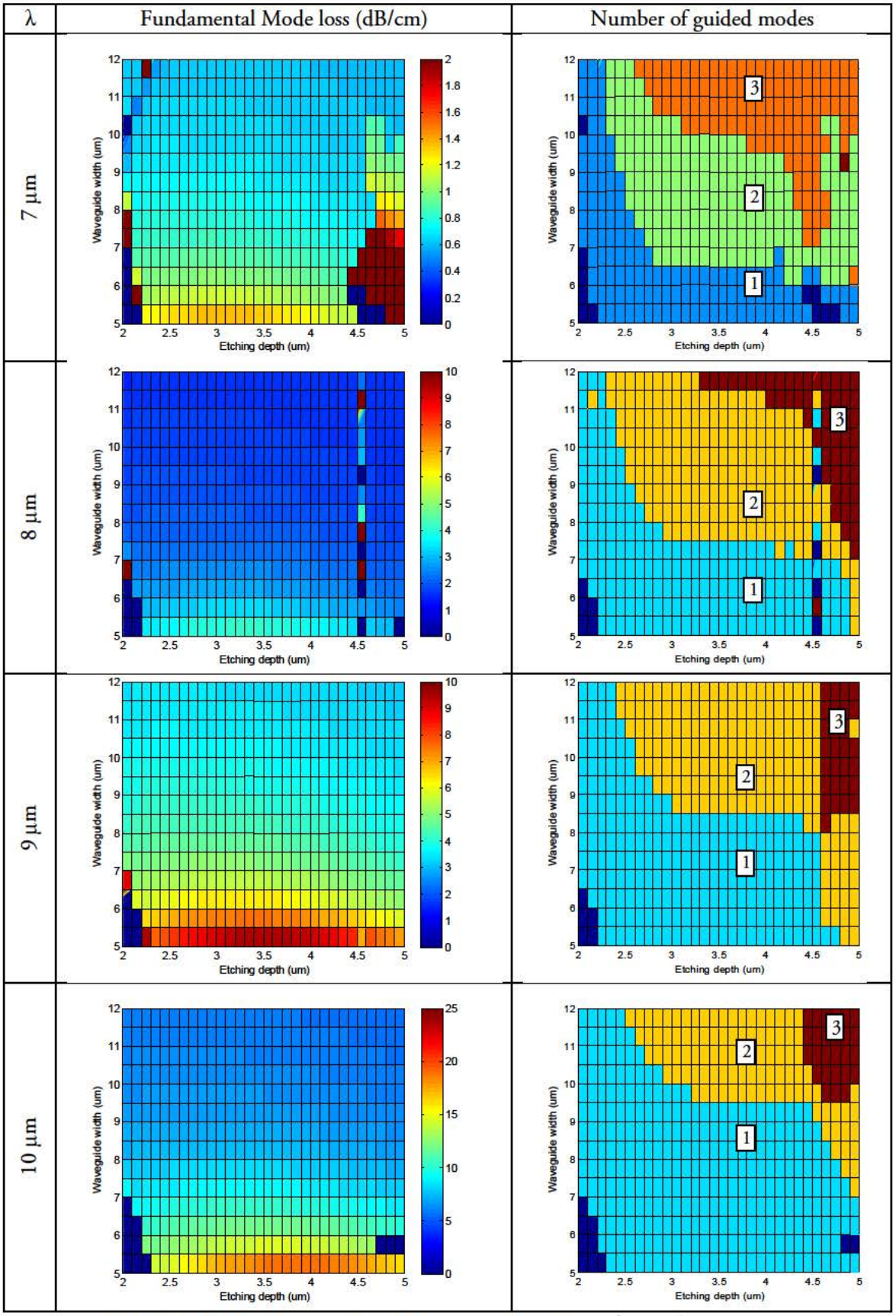

Table 2.7. TM etching and width waveguide analysis **for epilayer scenario 2**

λ	Fundamental Mode loss (dB/cm)	Number of guided modes
7 µm	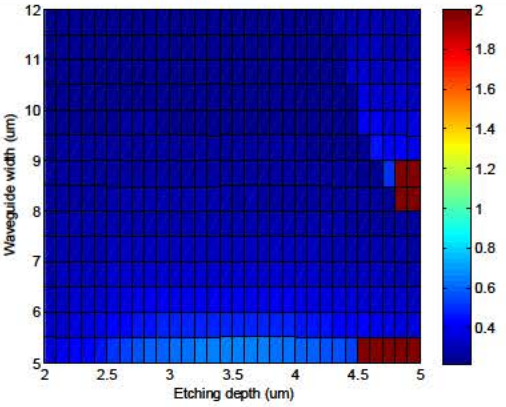	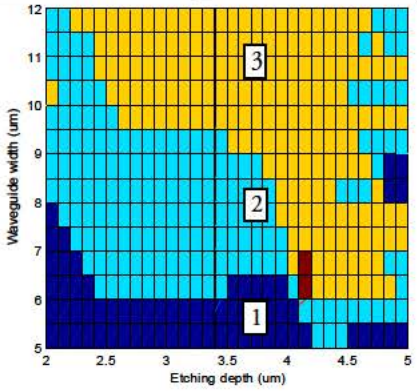
8 µm	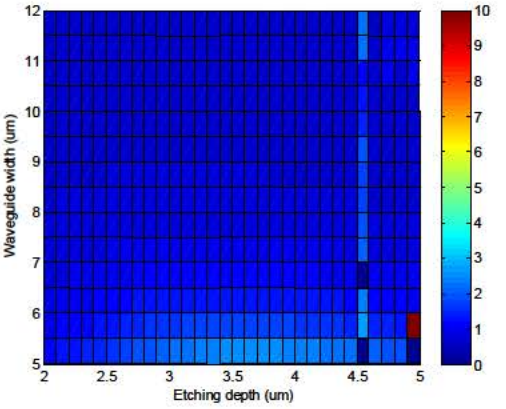	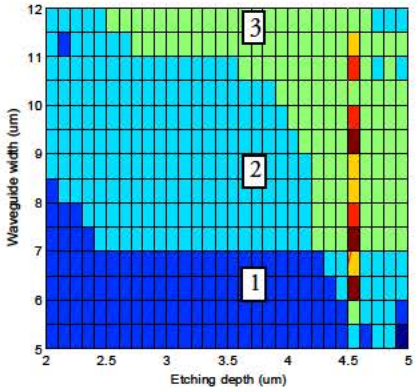
9 µm	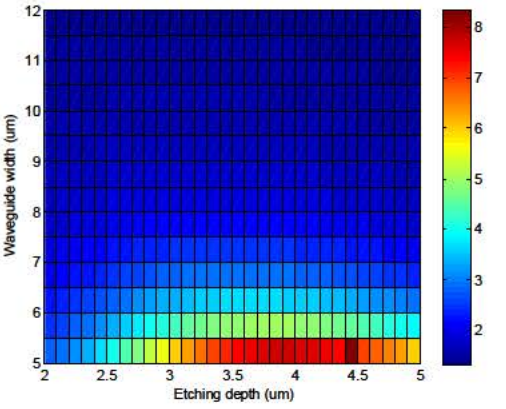	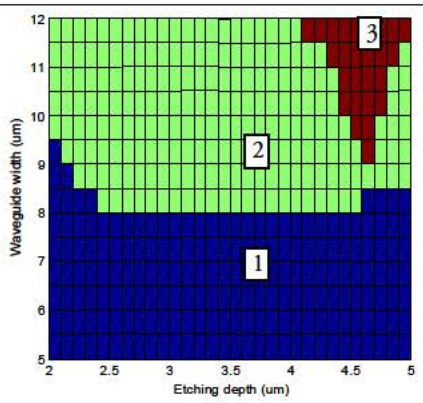
10 µm	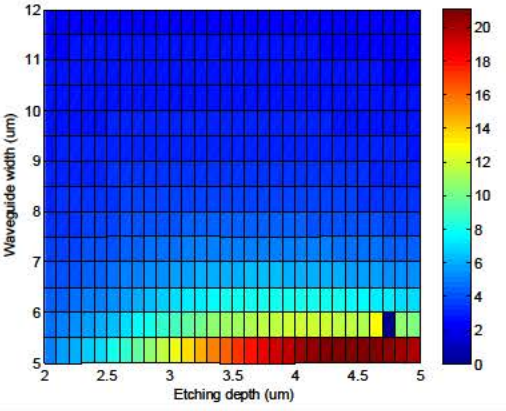	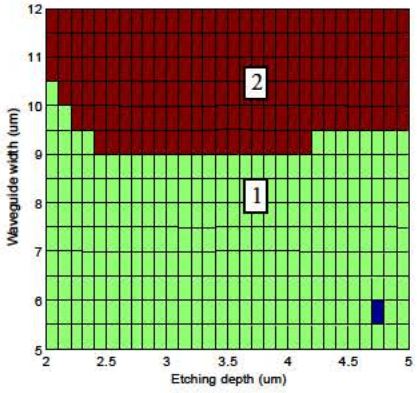

Table 2.8. TE etching and width waveguide analysis for **epilayer scenario 3**

λ	Fundamental Mode loss (dB/cm)	Number of guided modes
7 µm	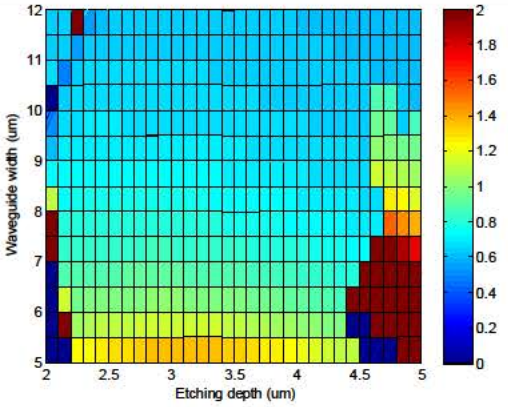	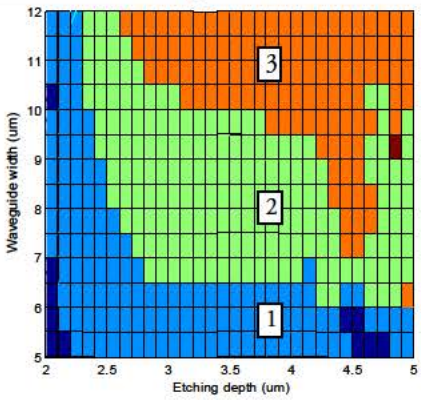
8 µm	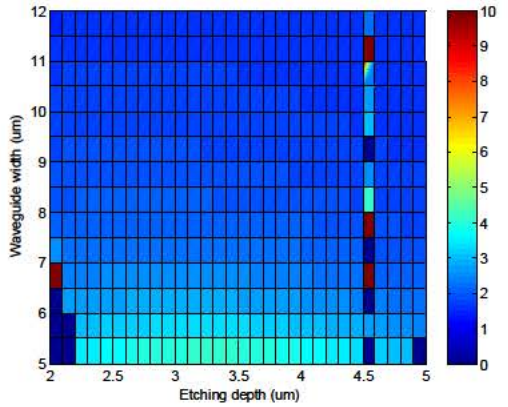	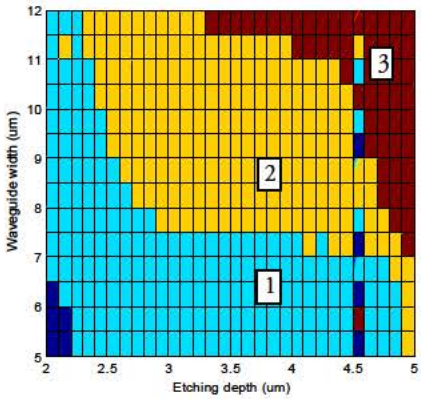
9 µm	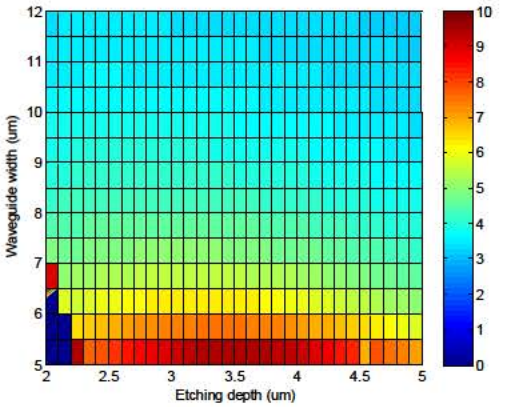	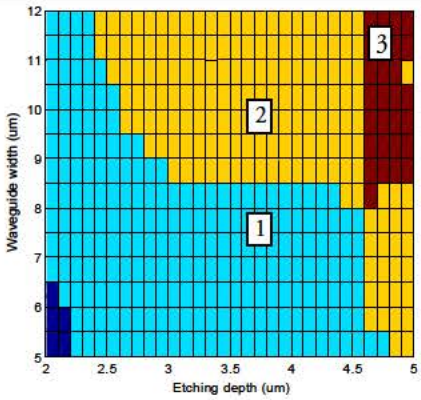
10 µm	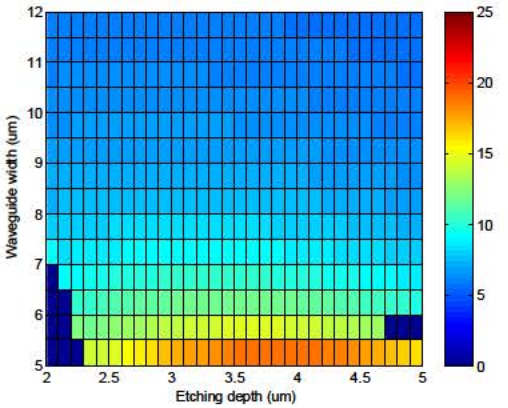	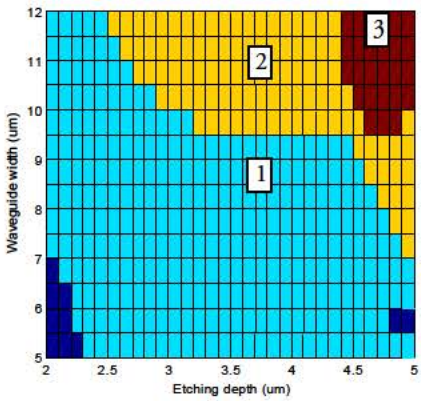

Table 2.9. TM etching and width waveguide analysis for **epilayer scenario 3**

In the simulation results a large difference in fundamental mode loss analysis is found, which is larger for both the TE and TM polarizations on the first epilayer scenario.

This is because of the difference in the optical index in the lower cladding layer, on top of the waveguide core. The imaginary value of the optical index is related to the absorption coefficient and therefore indicates the presence of loss due to the intrinsic characteristics of the InP material in the layer. In all cases, the additional losses due to this absorption are more than 5 dB/cm.

The second and third epilayer value scenarios are consistent in results due to the apparent lack of effect that the absorption coefficient of the substrate InP has over the propagating fundamental mode through the waveguide core. The numerical difference between fundamental mode losses between the epilayer scenarios 2 and 3 is less than 2%, favoring scenario 3, due to the absence of additional losses due to the effect of the absorption coefficient of the substrate.

The results allow for the quantification of such additional losses when comparing the fundamental mode loss results between the epilayer models. Additionally, the results show that the doping of the substrate layer has negligible effect on the propagation losses of the fundamental TE and TM modes.

The number of guided modes was also studied to find the region at which both the waveguide width and the etching depth allow for the propagation of fundamental TE and TM modes without the incursion of possible higher order mode conversion, which could increase the propagation losses. In all cases it was observed that the simulations indicate that the etching depth value of the fabrication process must be lower than 4.5 μm and also

that monomode behavior was ensured when the waveguide width is at least 1.0 μm lower in value that the simulated wavelength. This value was selected to be the maximum allowed for the etching depth.

However, further observation of the number of guided modes results show that a deep etch scheme (etching depth more than 3.5 μm) ensure a better monomode confinement when a 7.0 μm wavelength value is simulated. This special consideration allows for the etching depth parameter to have a wider monomode operation range, which is defined between 3.5 and 4.5 μm. The definition of this range allows for an additional advantage in the fabrication process that allows for a higher error margin without compromising the viability of the future samples.

In order to ensure monomode behavior for both TE and TM modes for all the wavelength range, a waveguide width value of 6.0 μm was selected. While it is true that this value could introduce additional losses for high wavelength values (> 7.0 μm), it is necessary in order to comply with the MIRIFISENS requirement for a widely tunable source which specify that the same waveguide width should be used for all the wavelength range[32] [33] . The simulated fundamental mode losses for the combination of the selected waveguide width and etching parameter values are compiled in the following table.

λ (μm)	Propagation losses for TE polarization (dB/cm)	Propagation losses for TM polarization (dB/cm)
7	0.7	1.2
8	2.5	3.5
9	4.5	7.0
10	9.0	>10.0

Table 2.10. Propagation losses for the third epilayer scenario as a function of wavelength and polarization

The results show a high increment in the losses for higher wavelength values, however, the propagation losses are correspondent to the level of losses for other InP fabrication platforms, which have presented propagation losses of 9.5 dB/cm at 1510 nm and 6.0 dB/cm at 1570 nm[34] .

Few attempts to propagate MIR laser light over InP waveguides have been reached, being SiGe based platforms the most used for these wavelengths, as losses as low as 1 dB/cm at 4.5 μm and 2 dB/cm at 7.4 μm have been reached[35] . However, as it has been mentioned in section II.I, the monolithic integration capabilities of InP platforms along with laser sources reduce the possibility of increased losses due to butt coupling or other light insertion schemes[18] [30] [31] .

2.3.2 - Bent waveguides

Bent waveguides are, together with straight waveguides, the most basic components to study in any design platform. Their functionality, as it has been mentioned for straight waveguides, is to connect different components inside a photonic circuit.

Their design is related to straight waveguide optimization and extends the parameter list to ensure modal propagation thought non-straight waveguides. The additional design parameter is defined as minimum bending radius R_{min} and represents the minimum value that the bending has to comply in order to avoid undesired effects on the propagating mode and additional losses.

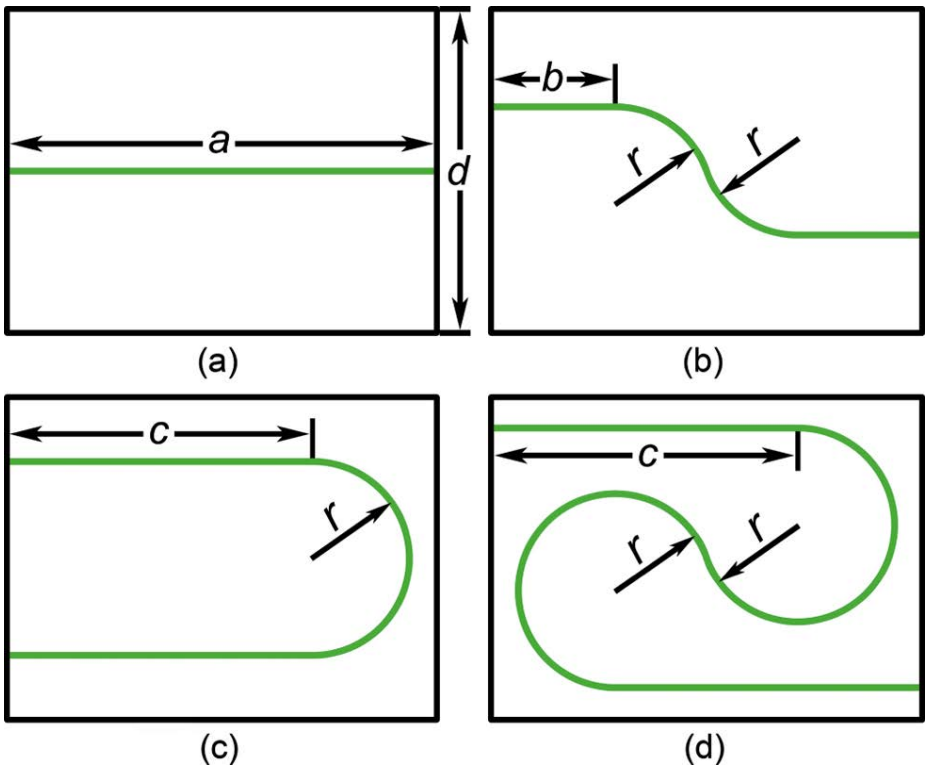

Figure 2.6. Straight waveguide example (a) and different outlines of bent waveguides (b, c, d) showing the bending radius **r** in an "arc" scheme

When a waveguide is bent, the modal field will shift towards the outer core/cladding boundary as the bend radius decreases, but the effect on the modal propagation constants causes the higher order modes to appear, altering the monomode behavior of the propagating light [36] . At the same time, if the bending radius of a bent waveguide exceeds a certain minimum, the design will present additional losses in form of radiation (Figure 2.7).

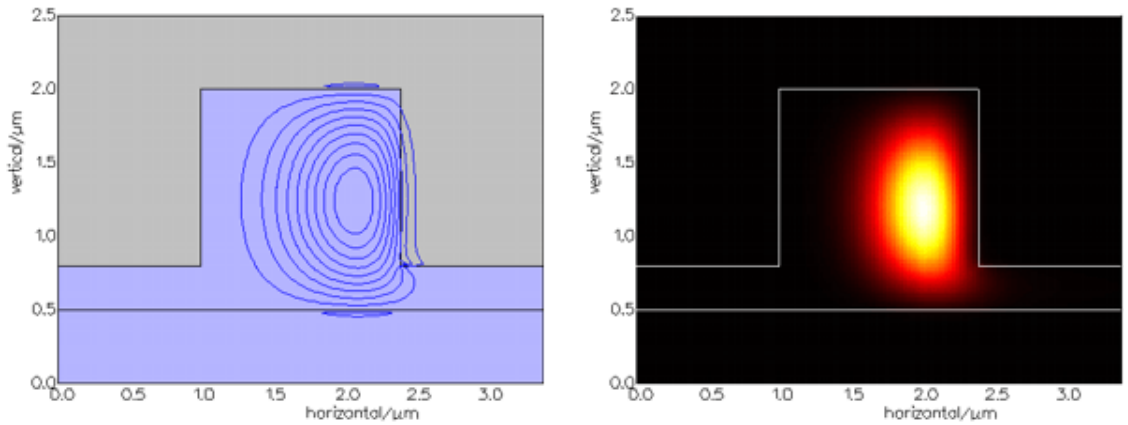

Figure 2.7. Cross section of a bent waveguide showing the mode profile (left) for a simulated mode and the intensity of such mode (right).

Bent waveguide design must ensure to comply with this minimum radius parameter, so that the propagating modes would not excite higher order modes nor increase the losses due to radiation.

The goal of our analysis is to identify the R_{min} value to ensure fundamental TM mode propagation and minimize dispersion losses. T the same time, TE mode propagation losses are studied, as it becomes necessary to ensure no losses due to the apparition of higher order modes through the bends.

Soibel et al [37] proposes an analytical approach to define the R_{min} value for arc waveguides in the MIR. The starting point is defined by the relations:

$$\frac{R_{min} \cdot \Delta}{\rho} \gg 1 \qquad \text{Eq. 2.1}$$

$$\Delta = \frac{\eta_{core}{}^2 - \eta_{cladding}{}^2}{\eta_{core}{}^2}$$

$$\rho = \frac{1}{2} WgWidth$$

Where R_{min} is related to the refractive indexes of both the waveguide core and the cladding of any waveguide with a cladding/core configuration. This relation allows knowing the minimum value that ensures propagation while minimizing radiation losses based on the characteristics of the materials that are part of the waveguides.

Taking the waveguide definition parameters as studied in 0 and the optical indexes for the third epilayer case, the analytical approach provides a R_{min} = 170.00 µm.

To have a better view of this analysis, a simulation approach was done using the Beam Propagation Method (BPM, see Annex C) and the Film Mode Matching (FMM) method. Initial simulations using maximum etching depth values (6.8 µm) show certain modal dispersion for the previously obtained value of R as can be observed in Figure 2.8.

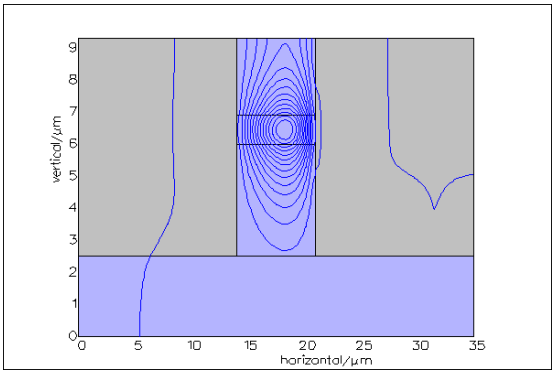

Figure 2.8. Bent mode image for minimum radius and full etching depth value

In order to observe the modal behavior of our guides in terms R_{min}, a minimum radius sweep was applied to the structure. A simulation approach was applied by using the FMM method as it was done for the straight waveguide parameter definition. The configuration parameters of this simulation follow a mode profile horizontal and vertical resolutions of nx = 120 and ny = 90 respectively. The number of unidimensional modes was set to 30, as the transversal view of the waveguide is relatively small. The total simulation area is defined by the dimensions x = 30 µm and y = 9 µm. The definition and use of these parameters become necessary given that the numerical model has to calculate the deformation of the propagating mode (Figure 2.8); the definition of such parameters can be found in Annex C. This parameter selection is enough to correctly simulate the modal behavior when a bend value sweep is applied.

Parameter sweep results show additional transmission losses, in comparison with the straight waveguide model results, due to the excitation of superior order modes and radiation when R < 165 µm. The R_{min} value is set to 170 µm to comply with this restriction. FMM simulations show correct fundamental TM modal confinement when this updated value is applied, as shown in Figure 2.9.

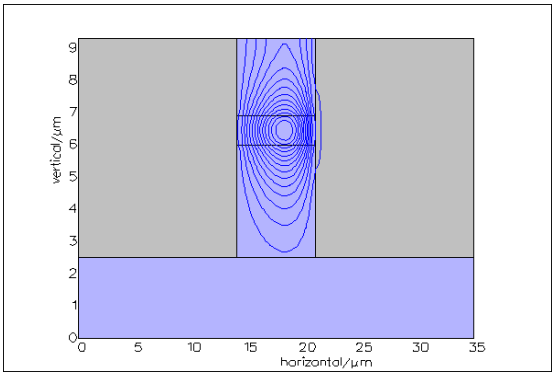

Figure 2.9. Bent mode image for R = 170 µm and full etching depth value

Once the minimum radius R_{min} is set, the next step is to model bend waveguides in order to measure propagation losses. A first approach was to simulate soft bending schemes, such as sine and cosine bends. These schemes were selected as a base for bend propagation analysis due to their gradual reduction of the radius in comparison with other structures such as arcs. Both sine and cosine bends present slight different profiles and this affects the light; their effect becomes more apparent in more complex structures such as Y-junction splitters/combiners.

The bends are described by the following functions:

$$Sine \rightarrow \ y = \frac{h}{L}z - \frac{h}{2\pi}\sin\left[\frac{2\pi}{L}z\right] \qquad \text{Eq. 2.2}$$
$$Cosine \rightarrow \ y = \frac{h}{2}\left[1 - cos\left[\frac{\pi}{L}z\right]\right]$$

Where **y** is the final outline of the bend (Figure 2.10), **h** is the function offset of the curve, **L** is the section length and **z** is the propagating axis of the bend. The parameters of interest in the bending radius analysis are then the offset (**h**) and the curve radius (**Rmin**). From the given equations we can infer a function describing the length of the S-bend. This equation takes the form:

$$L = \sqrt{2\pi h R_{min}} \qquad \text{Eq. 2.3}$$

In order to have a better idea of the differences in the outline of the bend functions, a function plot is done for a 50 μm offset value and the previously calculated minimum radius (R = 170 μm).The graphic comparison of the outline of both function models is observed in Figure 2.10.

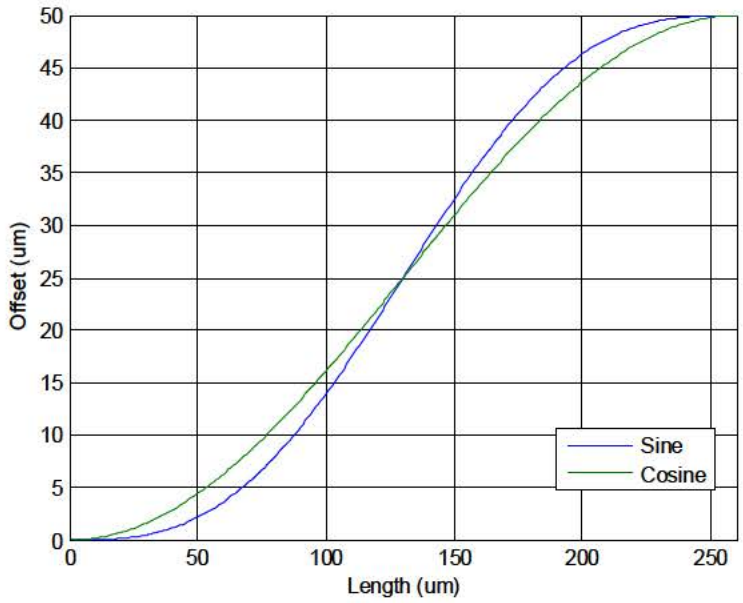

Figure 2.10. Bent waveguide model comparison for a 50 µm offset

As can be observed, the sine profile presents a more abrupt radius reduction in comparison with the cosine. Conclusions over this observation are given in the characterization section of this work.

Once the basic waveguide parameters are defined, as well as the bend functions to characterize, a propagation study becomes necessary in order to quantify other design factors such as the bending losses as a function of the propagation distance (dB/cm).

We have carried different simulations to assess the propagation losses through a single bent waveguides using both sine and cosine bending patterns. We analyzed those function profiles aiming to understand the propagation loss sources in S-bent waveguides and obtain preliminary data in order to design the basic 2-to-1 Y-junction coupler. The simulations were based on a Finite-Difference Time-Domain (FDTD) propagation method, following the same parameter values as in previous simulation approaches. The mode behavior and propagation loss percentage for an offset value of 50 µm and a wavelength of 7.0 µm,

which corresponds to the minimum value of the 7-10 μm range of the MIRIFISENS objective, are shown in Table 2.11.

The propagation results for a single mode bent waveguide of 6 μm width, as it is the selected optimal width for the platform in section 0, were applied to different offset values in order to and a deep etch waveguide model.

Propagated mode profile	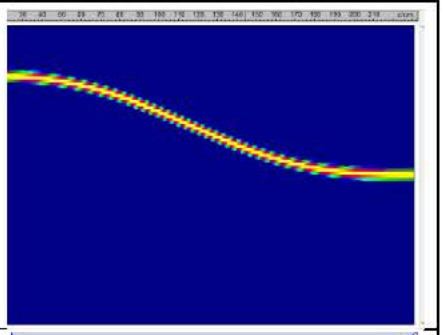
Propagation loss (%) for a Sine bent profile	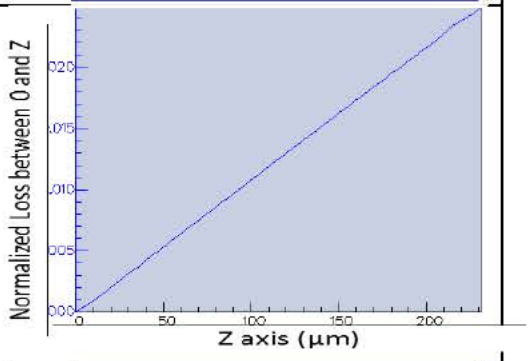
Propagation loss (%) for a Cosine bent profile	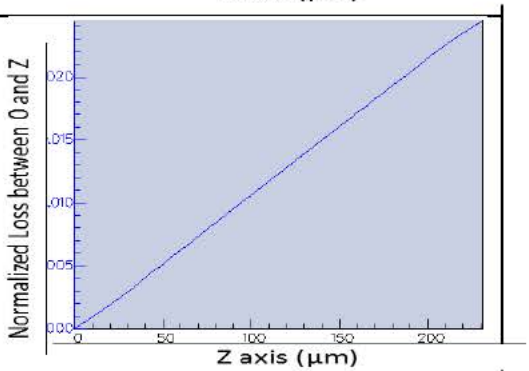

Table 2.11. Propagation loss profile and loss percentage for a sine bent waveguide as a function of the offset

The results show no losses due to coupling into higher order modes and a proportional increase in the propagation losses as a function of the offset. Single mode propagation on

the fundamental mode was confirmed for the full length of the bend. Transmission losses for the fundamental TE and TM modes were found to be slightly higher for sine bends and bending related losses were only 5% of the total losses in all cases.

Following the building block definition approach, we define a basic sine and cosine bend building block. The parameter description for this block is resumed in Table 2.12.

Building block name	**S-bend**
Input parameters	Identifier
Waveguide width	w
Radius	R
Offset	h
Output parameters	Identifier
Device length	L

Table 2.12. S-bend BB description

2.3.3 - Y-junction building blocks

The combination of curved waveguides can be used to create a higher functional component, to combine or divide optical power. When two bent waveguides approach each other, a Y-junction coupler is form. These couplers are defined by two separate sine S-bend building blocks, placed in a vertical specular image scheme.

Following the previous simulation scheme as in sine/cosine bends, an FDTD propagation analysis was applied with the same simulation parameters as the sine S-bend block. This numerical method was selected because the Y-junction coupler presents a free propagation region in the overlapping region of both the bent waveguides conforming the junction [37] . This free propagation region presents causes mode reflections that other numerical methods are not capable of processing.

Using the same simulation parameters for S-bend waveguides, a series of simulations were done in order to observe and quantify the modal behavior and the losses for both sine and cosine Y-junction based schemes. The results of those can be found in Table 2.13.

Propagated mode profile	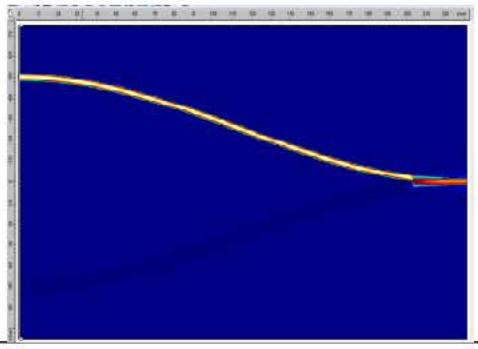
Propagation loss (%) for a Sine bent profile Y-junction scheme	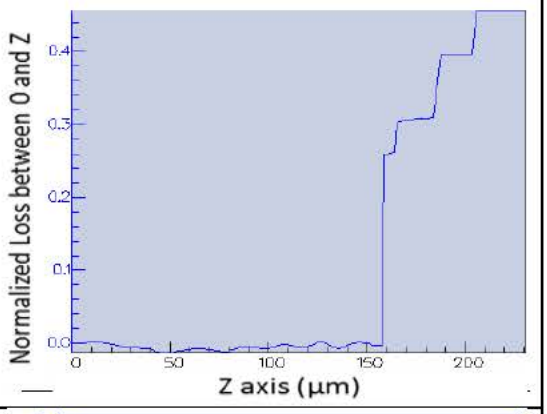
Propagation loss (%) for a Cosine bent profile Y-junction scheme	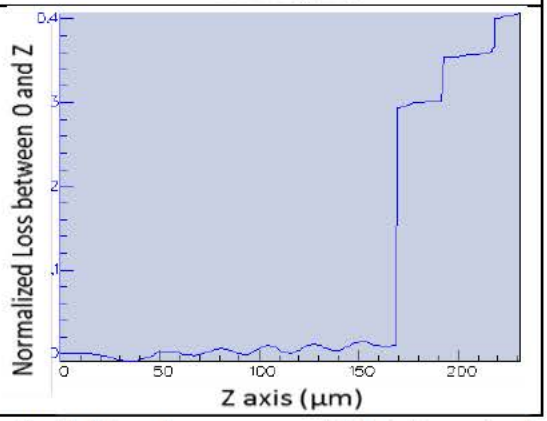

Table 2.13. Propagation loss profile (left) and percentage (right) for a sine bent based Y-junction coupler as a function of the offset

Table 2.13 shows the simulation results when an input MIR wavelength of 7.0 µm, which corresponds to the minimum value of the 7-10 µm range of the MIRIFISENS objective, is propagated from left to right into the coupler scheme. The table also shows the propagation loss profile and the appearance of different modes in the free propagating region where the two bent waveguides overlap. These different modes are observed to be

close but not confined inside the free propagating region conformed when the two bent waveguides form a single output. These observations are explained in Figure 2.11

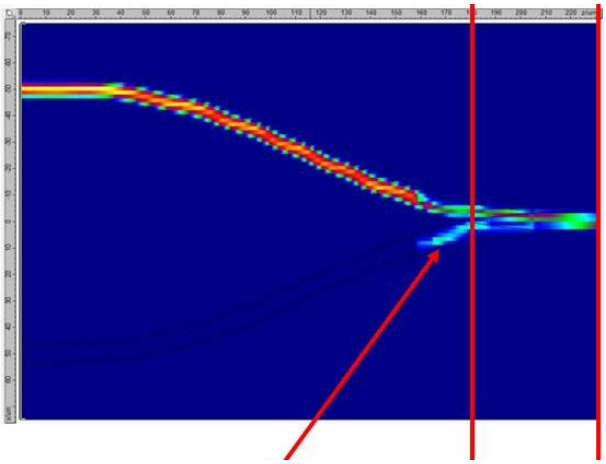

Figure 2.11. Intensity profile for a Y-junction coupler showing additional modes and the mode behavior in the free propagation region

Additional losses are observed to be related to this phenomena and the total loss is observed to be close to 50% for all cases when propagation losses in the bent are taken into account. Additional modes were formed due to back reflections in the free propagation region, along with modal coupling from the mode in the propagating bent waveguide.

The building block definition of the sine S-bend Y-junction coupler can be defined as a function of the input and output parameters shown in Table 2.14.

Building block name	**S-bend Y-junction coupler**
Input parameters	Identifier
Waveguide width	w
Radius	R
Offset	h
Output parameters	Identifier
Device length	L

Table 2.14. S-bend Y-junction coupler BB definition

2.4 - Discussion and remarks

In this chapter, a waveguiding analysis was done in order to comply with a series of objectives. The first of them, the selection of the epilayer structure was performed using an FMM numerical method in order to quantify the propagation losses for the fundamental TE and TM modes when different values of wavelength, waveguide width and etching depth were studied.

These results allowed for the identification of parameter values compatible with all the wavelength range of the objective.

The next step was to do an analytical study to introduce the concept of bent waveguides to the waveguiding analysis, which introduced the concept of minimum radius (R_{min}) into the basic design parameters. This analytical approach allowed for the definition of a minimum bend radius to ensure modal confinement and minimize bent-related losses.

The selected bent waveguide schemes to introduce were the sine and cosine S-bends. This bend schemes allow for a gradual increasing of the waveguide radius, further minimizing bent related losses in comparison with other bending schemes, such as arcs.

Taking the defined parameter values as base, a series of simulations using the FDTD method were performed over these bend schemes for different offset values. The change in method was motivated in order to have a comparison point between these schemes and the subsequent modifications that would introduce reflections and higher order modes. The

results confirmed a maximum increasing in propagation loss of 5% in comparison with the straight waveguides and to define a basic design function (building block, BB) for the S-bend waveguide.

These results allowed for the introduction of a 2-to-1 Y-junction scheme based on S-bends, which introduced a free propagation region in the area formed were the two bent waveguides join.

A series of simulations using the FDTD method were also performed for the same offset values as the single S-bends, allowing for a direct comparison between the basic bend waveguides and these Y-junction couplers. The results showed the apparition of superior order modes and reflections in the free propagation region formed between the two S-bends. The additional losses were significant and were quantified to be between 35-50% of the input power, with additional losses in the Sine S-bend scheme due to the increased area of overlapping between waveguides in comparison with the Cosine S-bend scheme.

A summary of the parameter values and significant results is summarized in the next table

Wavelength range (μm)	7-10 μm
Chosen epilayer scenario	Scenario 3
Waveguide width (μm)	6.0 μm
Etching depth (μm)	3.5 – 4.5 μm
Minimum radius, R_{min} (μm)	170 μm
Additional losses in S-bends	Up to 5% of the total losses
Losses in Y-junctions for Sine	42-50% of the input power
Losses in Y-junctions for Cosine	35-40% of the input power

Table 2.15. Summarization of the waveguiding parameters and simulation results

2.5 - References

[1] Photonics 21; “Our vision for a Key Enabling Technology of Europe”, 2011.

[2] Willner, A.E.; Byer, R.L.; Chang-Hasnain, C.J.; Forrest, S.R.; Kressel, H.; Kogelnik, H.; Tearney, G.J.; Townes, C.H.; Zervas, M.N., "Optics and Photonics: Key Enabling Technologies," inProceedings of the IEEE , vol.100, no.Special Centennial Issue, pp.1604-1643, May 13 2012

[3] Compound Semiconductors: Physics, Technology, and Device Concepts. [Online]. Available: http://www.uni-ulm.de/?id= 19197

[4] H. Morkoc, Handbook of Nitride Semiconductors and Devices, Volume 1, Materials Properties, Physics and Growth. Weinheim: Wiley-VCH, 2008.

[5] L. A. Coldren and S. W. Corzine, Diode Lasers and Photonic Integrated Circuits. Hoboken, NJ: Wiley, 1995.

[6] S. L. Chuang, Physics of Photonic Devices, 2nd ed., Hoboken, NJ: Wiley, 2009.

[7] R. D. Feldman, D. Lee, A. Partovi, R. P. Stanley, A. M. Johnson, J. E. Zucker, A. M. Glass, and J. Hegarty, BGrowth, optical, and optoelectronic properties of CdZnTe/ZnTe multiple quantum wells,[Critical Rev. Solid State Mater. Sci., vol. 17, pp. 477–506, 1992.

[8] S. E. Miller, BIntegrated opticsVAn introduction,[Bell Syst. Tech. J., vol. 48, pp. 2059–2069, 1969.

[9] P. K. Tien, BIntegrated optics and new wave phenomena in optical waveguides,[Rev. Mod. Phys., vol. 49, pp. 361–420, 1977.

[10] A. Yariv, BThe beginning of integrated optoelectronic circuits,[IEEE Trans. Electron. Devices, vol. ED-31, pp. 1656–1661, Nov. 1984.

[11] T. L. Koch and U. Koren, BSemiconductor photonic integrated circuits,[IEEE J. Quantum Electron., vol. 27, pp. 641–653, 1991.

[12] Smit, M.; et al; "An introduction to InP-based generic integration technology," Semicond. Sci. Technol. 29 (2014)

[13] Imanaka, H.; et al; “Optical constants of Titan tholins at mid-infrared wavelengths (2.5–25 μm) and the possible chemical nature of Titan’s haze particles”

[14] Capasso, F.; Gmachl C., Sivco, D. L., Cho, A. Y., "Quantum cascade lasers," Phys. Today 55 5", 34 (2002)".

[15] Gaumont, E.; Graver, C.; Gentner, J.L.; Pinquier, A.; Laube, G., "Butt coupling process for InP based photonic integrated circuits," in Indium Phosphide and Related Materials, 1996. IPRM '96., Eighth International Conference on , vol., no., pp.256-258, 21-25 Apr 1996

[16] C. Gilles ; G. Maisons ; B. Simozrag ; M. Carras; "Monolithic coupling of QCLs in evenescent waveguides on InP", Proc. SPIE 9370, Quantum Sensing and Nanophotonic Devices XII, 93702W (2015)

[17] Maisons, G.; Carras, M.; et al; "Advances toward monolithic tunable source," ISLC (2014)

[18] Carras, M.; et al; "Advances toward monolithic broadly-tunable QCL sources," Proc. SPIE 8993 (2014)

[19] Karin, H. "Tunable Diode Laser Spectroscopy." 1995

[20] Cassidy, D. T.; Reid, J., "Atmospheric pressure monitoring of trace gases using tunable diode lasers," Appl. Opt. 21(7), 1185–1190 (1982)

[21] Werle, P.; Slemr, F.; Maurer, K.; Kormann, R., Mucke, R., Janker, B., "Near- and mid-infrared laser-optical sensors for gas analysis," Opt. Las. Eng. 37(2–3), 101–114 (2002)

[22] Lee, B.; et al; "Widely tunable single-mode quantum cascade laser source for mid-infrared spectroscopy", APL 91, 231101 (2007)

[23] Faist, J.; et al; "Distributed feedback quantum cascade laser", APL 70, 2670 (1997)

[24] Lee, B. G.; et al; "Broadband Distributed-Feedback Quantum Cascade Laser Array Operating From 8.0 to 9.8 \mu m" Photonics Technology Letters, IEEE , vol.21, no.13, pp.914,916, July1, (2009)

[25] Yu, L.; Lu, D.; Zhao, L.; Li, Y.; Ji, C.; Pan, J.; Zhu, H.; Wang, W., "Wavelength and Mode-Spacing Tunable Dual-Mode Distributed Bragg Reflector Laser," Photonics Technology Letters, IEEE , vol.25, no.6, pp.576,579, March15, 2013

[26] Assefa, S.; Green, W.M.J.; Rylyakov, A.; Schow, C.; Horst, F.; Vlasov, Y.A.; "Ultra-dense monolithic integration of optical and electrical functions on silicon for optical interconnects," General Assembly and Scientific Symposium, 2011 XXXth URSI , vol.; no.; pp.1,2, 13-20 Aug. 2011

[27] Yu S.; Li, B., "All-optical signal processing functions using semiconductor ring lasers," Lasers and Electro-Optics Europe (CLEO EUROPE/EQEC), 2011 Conference on and 12th European Quantum Electronics Conference , vol.; no.; pp.1,1, 22-26 May 2011

[28] Smit, M.; et al; "An introduction to InP-based generic integration technology," Semicond. Sci. Technol. 29 (2014)

[29] Lawniczuk, K.; Smit, M.K.; "JePPIX: access to generic foundry processes for InP photonic integrated circuits," Avionics, Fiber-Optics and Photonics Technology Conference (AVFOP), 2014 IEEE , vol.; no.; pp.43,44, 11-13 Nov. 2014

[30] C. Gilles ; G. Maisons ; B. Simozrag ; M. Carras; "Monolithic coupling of QCLs in evenescent waveguides on InP", Proc. SPIE 9370, Quantum Sensing and Nanophotonic Devices XII, 93702W (2015)

[31] L. J. Orbe, G. Carpintero, G. Maisons, C. Gilles, F. Boulila, M. Carras, "MIR Photonic Integrated Circuits for Laser Spectroscopy," MIOMD (2014)

[32] L. J. Orbe, G. Carpintero, C. Gilles, F. Boulila, G. Maisons, M. Carras, "Characterization of an InGaAs/InP-based Echelle Mirror Multiplexer for Widely Tunable Mid-IR Sources Based on Quantum Cascade Lasers," SPIE Photonics West (2015)

[33] L. J. Orbe, C. Gordon, G. Carpintero, G. Maisons, M. Carras, "InGaAs/InP-based Echelle mirror multiplexer using dual Rowland circle gratings for DFB QCL arrays in the mid-long infrared range," SPIE Photonics West (2014)

[34] PARADIGM/EuroPIC Design Manual, Jeppix (2012)

[35] Mickael Brun, Pierre Labeye, Gilles Grand, Jean-Michel Hartmann, Fahem Boulila, Mathieu Carras, and Sergio Nicoletti, "Low loss SiGe graded index waveguides for mid-IR applications," Opt. Express 22, 508-518 (2014)

[36] Garth, S.J., "Modes on a bent optical waveguide," in Optoelectronics, IEE Proceedings J , vol.134, no.4, pp.221-229, August 1987

[37] Soibel, A.; Mansour, K.; Forouhar, S.; Peabody, Milton L.; Sivco, Deborah L.; Cho, Alfred Y.; Gmachl, Claire, "Y-branch optical coupler monolithically integrated with DFB quantum cascade lasers," in Lasers and Electro-Optics, 2005. (CLEO). Conference on , vol.2, no., pp.863-865 Vol. 2, 22-27 May 2005

Optical Multiplexer Design for Broadly-Tunable QCL Sources

3.1 - Introduction to optical multiplexer design in the MIRIFISENS platform

The main objective within this thesis has been to develop a widely tunable the mid-infrared (Mid-IR) source.

The novel approach that we have pursued is using photonic integration techniques to combine the light from an array of DFB-QCL emitters onto a common output waveguide using an integrated multiplexer structure. On its own, developing an integration platform in the MIR region is an ambitious goal, which will benefit many other areas of application. Our objectives is focused on combining multiple DFB-QCL sources and demonstrate the cost and size reduction, as well as the performance enhancement brought by the use of photonic integration techniques.

Single DFB-QCLs present very narrow tuning range, on the order of few nanometers, which is the major limitation of the development of these sources. The wavelength varies with temperature, at a rate of 0.09 $cm^{-1}/^{o}K$ over in a -30 to +30 ^{o}K range in a continuous wave (CW) operation [8] Efforts achieve tunability rates between 0.05 and 0.18 $cm^{-1}/^{o}K$ in pulsed devices [9] . Wavelength can be also varied through the Injection current, which basically modifies the temperature. The rate of change that has been reported is 2.26 ± 0.03 cm^{-1}/A over a range of about 400 mA [10] .

In our approach, using an array of DFB-QCL emitters, each emitter in the array is slightly detuned over the adjacent ones, each emitting at its own output facet, therefore the

direct use of the array as a single output source requires additional efforts to combine the different outputs into a common output[11] [12] [13] . This is the main component that we have designed within this thesis. The multiplexer design for this application must be applied to ensure monolithic integration of both the DFB-QCL sources and the multiplexer structures as the MIRIFISENS project objectives dictate.

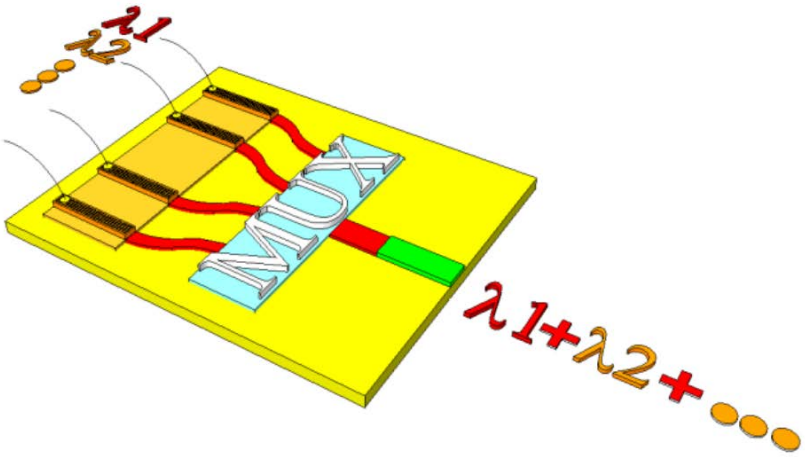

Figure 3.1. Scheme of the final broad band mid-infrared source based on a QCL array.

In order to achieve this objective, the design of multiplexer structures is proposed by the use of Building Blocks, based on the epilayer structure and parameter values as defined in Chapter II.

The work, as detailed on this chapter is to show the applied methodology for the design and application of two different multiplexer schemes, such as the Y-junctions and the Echelle mirrors. Their advantages and disadvantages are also mentioned as the comparison between them is addressed.

3.2 - Y-Junction based multiplexer structures

The first option that we have considered is to use a multiplexer structure is to gradually merge all the sources, through a sequence of 2-to-1 Y-junction combiners. This is the simplest approach, lacking compactness and might pose a problem on the chip size as one increases the number of emitters to widen the tuning range. The general structure of this multiplexer is shown in Figure 3.2.

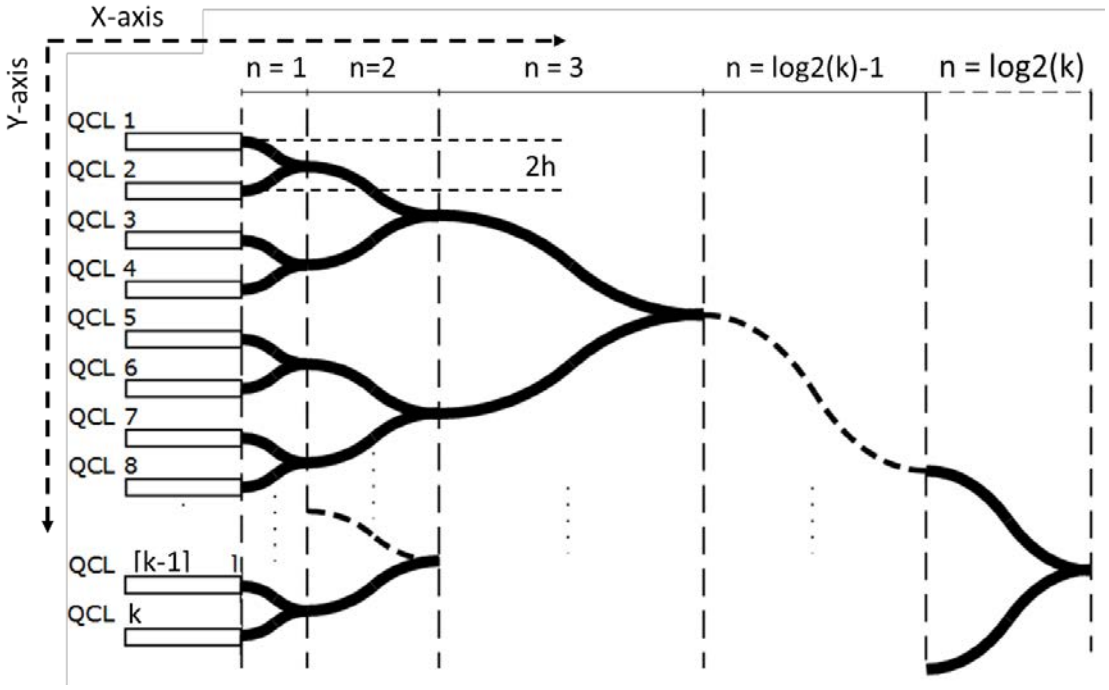

Figure 3.2. Diagram of a monolithically integrated QCL multiplexer as a function of the number of "k" lasers in the array.

Where **h** is the offset of a single S-bend and 2h defines the separation between two adjacent light sources. As shown, the structure allows combining k inputs into a single output, with the number of such inputs being a two's power. This means that the number of inputs must be rounded up to the nearest power of two of the number of emitters.

As the number of individual DFB-QCLs in the array that we aim to combine is 30, the design is optimized to multiplex a total of 32 inputs, n = $\log_2(k)$, where **k** is the number of lasers in the array. This design definition also helps us to define the parameter **n**, the multiplexing level. A design with a parameter value n=1 can only multiplex up to 2 inputs; a n=2 multiplexer design can multiplex up to 4 inputs in a two level configuration; this means that it is necessary to first multiplex each pair of laser sources into a single output, and then, in a different level, multiplex those outputs into a new single output.

In order to estimate the size of the chip, we can observe that the vertical dimension is determined by the offset level of the S-bend Y-junction BB (as described in Chapter II), which increases for larger **n** values. If we would want to define this offset as a function of the multiplexing level, the relation can be defined as

$$offset\ (n) = 2^n h \qquad \text{Eq. 3.1.}$$

In the DFB-QCL arrays of the III-V platform, the spacing between adjacent emitters is 100 μm. Working out the size of the chip area required for the Y-junction combiner of n elements we find that

$$\begin{aligned} y &= 2h(2^n - 1) \\ x &= \sum 2^{n-1}\pi(2h)(R_{min}) \end{aligned} \qquad \text{Eq. 3.2.}$$

Where **y** is the axis at which the input laser sources are located and **x** is the direction where the single output of the multiplexer is located. Using these relations, and using the R_{min} value of 170 μm calculated previously as the minimum radius for the bent waveguides,, we obtain the area occupied by the multiplexer for an increasing value of

multiplexer levels (n). A visualization of the increasing of the x/y axis in the multiplexer design as a function of the multiplexer level **n** is shown in Figure 3.3. This figure is complemented by Figure 3.4, where the total footprint of the resulting device is shown in μm^2.

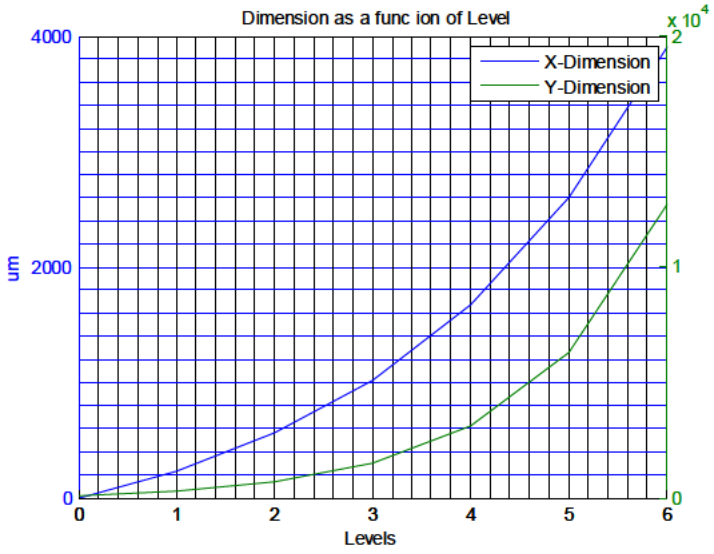

Figure 3.3. X-Y dimensions in μm for an integrated S-bend based multiplexer as a function of the multiplexer level "n"

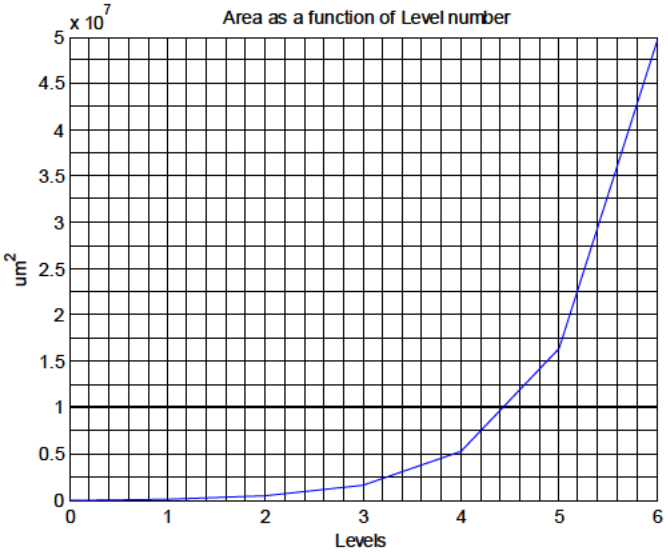

Figure 3.4. Footprint area in μm^2 of an integrated S-bend based multiplexer as a function of the multiplexer level "n"

Given this multiplexer level based approach, we can define the total losses of the device as a function of the propagating wavelength **λ** and the multiplexer level **n** as:

$$Total\ loss(n,\lambda) = \left(\sum_{1}^{n}\left[\int_{0}^{L(n)}\left[\sqrt{1+[F_{Sbend}(x)]^2}dx\right] + FPR(n)\right], \lambda\right)$$

Where:

- L(n) is the S-bend length of the multiplexer level n over the x-axis
- $F_{Sbend}(x)$ is the bend function (Chapter II)
- FPR(n) is the losses due to reflections and higher order modes in the free propagating regions of each Y-junction

Following the building block definition, we can define this multiplexer scheme as a higher level BB conformed of multiple S-bend Y-junction coupler BBs. Table 3.1 describes the BB components and shows a detailed schematic of the S-bend Y-junction scalable multiplexer as a function of the S-bend 2-to-1 Y-junction couplers; in the figure, each white square represents a single S-bend 2-to-1 Y-junction multiplexer.

Building block name	**S-bend Y-junction scalable multiplexer**
Input parameters	Identifier
Number of inputs	N
Waveguide width	w
Radius	R
Laser source separation	2h
S-Bend type	No identifier (Sine or Cosine)
Output parameters	Identifier
Device length	L
Multiplexer level	n

Table 3.1. BB definition for an S-bend Y-junction based scalable multiplexer

Figure 3.5 shows the number of light sources as the base for the design of scalable multiplexers in the form of Building Blocks, as they are applied for defining the total device length.

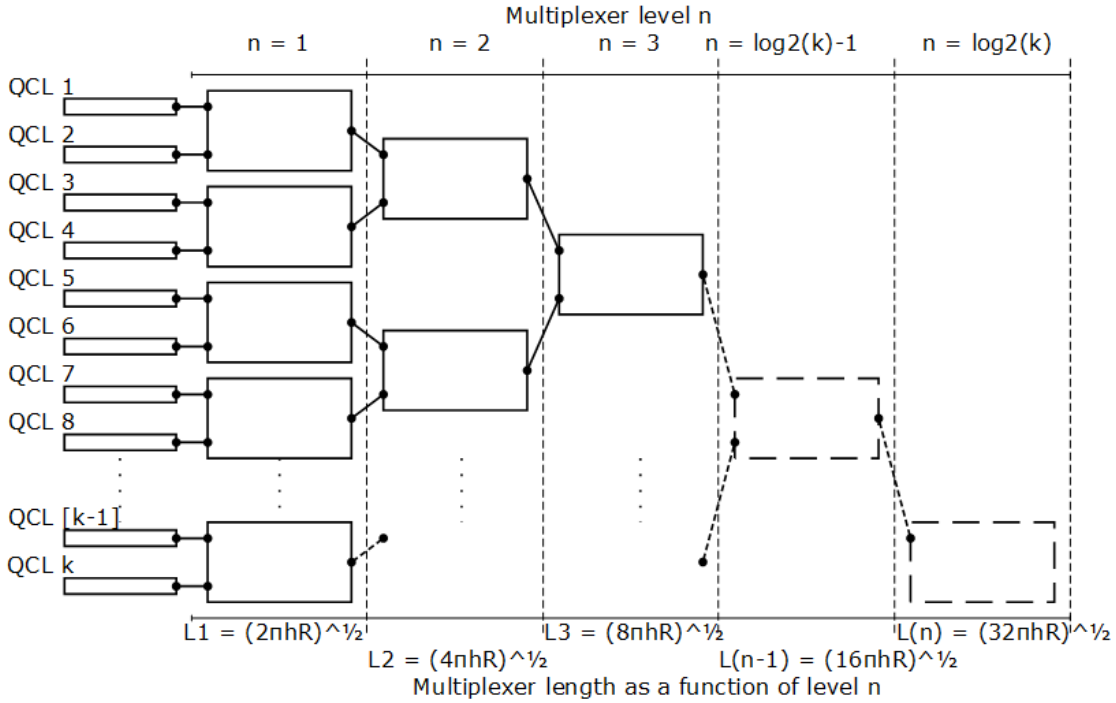

Figure 3.5. Diagram of a monolithically integrated QCL multiplexer as a function of the number of lasers in the array, axis show the multiplexer level n (top) and the length of individual multiplexer levels (bottom)

With this description, the scalability of the BB approach for the design of multiple input (de)multiplexer schemes is demonstrated and provides a better visibility of the parameter values for each section, reducing design effort, as several BBs are reused, and improving the monolithic design capabilities, as the passive and active components in the design are described as individual blocks.

3.3 - Echelle grating based multiplexer structures

Wavelength (de)multiplexers have recently been fabricated in the MIR spectral range on different platforms to obtain single output broadly tunable sources. Arrayed waveguide grating (AWG) and planar concave grating (PCG) have been demonstrated on a silicon-on-insulator platform at a wavelength of 3.8 μm [14] . Despite the performances of these devices, SiO2 exhibits a strong absorption at longer wavelength limiting further developments of this platform in other regions of the MIR [15] . Therefore, AWG [16] and PCG [17] multiplexers have been reported on germanium-on-silicon benefiting from a larger transparency window up to 14 μm [15] .

However, the integration between the multiplexer input waveguides and DFB laser arrays requires a coupling scheme between the two chips, usually bringing these two platforms together through butt-coupling. Robust alignment procedure and high coupling efficiency without parasitic reflections leading to laser perturbations can be nevertheless difficult to achieve.

III-V semiconductor waveguides based on Indium Phosphide(InP) and Indium Gallium Arsenide (InGaAs) materials have the advantage of exhibiting very low absorption across the whole MIR region from the absorption edge at high photon energies [18] down to a wavelength of 14 μm, where multi-phonon absorption features and free carrier absorption become significant [19] . In addition, two-photon absorption and sidewall roughness, which slow down the development of InP in the telecom wavelength bands, are

no longer consider as major loss mechanisms in this region. Integrating wavelength multiplexers with light generation and detection elements on the InP platform would therefore benefit to the development of broadband and scalable complex photonic integrated circuits in the MIR.

However, requirements for wavelength multiplexing of laser arrays are different from those that are expected for wavelength-division multiplexing (WDM) in fiber-optic communications. The newly defined figures of merit for wavelength multiplexers and designed transmission spectra for each wavelength channel are illustrated in Figure 3.6. The spectral coverage represents the range of wavelengths covered by the multiplexer and should be large to exploit the full potential of the strong absorption features in the MIR. The channel spacing, corresponding to the wavelength pitch between adjacent inputs, has to be narrower than the tunability range of one single emitter of the laser array to obtain continuous tuning over the spectral coverage.

The channel passband, defined as the wavelength range at which the relative power decreases 3 dB below the maximum power, is required to be large, and as flattened as possible in multiplexers to get good power uniformity from the single-output waveguide. The channel crossing is defined as the ratio of power transmission of a channel at its central wavelength with the power transmission of this channel at the crossing with adjacent channels. A small channel crossing is required to obtain quasi-constant output power over the spectral coverage.

The insertion loss represents the total optical power reduction from the multiplexer and the channel crosstalk, the power transmission ratio at its central wavelength with the adjacent channel wavelength.

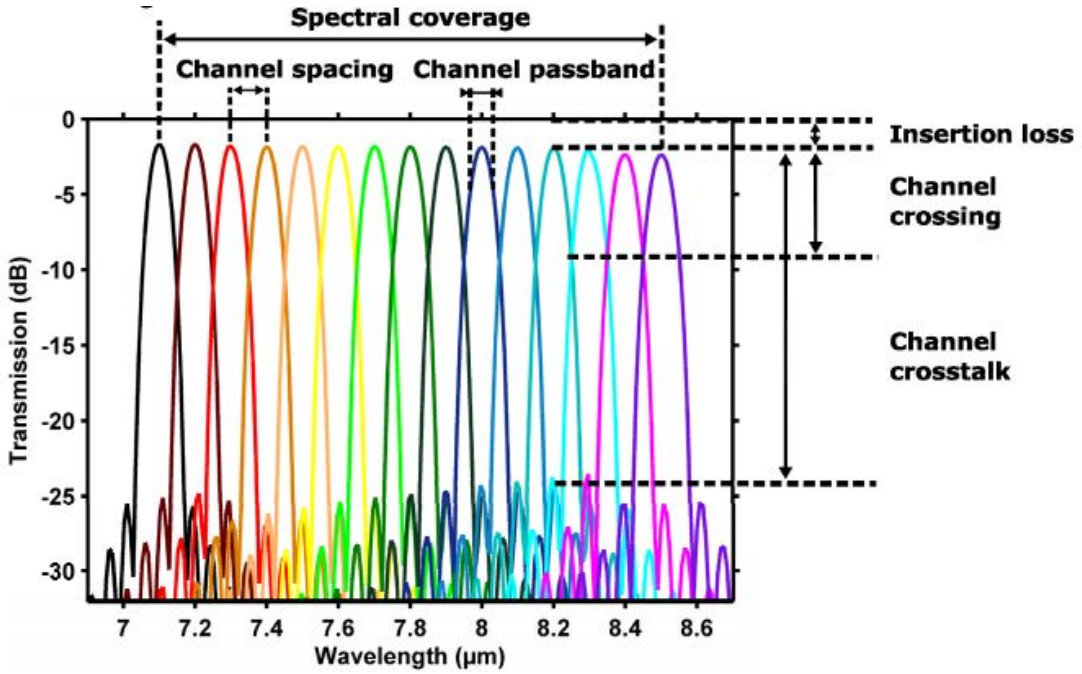

Figure 3.6. Figures of merit and designed channel transmission spectra of the multiplexer

Looking for a compact and area efficient multiplexers, we turned to Echelle grating multiplexers. An Echelle grating (or diffraction grating) is an optical component used to spatially separate the different constituent optical frequencies combined in an optical beam. As the beam arrives to its surface, each wavelength component is reflected with a different angle.

A diffraction grating is an optical component with a periodic structure, which splits and diffracts light into several beams travelling in different directions. The relationship between the grating spacing and the angles of the incident and diffracted beams of light is known as the grating equation.

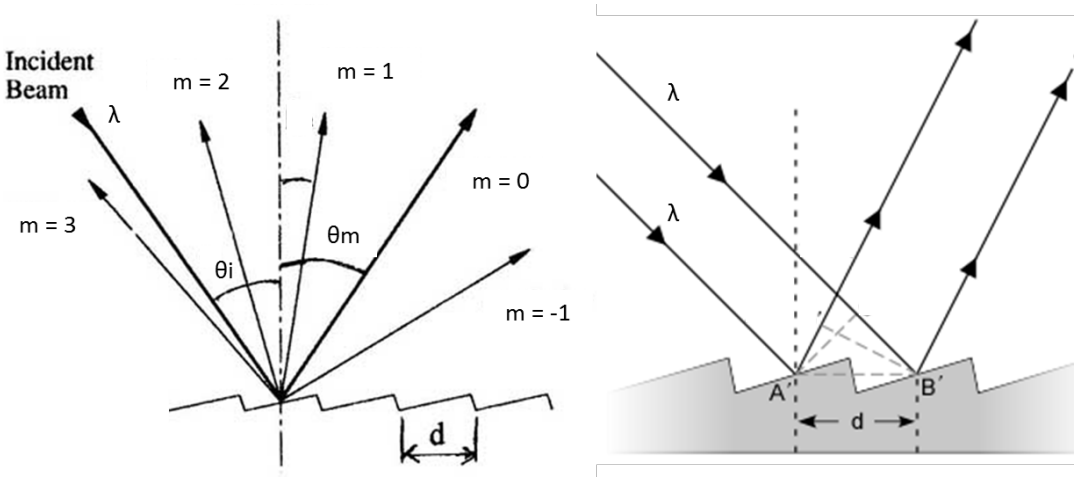

Figure 3.7. Depiction of the diffraction of light by a grating mirror surface into different diffraction orders (left). Depiction of the contribution of two different diffraction points in a diffraction grating (right).

According to the Huygens–Fresnel principle, each point on the wavefront of a propagating wave can be considered to act as a point source, and the wavefront at any subsequent point can be found by adding together the contributions from each of these individual point sources.

Gratings may be of the reflective or transmissive type, analogous to a mirror or lens respectively. A grating has a zero-order mode (where m= 0), in which there is no diffraction and a ray of light behaves according to the laws of reflection and refraction the same as with a mirror or lens respectively [20] .

An idealized grating is considered here which is made up of a set of slits of spacing ***d***, that must be wider than the wavelength of interest to cause diffraction. Assuming a plane wave of monochromatic light of wavelength λ with normal incidence (perpendicular to the grating), each slit in the grating acts as a quasi point-source from which light propagates in all directions (although this is typically limited to a hemisphere). After light interacts with the grating, the diffracted light is composed of the sum of interfering wave components

emanating from each slit in the grating. At any given point in space through which diffracted light may pass, the path length to each slit in the grating will vary.

Since the path length varies, generally, so will the phases of the waves at that point from each of the slits, and thus will add or subtract from one another to create peaks and valleys, through the phenomenon of additive and destructive interference. When the path difference between the light from adjacent slits is equal to half the wavelength, $\lambda/2$, and the waves will all be out of phase, and thus will cancel each other to create points of minimum intensity. Similarly, when the path difference is λ, the phases will add together and maxima will occur. The maxima occur at angles θ_m, which satisfy the relationship $d \sin\theta_m/\lambda = |m|$, where θ_m is the angle between the diffracted ray and the grating's normal vector, and $\boldsymbol{d}$ is the distance from the center of one slit to the center of the adjacent slit, and $\boldsymbol{m}$ is an integer representing the propagation-mode of interest.

Echelle grating multiplexers are a solution that consists on a number of optical inputs, which deliver the light into a free propagation region (FPR), in which the light is diffracted onto a grating mirror surface. Each one of the mirrors in the surface focuses the light of each input onto an output port only if the light[20] .

In Echelle grating multiplexers, the light meets a grating surface that focuses the light from any of these inputs into a single output waveguide. Such output waveguide must be carefully located so that mode propagation is ensured and the different wavelengths present at the different input waveguides, (such is the case of a DFB QCL array) are combined into a single output [21] [22] .

These structures present the characteristic that a continuous tuning range can be obtained if adjacent input channels of the multiplexer present some spectral overlap. This spectral overlap is called channel crosstalk, and it is the design base for broad spectrum optical (de)multiplexers and combiners.

The basic Echelle grating based scheme is composed, as mentioned, by two separate sets of waveguides. These waveguides are to be located following a precise orientation, having the center of the diffraction grating as focal point, thus making direct use of the diffraction capabilities of the incident light. The typical representation of these schemes can be found in Figure 3.8.

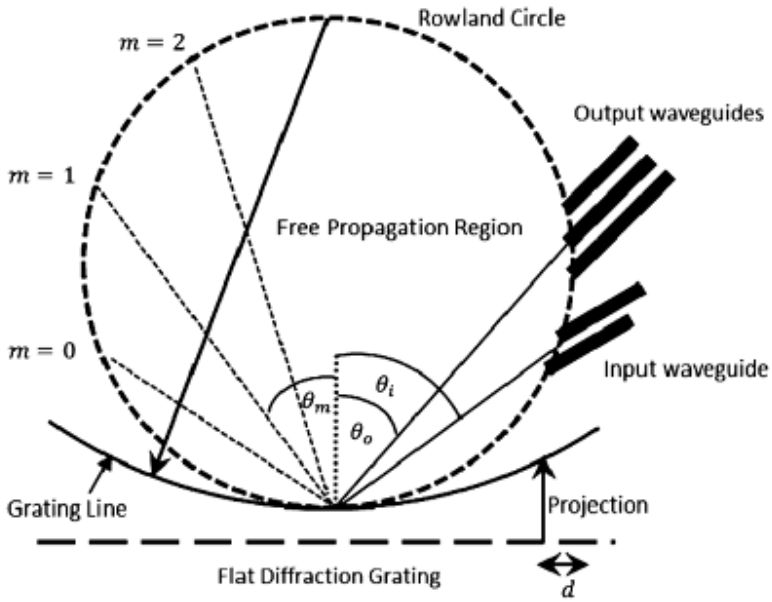

Figure 3.8. Typical Rowland circle based (de)multiplexer structure with input/output waveguides

They have been widely used in multiplexer applications in various technologies[23] [24] [25] [26] [27] ; but so far, limited work has been done in the mid-IR[21] [22] [28] [29] [30] .

In these structures, when the light that is propagated through the input waveguides and enters the free propagation region will be diffracted when it encounters the grating, with a refractive index n_{eff}, the diffracted light will be separated into different diffraction orders at angles θ_m given by the relation:

$$d \sin \theta_m = \frac{m\lambda}{n_{eff}} \qquad \text{Eq. 3.3.}$$

It is straightforward to show that if a plane wave is incident at any arbitrary angle θ_i, the grating equation becomes:

$$d \left(\sin \theta_i + \sin \theta_m\right) = \frac{m\lambda}{n_{eff}} \qquad \text{Eq. 3.4.}$$

When solved for the diffracted angle maxima, the equation is:

$$\theta_m = sin^{-1}\left(\frac{m\lambda}{dn_{eff}} - \sin \theta_i\right) \qquad \text{Eq. 3.5.}$$

The light that corresponds to direct transmission (or specular reflection in the case of a reflection grating) is called the zero order, and is denoted $m = 0$. The other maxima occur at angles which are represented by non-zero integers m. Note that m can be positive or negative, resulting in diffracted orders on both sides of the zero order beam.

In order to address the BB scheme, a representation of a monolithically integrated QCL Echelle grating based multiplexed source is shown in

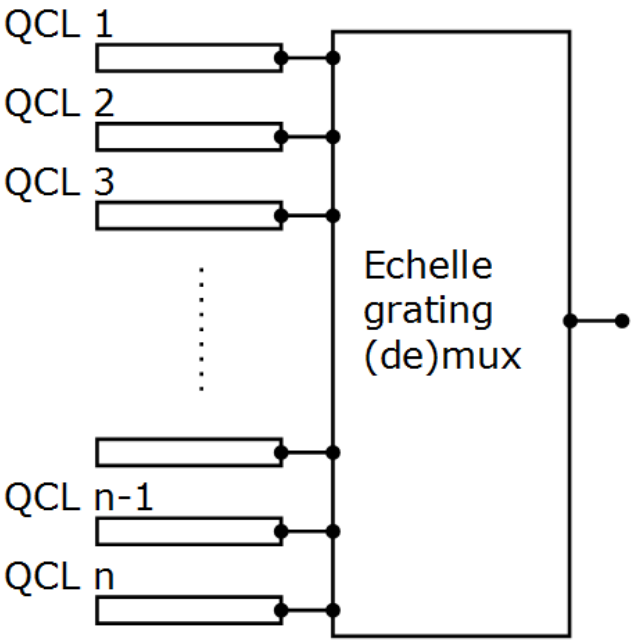

Figure 3.9. Diagram of a monolithically integrated QCL + Echelle grating based multiplexer as a function of the number of lasers in the array

As mentioned in the objectives of this work, the design of multiplexer functions to conform a monolithic tunable source with a single output is divided into two different wavelength ranges:

- 7.00 – 8.50 μm (1176.5 – 1428 cm^{-1}) with 30 input channels
- 7.00 to 10.00 μm (1000 - 1428 cm^{-1}) with 30 input channels

The device design for each of those wavelength range requirements will be treated separately, in the following sections.

3.3.1 - Design and optimization methodology

The fundamentals for the design of Echelle grating based multiplexers are the diffraction equation for the different diffracted modes (Eq. 3.4). However, additional restrictions can be introduced in order to ensure compatibility with the fabrication stages.

The preliminary data for an accurate design requires the use and validation of a certain number of parameter values, which are also necessary for the definition of the Echelle based (de) multiplexer building block. This definition is shown Figure 3.10(a) and it is detailed in Table 3.2.

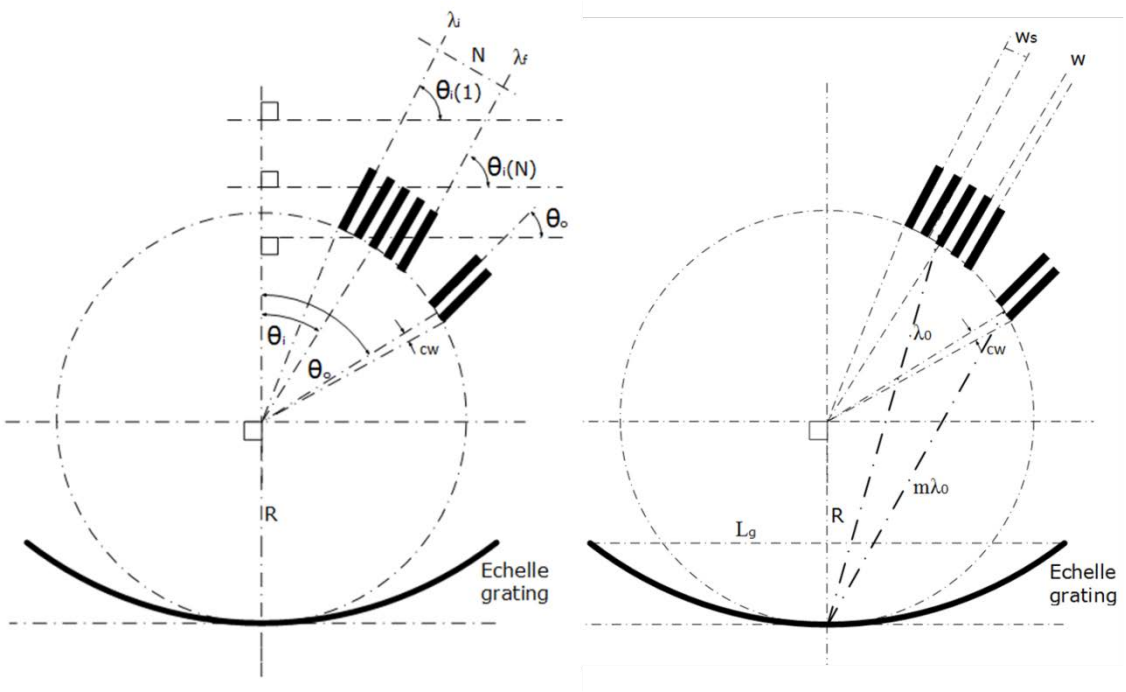

(a)

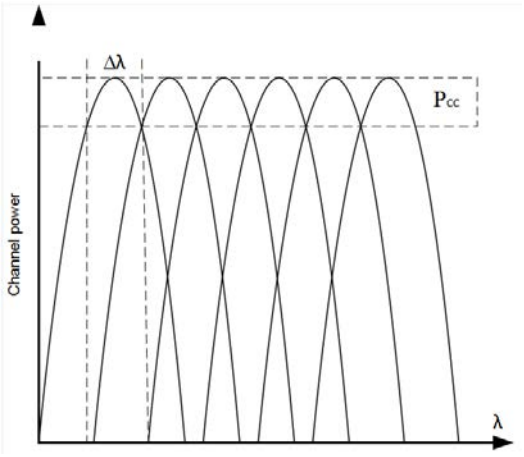

(b)

Figure 3.10. Parameter values for the Echelle grating design (a) and output spectra (b)

Building block name	**Echelle grating multiplexer**
Input parameters	Identifier
Number of input waveguides	N_{in}
Number of output waveguides	N_{out}
Waveguide width	w (μm)
Cladding width	c_w (μm)
Initial wavelength	λi (μm)
Final wavelength	λf (μm)
Incidence angle of the input waveguides	θin (°)
Diffraction order	M
Output parameters	Identifier
Rowland radius	R (μm)
Device footprint area	A
Incidence angle of the output waveguides	θout (°)
Central wavelength	λ_0 (μm)
Channel width	Δλ (μm)
Effective index	neff
Waveguide spacing	w_s (μm)
Channel crossing level	Pcc (dB)
Grating length	L_g (μm)

Table 3.2. Building block definition of a Echelle grating (de) multiplexer

As can be observed, some of those parameters do not have a straightforward setting and must be obtained through other means. The methodology for their calculation involves the following steps which are taken sequentially in the order that are introduced [20] .

- Define the wavelength range (bandwidth) and the incident angle.

Is necessary to define the incidence angle respect to the center of the Rowland circle. As it serves as reference for the focal point of the incident waveguides. At this point, the definition of the wavelength range is necessary in order to predefine the footprint area of the overall structure. This parameter allows for the definition of the initial (λi) and final (λf) wavelengths, which are introduced by a number of input waveguides (Nin) into the structure. At this point we can define the channel width, which is the absolute difference in initial and final wavelengths that are introduced into the propagating region through a waveguide.

$$w_{Bw} = \frac{w_f - w_i}{N_{in}} \qquad \text{Eq. 3.6.}$$

However, this relation does not take into consideration the channel width loss due to the cladding surrounding the propagation region of the waveguide. Special attention must be put into this detail, as the waveguide losses for the light not correctly centered into the waveguide are considerable.

At this step, the central wavelength can be easily inferred by the relation:

$$\lambda_0 = \frac{\lambda_i + \lambda_f}{2} \qquad \text{Eq. 3.7.}$$

This parameter is used as a landmark for the simulations of the device, as its calculation implies the localization of the center of the input waveguide array.

- Perform a waveguiding analysis for the input and output waveguides.

Modal behavior of the waveguides is important to determine the correct approach to study the propagation and the mode conversion over the light path. The effective index (neff) of the mode is a mayor indicator for the possibility of mode conversion or confinement loss through the input and output waveguides.

- Perform a coupling analysis.

Once the effective index of the propagating mode is set, a coupling analysis is necessary to calculate the minimum separation between two adjacent waveguides. As this was mentioned before, is directly related to the minimum channel width.

Limitations in the resolution and tolerances in the fabrication procedures also limit the channel width, as the waveguide cladding is taken into account for it.

- Calculate the Rowland radius and the diffraction angles of the input and output waveguides

The Rowland circle radius defines the number of the input and output waveguides. Given the basic structure of the Echelle grating based multiplexer (Figure 3.8) is easily observable that the number of input waveguides, as well as their width and cladding space take a major role in the footprint definition of the structure. The angle created by the area

inside the two limiting waveguides is defined as the input array angle $\theta_{in\ array}$, and it is defined as a function of the waveguide width and cladding as follows:

$$\theta_{in\ array} = \frac{N_{in}(wgw + wgc)}{R} \qquad \text{Eq. 3.8.}$$

Where R is the Rowland radius. Related to the application, it is recommended that this Rowland radius is large enough so that $\theta_{in\ array} < 90^{o}$, otherwise the device performance could be affected if low diffraction mode values are selected for mode propagation.

- Calculate the diffraction angles for the input and output waveguides

The fundamental equation in the optimization of the Echelle Grating Wavelength Multiplexor is the Standard diffraction. This equation allows defining the position of the waveguide array. If we know the period of the grating, the angle of incidence, the order of diffraction, the wavelength in the free space and the refractive index of the mode in the slab waveguide, we can work out the angle of the diffraction associated with an order of diffraction by using Eq. 3.3

Along with this calculation, it is important to establish the optimum waveguide spacing. This parameter depends on the input angle and the width of the waveguide and allows the size optimization of the Rowland.

3.3.2 - Rowland grating design for the 7.0 – 8.5 μm wavelength range

Following the aforementioned methodology, we design two different multiplexer schemes for two different wavelength ranges, for the completion of the MIRIFISENS project objectives.

The first is a 7.0-8.5 μm 30-to-1 (de)multiplexer. A safe design approach was taken as this is the first design of these structures in the III-V platform and it is necessary to get a good idea of the limitations applicable to these designs. As the DFB-QCL sources present a TM polarization, this additional design requirement is taken into account for minimizing fundamental mode losses in the resulting device.

In order to comply with this design, the proposed input parameters for the BB are given in the next table.

Building block name	**Echelle grating multiplexer**
Input parameters	Identifier
Number of input waveguides	30
Number of output waveguides	1
Waveguide width	6 μm
Cladding width	1 μm
Initial wavelength	7.0 μm
Final wavelength	8.5 μm
Incidence angle of the input waveguides	0º
Diffraction order	1

Table 3.3. Input parameters for the 7-8.5 μm Echelle grating based (de) multiplexer

Where diffraction order 1 is selected as the most basic scheme, suitable for error and deviation measurements if any were to appear during the fabrication process. The incidence angle of the input waveguides was designed to be perpendicular to the center of the grating; this way no blazing or angle compensation is necessary for the diffraction facets over the grating.

A series of simulations were done in order to visualize the device spectrum. These simulations were done using the commercial software EPIPPROP by PhotonDesign.

Given the nature of the simulation over a free propagation region and the large number of reflections to consider, an FMM simulation was done over the cross section of the input and output waveguides, the resulting mode calculations for the fundamental TE and TM modes were introduced into a FDTD simulation of the Echelle grating multiplexer.

The results of such simulations for the fundamental TE and TM modes, based on the data from Table are shown in Figure 3.11.

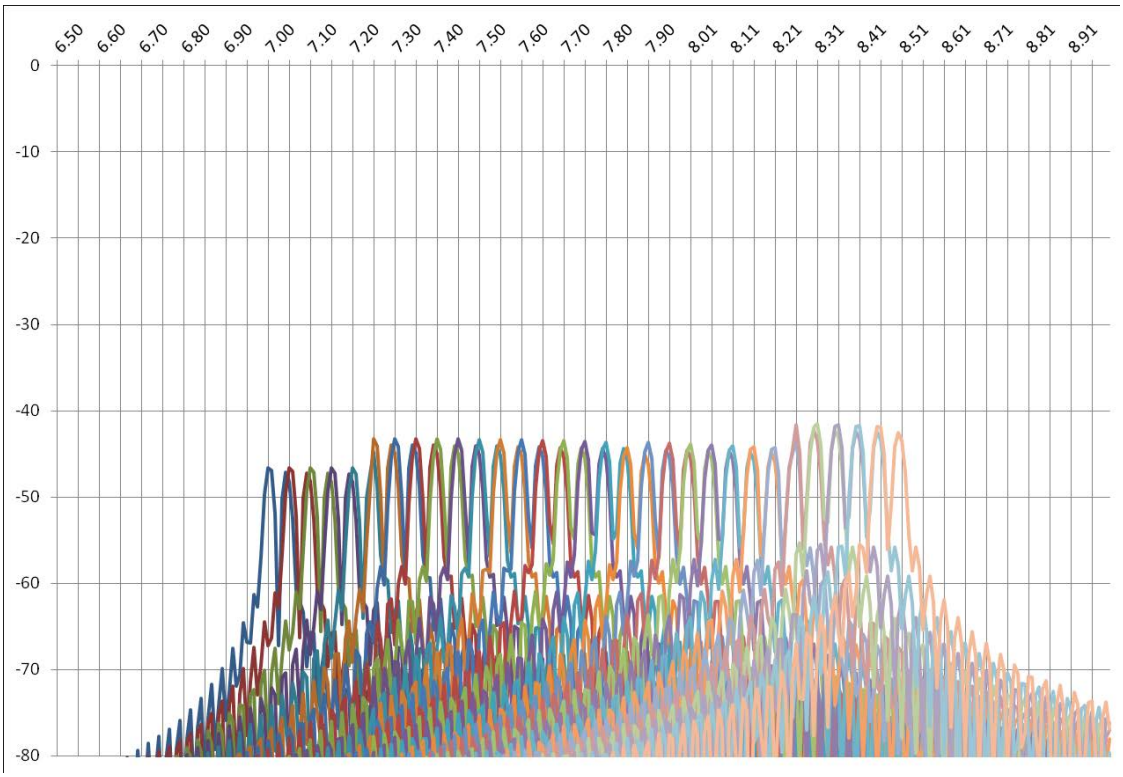

(a)

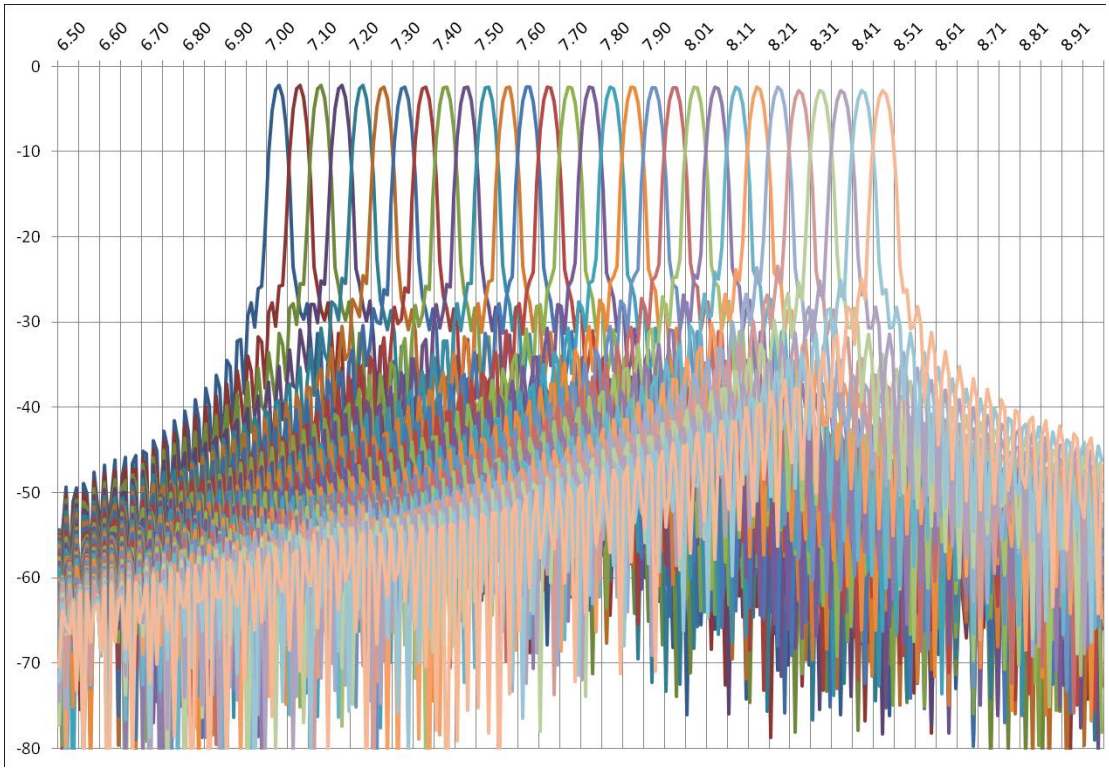

(b)

Figure 3.11. Simulation results showing individual input channels of a 30-to-1 Echelle grating based (de)multiplexer for TE (a) and TM (b) fundamental modes for the 7.0-8.5 μm wavelength range

The resulting spectrum shows the expected transmission level between the inputs and outputs of the Echelle grating based multiplexer when light is propagated through the device and gets diffracted in the diffraction mirror. The simulation for the TE polarization shows insertion losses between 46.5 and 42 dB. In the same way, the simulation for the TM polarization presents insertion losses between 2.5 and 3.2 dB. The difference between these insertion losses lay in the diffraction angle for both TE and TM polarizations.

At it has been defined before, the channel crosstalk and the starting crossing level in these devices are of the outmost importance as a small channel crossing is required to obtain quasi-constant output power over the spectral coverage. This simulation results allow obtaining the channel crosstalk for both TE and TM modes. In the case of the TE fundamental mode, the simulation shows channel crossing level ranges from 14 to 16 dB and between 6 and 9 dB for the TM fundamental mode.

However, the design methodology and simulations show that a device following this design parameter values result in a very large Rowland radius (>2000 μm) which would severely increase the device footprint and affect any design optimization effort.

In order to comply with these observations, a variation of the building block for the Echelle grating design is proposed in order to divide the main design into a number of subdesigns; each including the same number of inputs and a single output to be coupled in a later step to a single output design.

Figure 3.12 shows a diagram of this subdivision proposal for a monolithically integrated QCL multiplexer as a function of the number of lasers in the array, illustrating the subdivision into two subdesigns.

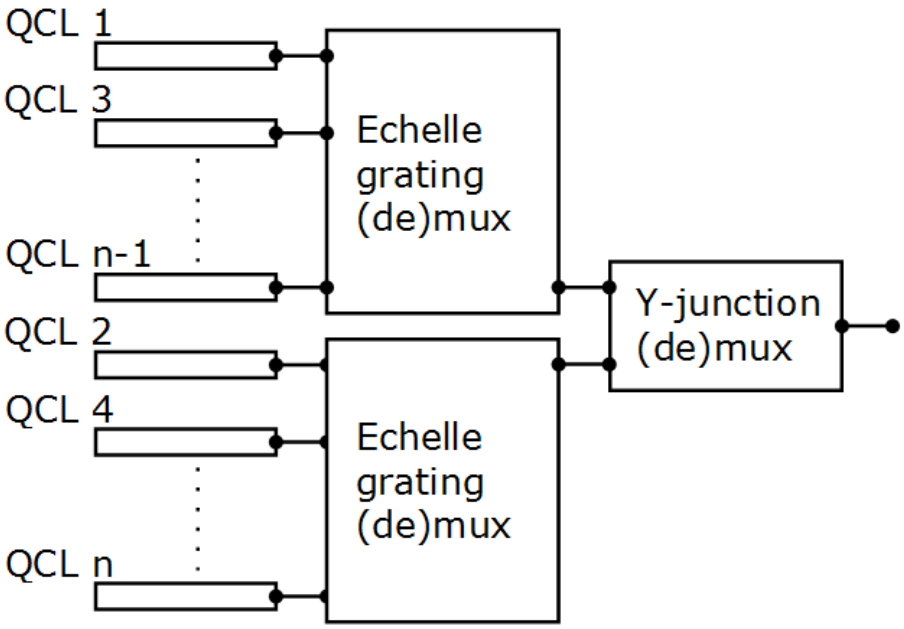

Figure 3.12. Diagram of a monolithically integrated QCL dual Echelle grating based multiplexer as a function of the number of lasers in the array

As it can be observed, this effort supposes a modification in the central wavelength for which each channel is designed, as shown in Figure 3.13. The channel spacing (wavelength range of a channel) is divided according to the number of subdivisions of the original BB.

This figure illustrates the division of the input channels (Ni) of a device wavelength range when the original design is divided into two different "subdevices" (individual Echelle grating multiplexers).

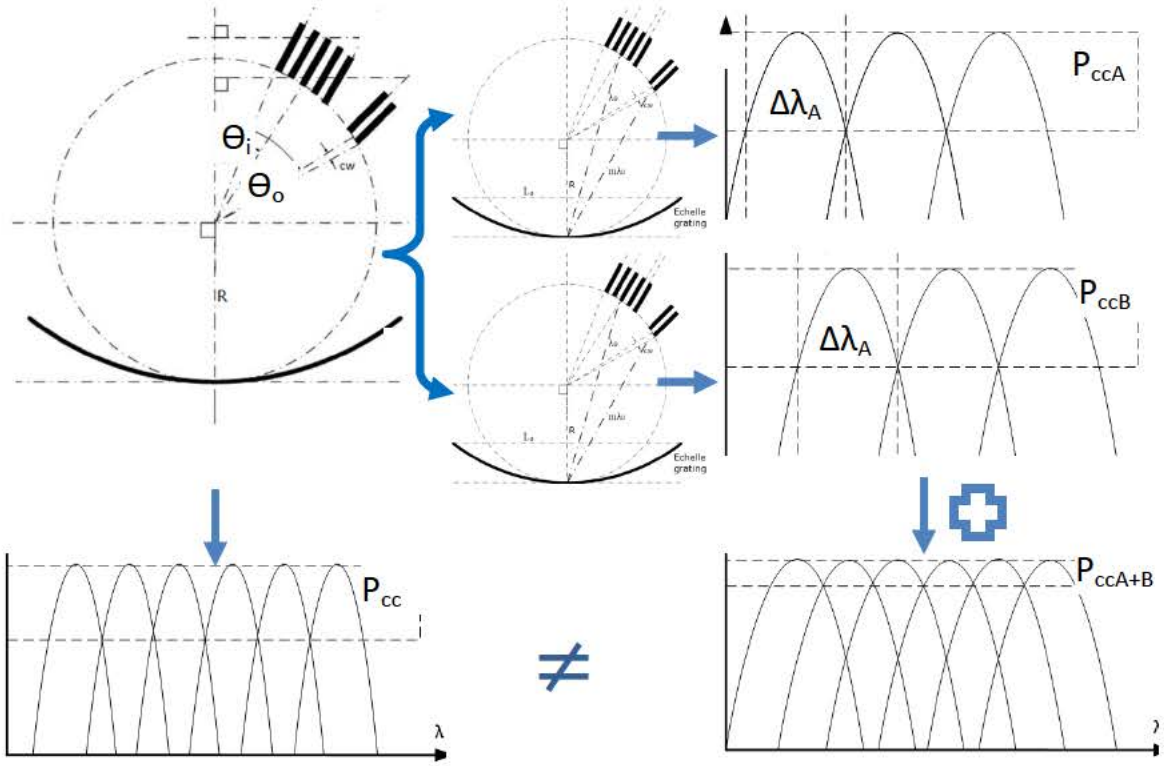

Figure 3.13. Spectral division for the output channels of an Echelle multiplexer as a result of the subdivisions of the original multiplexer

We can observe in the increasing in channel width as a function of the number of subdesigns the original scheme is divided. Following this scheme, a variation in the BB is proposed.

With this design modification, the new Echelle grating multiplexer BB variation into subdivisions can be defined with the following parameter definition:

Building block name	**Echelle (de)mux A**	**Echelle (de)mux B**
Input parameters	Identifier	Identifier
Number of input waveguides	N_{inA}	N_{inB}
Number of output waveguides	N_{outA}	N_{outB}
Waveguide width	w (μm)	
Cladding width	c_w (μm)	
Initial wavelength	λi (μm)	
Final wavelength	λf (μm)	
Central wavelength of the initial waveguide	λAi (μm)	λBi (μm)
Central wavelength of the final waveguide	λAf (μm)	λBf (μm)
Incidence angle of the input waveguides	θAin (°)	θBin (°)
Diffraction order	M	
Output parameters	Identifier	Identifier
Rowland radius	R_A (μm)	R_B (μm)
Device footprint area	A_A	A_B
Incidence angle of the output waveguides	θoutA (°)	θoutB (°)
Central wavelength	λ_{0A} (μm)	λ_{0B} (μm)
Channel width	$\Delta\lambda_A$ (μm)	$\Delta\lambda_B$ (μm)
Effective index	$neff_A$	$neff_B$
Waveguide spacing	w_{sA} (μm)	w_{sB} (μm)
Channel crossing level	P_{ccA} (dB)	P_{ccB} (dB)
Grating length	L_{gA} (μm)	L_{gB} (μm)

Table 3.4. Building block definition of a Echelle grating (de) multiplexer

According to this parameter redefinition, a subdivision into two subdesigns was proposed as a feasible way to reduce overall propagation losses by reducing the area of the free propagation region of the final device. This becomes clear by observing the output parameters for both subdesigns when modifying the definition of the BBs. These parameters are presented in Table 3.5.

Building block name	**Echelle (de)mux A**	**Echelle (de)mux B**
Input parameters	Identifier	Identifier
Number of input waveguides	15	15
Number of output waveguides	5	5
Waveguide width	6 μm	
Cladding width	1 μm	
Initial wavelength	7.0 μm	
Final wavelength	8.5 μm	
Central wavelength of the initial waveguide	7.00 μm	7.05 μm
Central wavelength of the final waveguide	8.40 μm	8.45 μm
Incidence angle of the input waveguides	0°	0°
Diffraction order	1	
Output parameters	Identifier	Identifier
Rowland radius	750 μm	750 μm
Device footprint area	1767145.87 μm^2	1767145.87 μm^2
Incidence angle of the output waveguides	48.59393º	48.943925º
Central wavelength	7.70 μm	7.75 μm
Channel width	0.1 μm	0.1 μm
Waveguide spacing	1 μm	1μm
Channel crosstalk level	14-16 dB for TE / 6-9 dB for TM	14-16 dB for TE / 6-9 dB for TM
Grating length	750 μm	750 μm

Table 3.5. Design and output parameters for the 7-8.5 μm Echelle grating based (de) multiplexer

As the output parameter list shows, this dual Echelle grating scheme allows for a large reduction of footprint area in comparison with the single Echelle grating BB, encouraging a theoretical reduction in transmission losses.

However, preliminary design steps following this variation in the (de)multiplexer design do not take into account posterior design steps for complete multiplexing into a single output. The solution can be easily implemented with the use of a Y-junction 2-to-1 S-bend coupler building block; allowing for a single output design (Figure 3.12).

In order to confirm the feasibility of the dual Echelle design, a series of simulations were performed for each of the subdesigns, using the parameters as listed in Table 3.5. The simulation parameters follow the same values as for the single Echelle model for comparison purposes when the individual wavelength channel and the number of input waveguides are doubled, allowing for a broader channel.

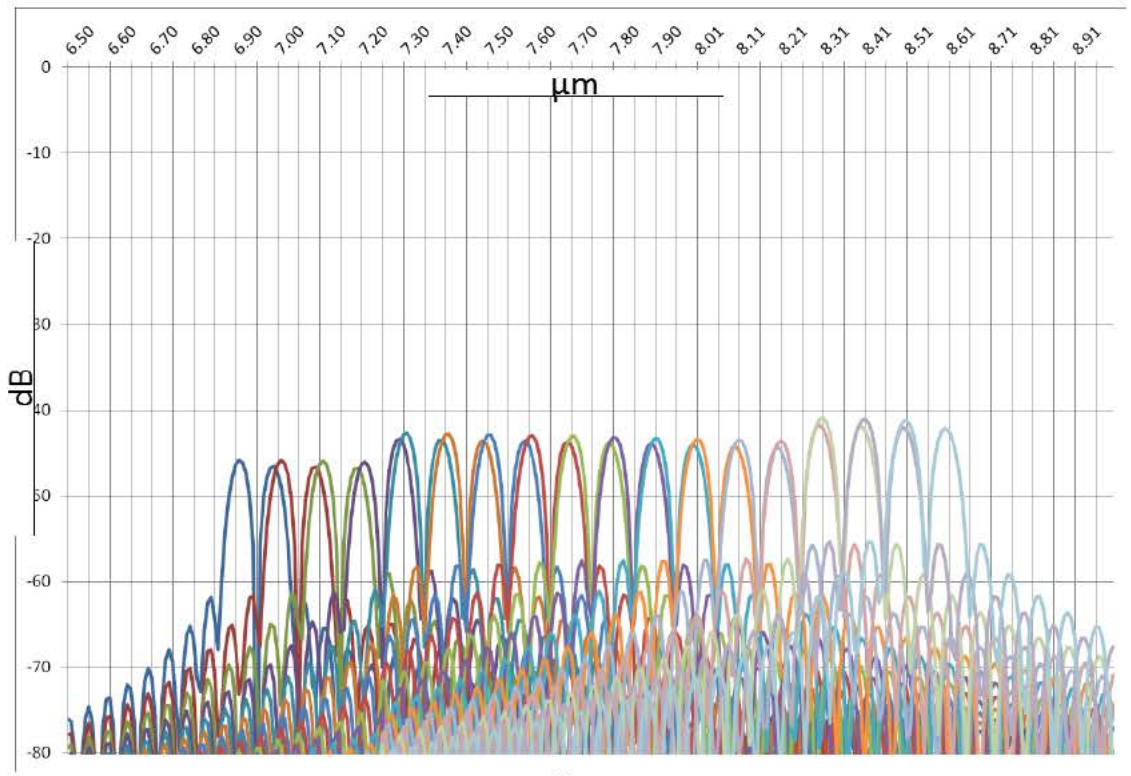

(a)

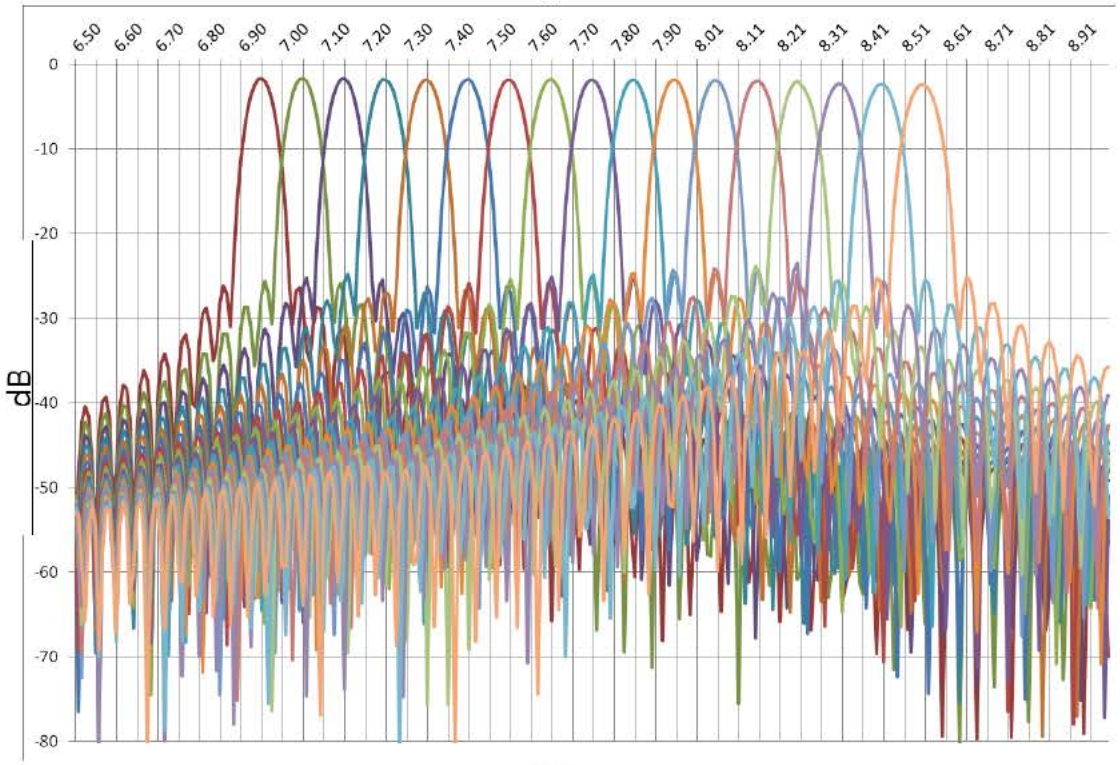

(b)

Figure 3.14.Simulation results showing individual input channels of a dual design 15-to-1 Echelle grating based (de)multiplexer for TE (a) and TM (b) fundamental modes for the 7.00-8.50 µm wavelength range

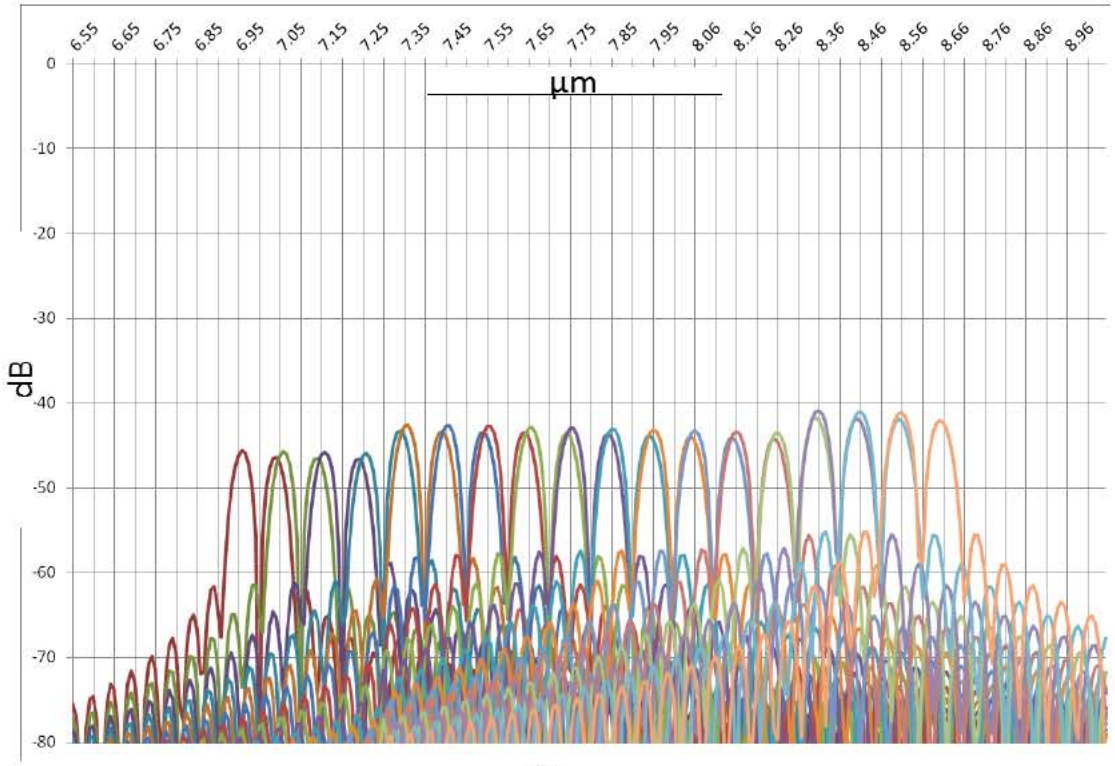

(a)

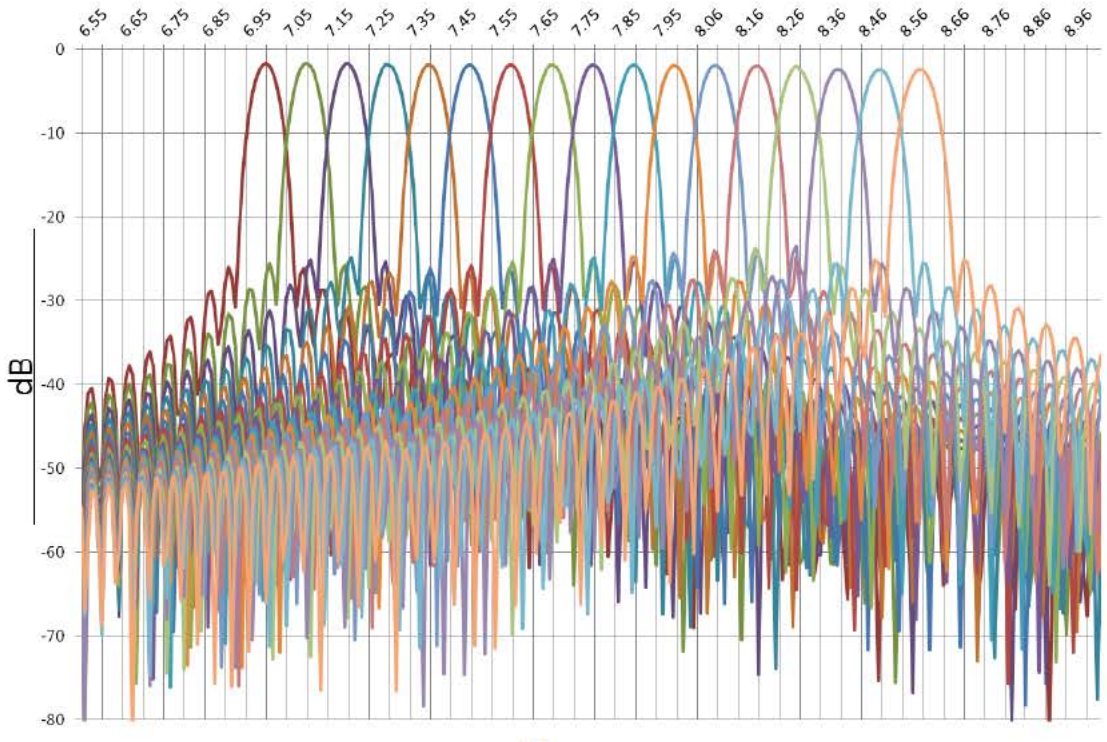

(b)

Figure 3.15.Simulation results showing individual input channels of a dual design 15-to-1 Echelle grating based (de)multiplexer for TE (a) and TM (b) fundamental modes for the 7.05-8.55 µm wavelength range

The resulting simulation spectrums for the dual Echelle grating design are shown in a separated form for both TE and TM fundamental modes at Figure 3.14 and Figure 3.15. Both figures show the simulated spectrums for the 7.00 to 8.50 μm, and the 7.05-8.55 μm wavelength ranges respectively under the parameter redefinition as shown in Table 3.5.

Observation of such figures shows similar channel crossing level behavior in comparison with the single Echelle BB (between 14 – 16 dB for the fundamental TE mode and between 6 – 9 dB for the fundamental TM mode). This similarity effect between the single Echelle grating multiplexer and the dual Echelle grating multiplexer designs allows for the identification of the interwaveguide cladding as a major source of interchannel loss, as parameter values for waveguide width, cladding width and spacing remain unchanged.

The reduction of any of such parameters will surely reduce the channel crosstalk level between adjacent channels. However, as it has been mentioned before, limitations in the fabrication procedures directly affect the minimum size resolution in the produced devices, giving as a result a minimum level in channel crosstalk, which is approximately 1 μm of cladding width for the III-V Lab fabrication procedure.

In order to show the advantages of this dual Echelle grating multiplexer approach, a new simulation was done combining the parameters for each of the Echelle multiplexer subdesigns. The simulation results, as shown in Figure 3.16, show that dual Echelle grating multiplexer schemes widen the individual channel width without compromising individual source tunability, which remains the same in comparison with a single grating model, severely reducing the interchannel crosstalk levels of the resulting transmission spectra in comparison with a single Echelle grating approach.

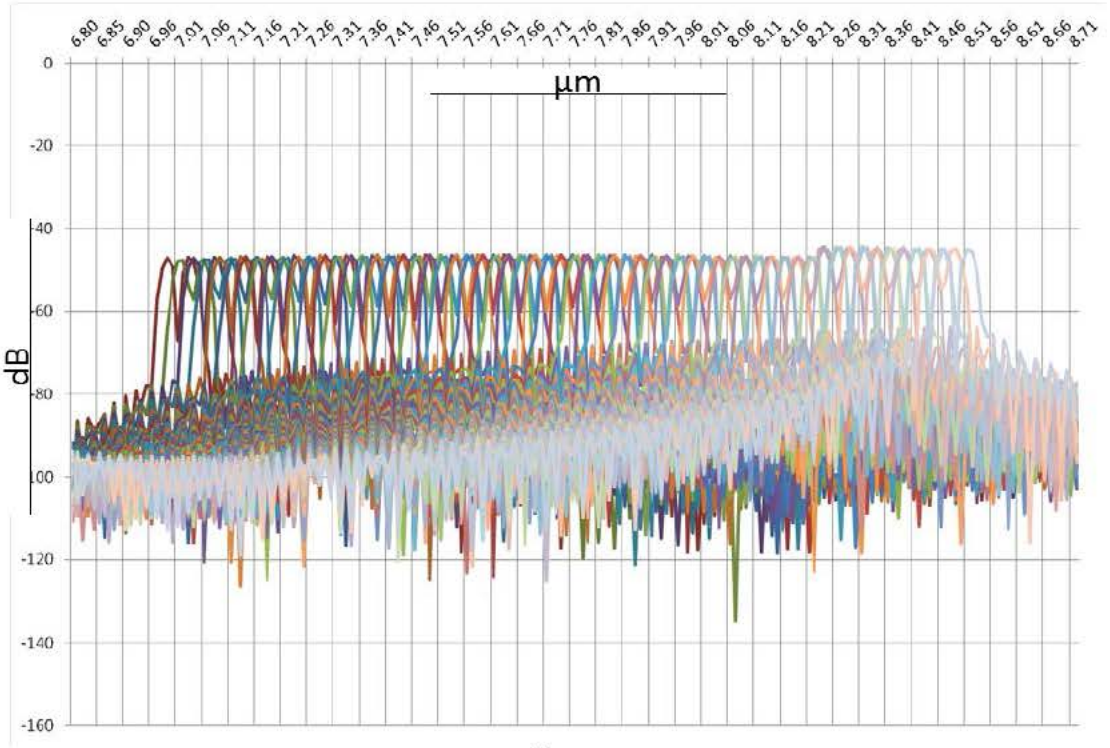

(a)

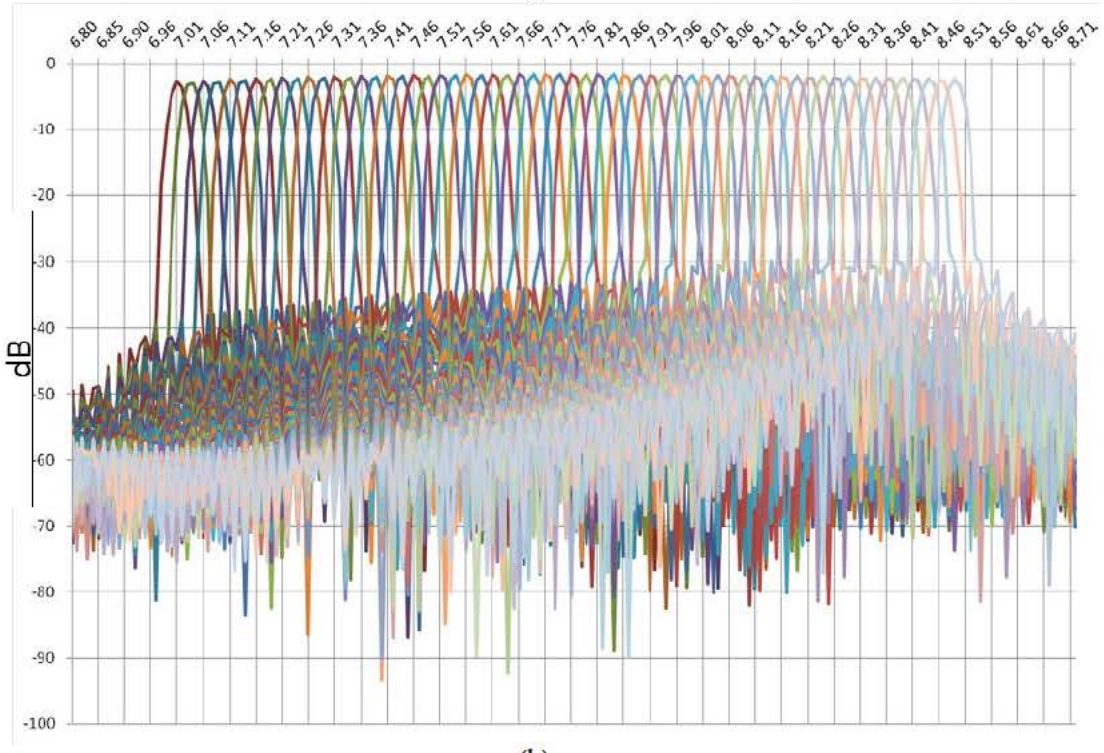

(b)

Figure 3.16. Simulation results showing the combined input channel spectrum of a dual 15-to-1 Echelle grating based (de)multiplexer for TE (a) and TM (b) fundamental modes for the 7.0-8.5 µm wavelength range

The results show that design efforts concerning combining stages after the multiplexer subdesigns allow for a further increasing of interchannel crosstalk levels without affecting the individual channels. This improves the spectrum appearance of the combined channels by reducing the difference between the maximum and minimum channel profiles. Simulations of dual Echelle grating BBs into a single output, as shown in Figure 3.16, show a high reduction in channel width and confirm the interchannel crossing level theoretical behavior in a range between 1.5 and 2.5 dB for both fundamental mode TE and TM polarizations.

In the light of the simulation results, this technique regarding the division of an Echelle grating multiplexer BB into two different subdesigns is proven feasible in order to address the limiting factors reducing the device capabilities and introducing losses.

3.3.3 - Rowland grating design for the 7.0 – 10.0 μm wavelength range

A second wavelength range, consisting in the wavelengths between 7 and 10 μm in the mid infrared, was defined as an objective for the III-V Lab platform. The objective is the same as for the 7-8.5 μm range, consisting in the design of a single output widely tunable MIR source.

In order to address this proposal, the same steps were followed for the design and simulation of this design. The basic input parameters for the design of an Echelle grating multiplexer building block are shown in Table 3.6 in direct analogy with the 7-8.5 μm multiplexer design, as discussed in section 0.

Building block name	**Echelle grating multiplexer**
Input parameters	Identifier
Number of input waveguides	30
Number of output waveguides	1
Waveguide width	6 μm
Cladding width	1 μm
Initial wavelength	7.0 μm
Final wavelength	10.0 μm
Incidence angle of the input waveguides	0º
Diffraction order	1

Table 3.6. Input parameters for the 7.0-10.0 μm Echelle grating based (de) multiplexer

The simulation results, as shown in Figure 3.17, show the channel crosstalk for both TE and TM modes in the studied wavelength range. In the case of the TE fundamental

mode, channel crossing ranges from 14 to 20 dB and between 4.5 and 6 dB for the TM fundamental mode. Such ranges directly affect the transmission capabilities of the multiple light sources; making the reduction of such channel crossing levels a priority.

These channel crossing levels are smaller in comparison with the 7-8.5 μm single Echelle multiplexer design, which signals the channel width as a parameter value to increase or reduce the channel crosstalk levels in adjacent channels. The simulated spectrum is shown in Figure 3.17 for the fundamental TE and TM propagating modes.

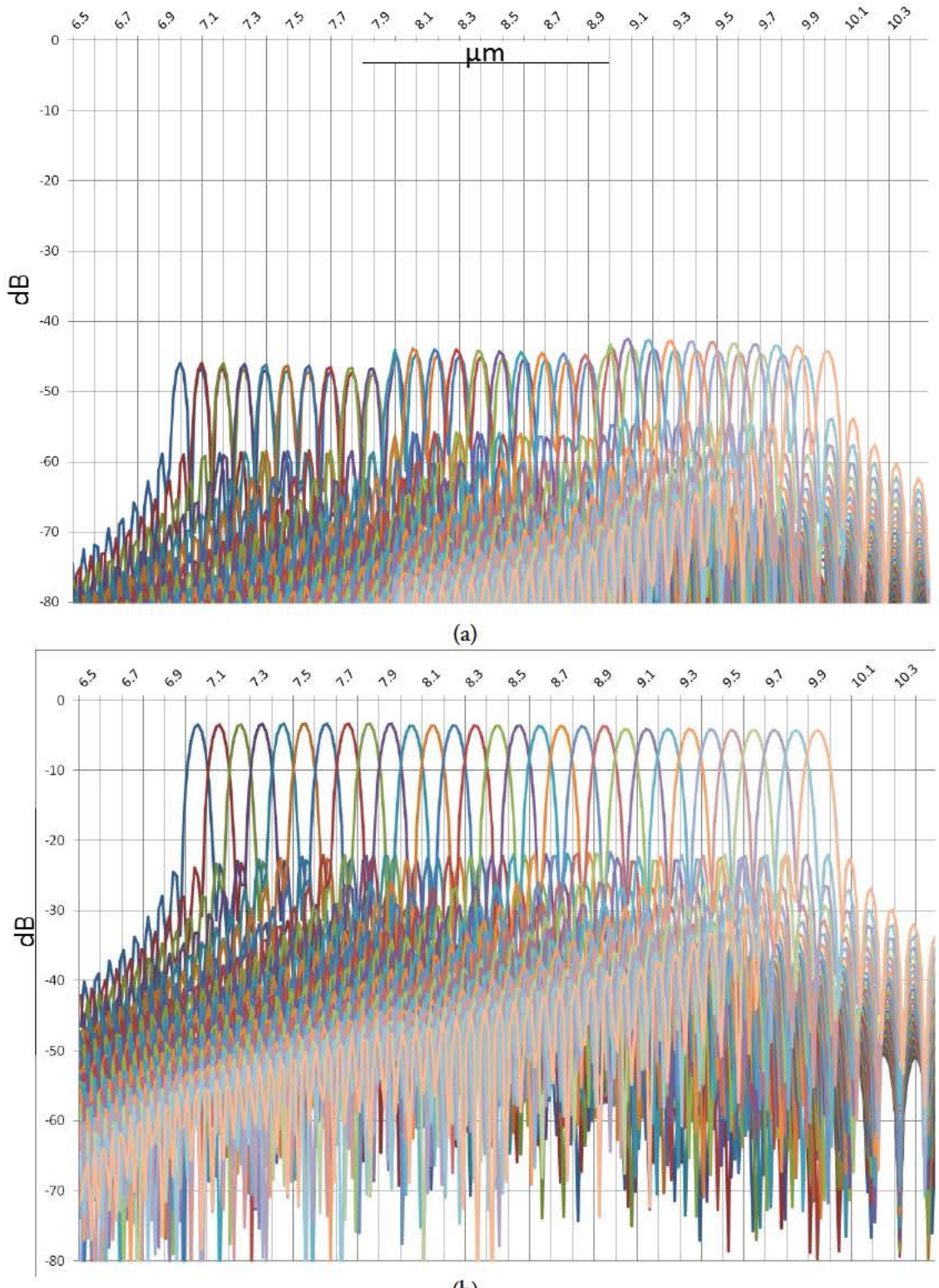

Figure 3.17. Simulation results showing individual input channels of a 30-to-1 Echelle grating based (de)multiplexer for TE (a) and TM (b) fundamental modes for the 7.00-10.00 µm wavelength range

Given the simulation results, a dual Echelle grating multiplexer building block structure is also proposed in order to reduce footprint area of the overall design, as well as to prove the scalability of the multiple Echelle grating BB for different wavelength ranges. The input and the resulting output parameters are shown in Table 3.7.

Building block name	**Echelle (de)mux A**	**Echelle (de)mux B**
Input parameters	Identifier	Identifier
Number of input waveguides	15	15
Number of output waveguides	5	5
Waveguide width	6 μm	
Cladding width	1 μm	
Initial wavelength	7.0 μm	
Final wavelength	10.0 μm	
Central wavelength of the initial waveguide	7.00 μm	7.1 μm
Central wavelength of the final waveguide	10.0 μm	10.1 μm
Incidence angle of the input waveguides	0°	0°
Diffraction order	1	
Output parameters	Identifier	Identifier
Rowland radius	400 μm	400 μm
Device footprint area	502654.82 μm^2	502654.82 μm^2
Incidence angle of the output waveguides	53.90666º	54.62575º
Central wavelength	8.50 μm	8.55 μm
Channel width	0.2 μm	0.2 μm
Waveguide spacing	1 μm	1μm
Channel crossing level	16-20 dB for TE / 6-12 dB for TM	16-20 dB for TE / 6-12 dB for TM
Grating length	750 μm	750 μm

Table 3.7. Design and output parameters for the 7-10.0 μm Echelle grating based (de) multiplexer

Output parameters show a major decreasing in the Rowland radius and the footprint area; this is a confirmation of the impact of the wavelength range of the device and the wavelength width of the waveguide channel as the most influential parameters in defining the total area of the design. This is because the larger the parameter values, the diffraction angle between the initial and final wavelengths of the range differ the most; allowing for the reduction of the Rowland radius for a closer waveguide spacing.

Figure 3.18 and Figure 3.19 show the simulated spectrum of both subdesigns. The simulations show a variation in the channel crossing in comparison with the obtained for the single Echelle grating BB. These values are 16-20 dB for the TE mode and 6-12 dB for the TM.

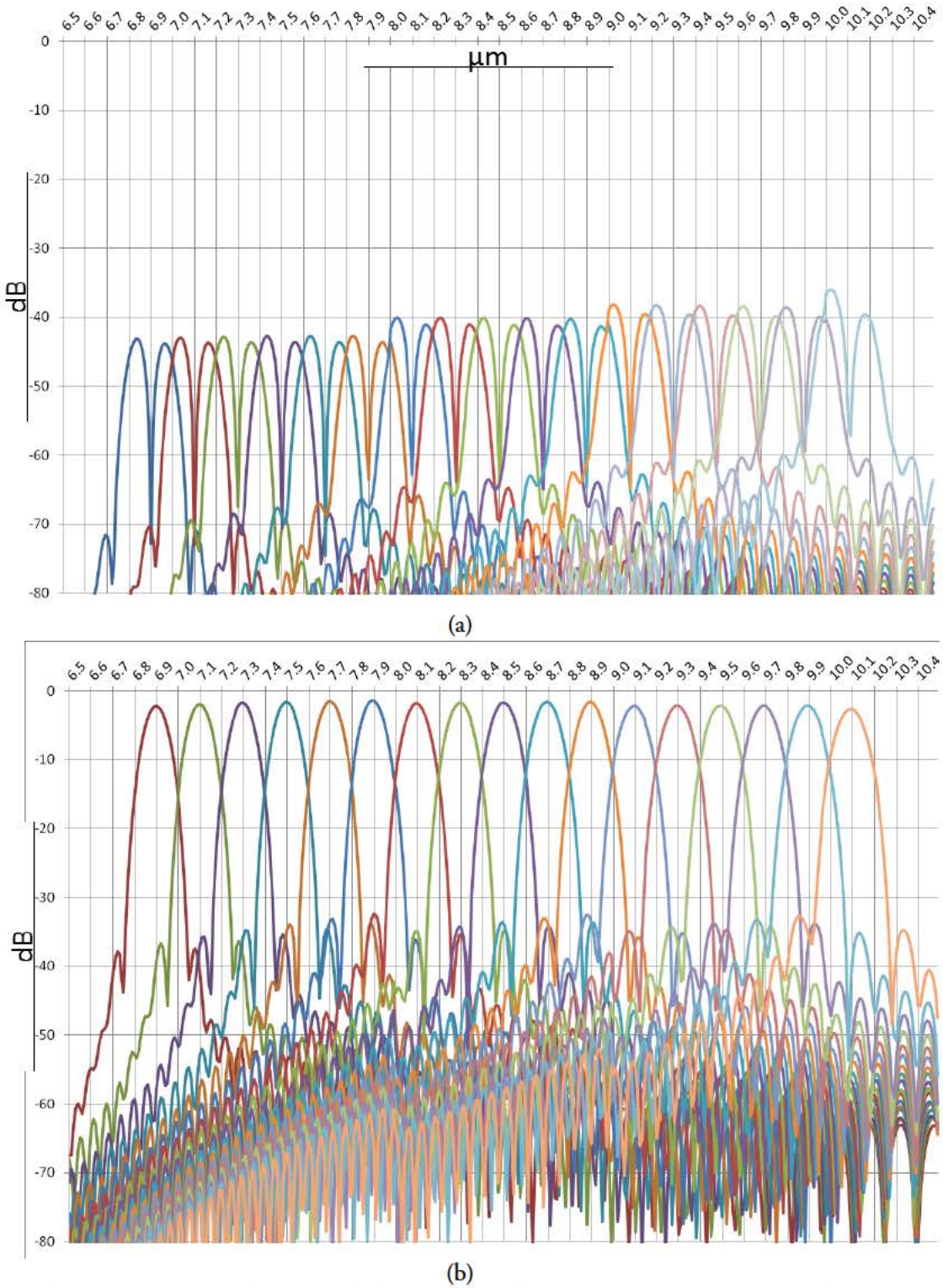

(a)

(b)

Figure 3.18. Simulation results showing individual input channels of a dual design 15-to-1 Echelle grating based (de)multiplexer for TE (a) and TM (b) fundamental modes for the 7.00-10.0 μm wavelength range

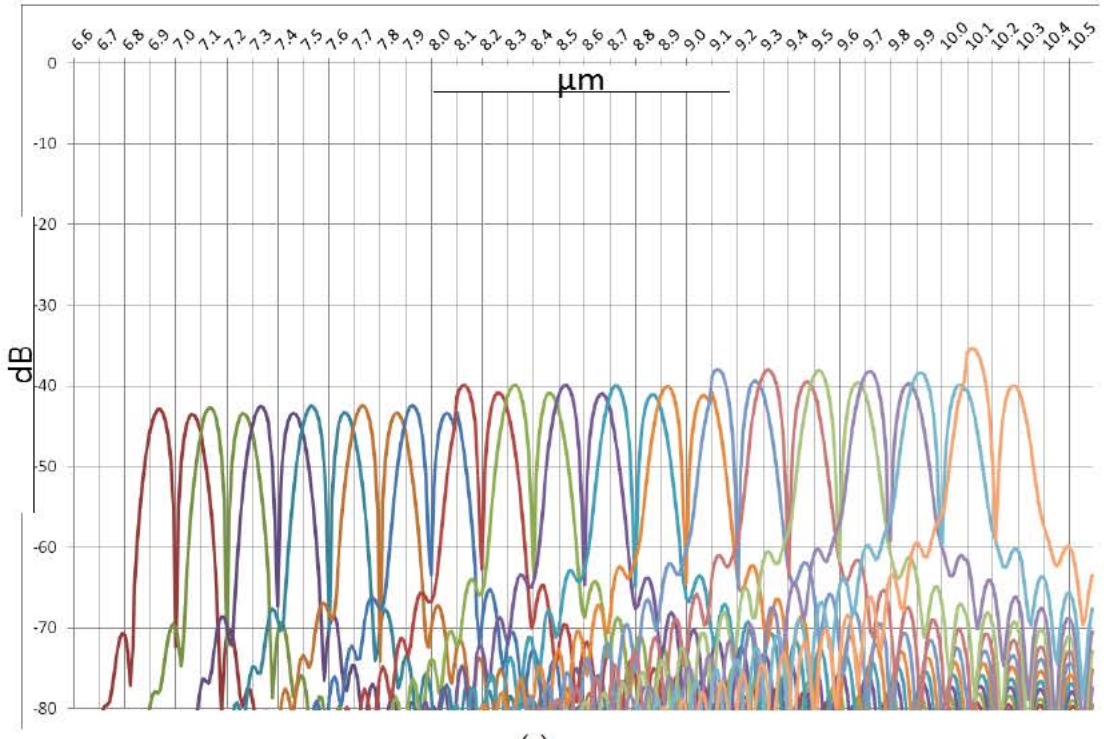

(a)

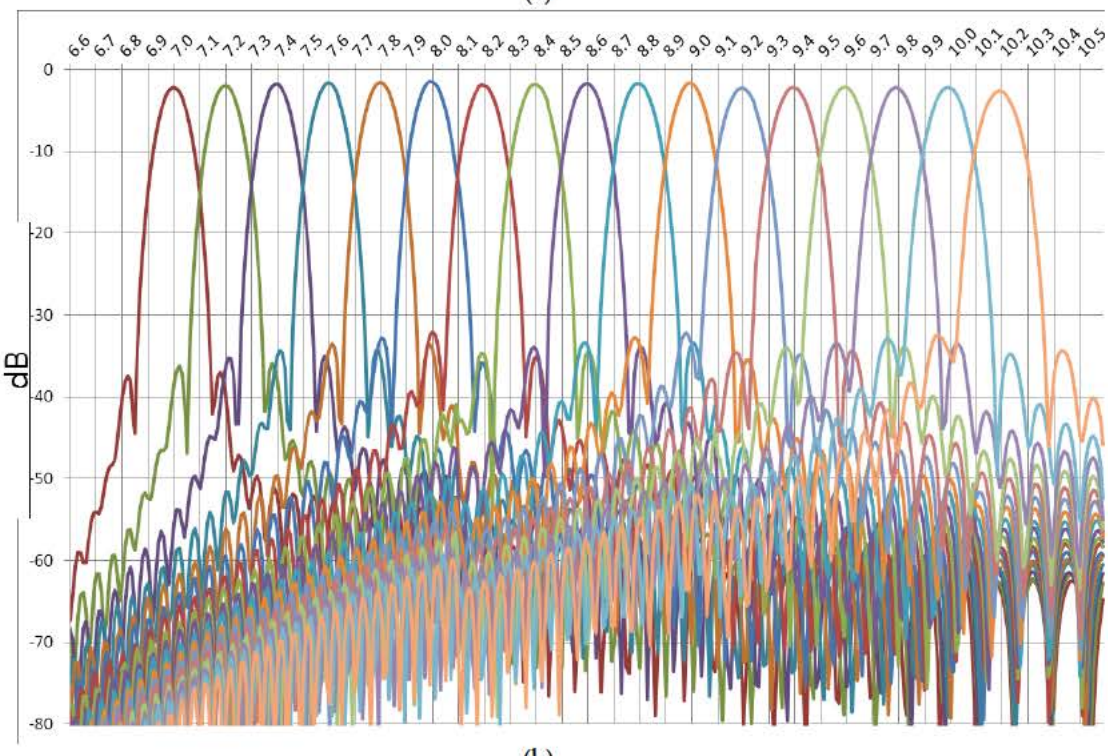

(b)

Figure 3.19.Simulation results showing individual input channels of a dual design 15-to-1 Echelle grating based (de)multiplexer for TE (a) and TM (b) fundamental modes for the 7.1-10.1 µm wavelength range

The combination of the dual Echelle grating Multiplexer BB into a single output conformed by a Y-junction 2-to-1 multiplexer was also studied in order to measure the improvement in maximum and minimum channel profiles. Results confirm that combining stages after the multiplexer subdesigns allow for a further increasing of interchannel crosstalk levels without affecting the individual channels; improving the spectrum appearance of the combined channels by reducing the difference between the maximum and minimum channel profiles.

Simulations of dual Echelle grating BBs into a single output for the 7-10 range are shown in Figure 3.20. The figure shows a high reduction in channel width and confirms the interchannel crosstalk theoretical behavior.

One concluding the design stage, a fabrication procedure is done in order to confirm the aforementioned BBs and structures. Results of the fabrication procedures are discussed in detail in following chapters including the characterization results of some of the discussed designs.

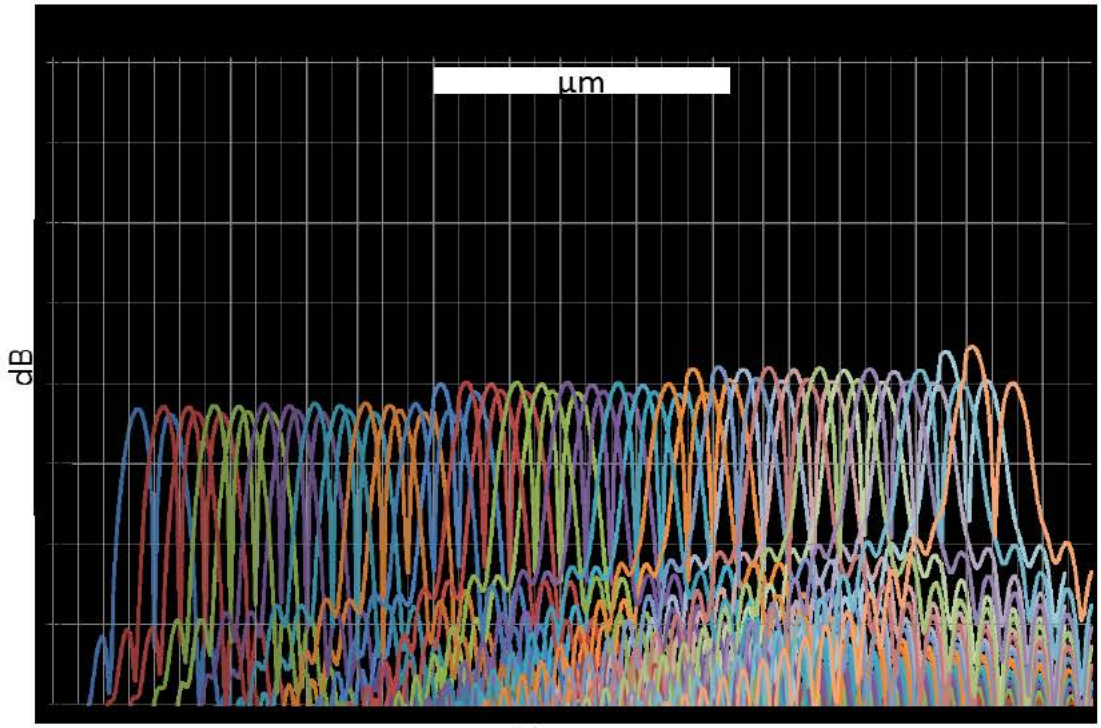

(a)

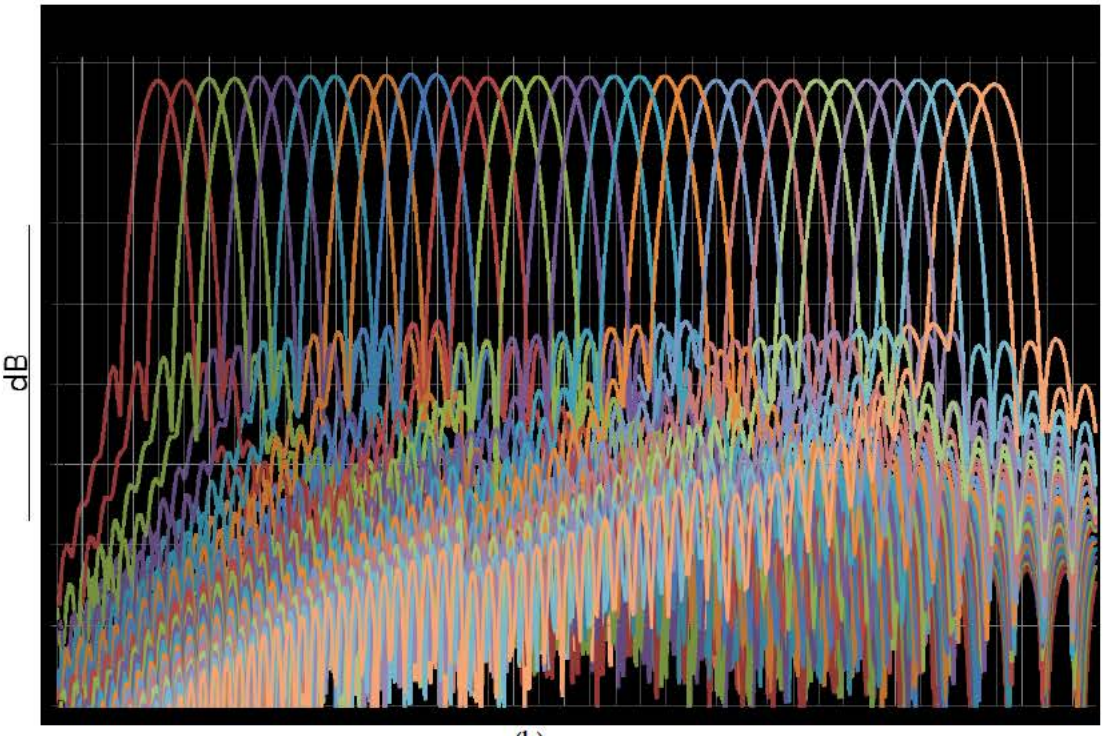

(b)

Figure 3.20. Simulation results showing the combined input channel spectrum of a dual 15-to-1 Echelle grating based (de)multiplexer for TE (a) and TM (b) fundamental modes for the 7.0-8.5 µm wavelength range

3.4 - Discussion and remarks

In this chapter, a MIR multiplexer design was done following two different approaches in the framework of project MIRIFISENS using the III-V Lab epilayer structure. Both designs were based on the waveguiding analysis and bent waveguide parameterization results for such epitaxy, as detailed in Chapter II.

The simulation results shown in this chapter present a proof of concept for the multiplexer stage in the fabrication of monolithically integrated widely tunable MIR sources in two different wavelength ranges:

- 7.00 – 8.50 μm (1176.5 – 1428 cm^{-1})
- 7.00 to 10.00 μm (1000 - 1428 cm^{-1})

Both of those ranges are to be covered with 30 input channels.

The basis of this work is based on the previously detailed S-bend Building Blocks, which combined design into Y-junction based 2-to-1 (de)multiplexers was the starting point for the first of the two multiplexer approaches, however, this multiplexing approach is not wavelength specific.

First, a Y-junction based 2-to-1 scalable multiplexer BB was defined and parameterized. This BB based construction scheme provided a scalable solution consisting in various multiplexer levels sequentially connected and capable of multiplexing “k” number of light

sources, monolithically integrated or not. The number of sequences, or multiplexing levels, for this design was described by n = log2(k).

However, power limitations were observed in the simulation results for individual elements of the multiplexer sequence, as FDTD based simulations showed an estimated loss per multiplexer level between 1.87 and 3 dB. As the objective of this design is to multiplex 30 DFB-QCL sources in an array configuration, the resulting design is needed to have an n=5 multiplexing levels, corresponding to a level of losses between 9.35 and 15.00 dB.

The second design approach was the development of an Echelle grating based multiplexer BB. These structures are based on diffraction gratings and a geometrical placement of the input and output waveguides. Each design is wavelength dependant.

The first step was a FMM simulation over the cross section of the input and output waveguides of the device, after that and given the large number of reflections to consider in the model, an FDTD simulation was done. The results allowed for the visualization of the output spectrum, which shows the simulated behavior of each input waveguide, corresponding to each of the input channels of the multiplexer.

In order to improve the crosstalk characteristic and level of insertion losses, a variation of the Echelle grating multiplexer was proposed in the form of a dual Echelle grating multiplexer (two subdesigns). Each of those subdesigns inherited the design characteristics from the original single Echelle model. However, in order to improve the aforementioned parameter results, the wavelength spacing between adjacent input channels for each subdesign was doubled, allowing for a smaller device area and therefore a reduction of the insertion losses.

A comparison between the major simulation results for both the single and double Echelle grating multiplexer solutions is summarized in the next table:

Wavelength range: 7.0-8.5 μm	**Single Echelle multiplexer**	**Dual Echelle multiplexer (for each subdesign)**	**Dual Echelle multiplexer (complete design)**
Input wavelength spacing (μm)	0.05	0.1	0.05
Insertion losses (dB)	TE: 42 – 46.5 TM: 2.5 – 3.2	TE: 41 - 46 TM:2.5 – 3.5	TE: 41 - 46 TM:2.5 – 3.5
Crossing level (dB)	TE: 14 - 16 TM: 6 -9	TE: 14 - 16 TM: 6 - 9	TE: 1.5 – 2.5 TM: 1.5 – 2.5
Wavelength range: 7.0-10.0 μm	**Single Echelle multiplexer**	**Dual Echelle multiplexer (for each subdesign)**	**Dual Echelle multiplexer (complete design)**
Input wavelength spacing (μm)	0.1	0.2	0.1
Insertion losses (dB)	TE: 42 – 46.5 TM: 4 - 5	TE: 36.5 – 43.5 TM:2.5 – 3.5	TE: 36.5 – 43.5 TM:2.5 – 3.5
Crossing level (dB)	TE: 14 - 20 TM: 4.5 - 6	TE: 14 - 20 TM: 4.5 - 6	TE: 1.5 – 2.5 TM: 1.5 – 2.5

Table 3.8. Summarization of the simulation results for the Echelle grating based multiplexer approach

The total losses are not presented given the necessity of adding the connecting input and output waveguides into the model. However, their magnitude is similar for both single and dual schemes.

As we can observe, the best results for both insertion losses and crosstalk level are achieved for a dual Echelle grating multiplexer for both the insertion losses and crosstalk level.

Given these results, a fabrication procedure was done and the characterization efforts for numerous BBs for straight, bent waveguides and multiplexer structures are detailed in Chapter IV.

3.5 - References

[1] M. C. Phillips and N. Hô, “Infrared hyperspectral imaging using a broadly tunable external cavity quantum cascade laser and microbolometer focal plane array,” Opt. Express, vol. 16, 2008, pp. 1836–1845.

[2] Shorter, J.H.; Nelson, D.D.; McManus, J.B.; Zahniser, M.S.; Milton, D.K.; "Multicomponent Breath Analysis With Infrared Absorption Using Room-Temperature Quantum Cascade Lasers,"Sensors Journal, IEEE , vol.10, no.1, pp.76,84, Jan. 2010.

[3] Kim, Seong-Soo; Young, C.; Vidakovic, B.; Gabram-Mendola, S.; Bayer, C.W.; Mizaikoff, B.; "Potential and Challenges for Mid-Infrared Sensors in Breath Diagnostics," Sensors Journal, IEEE , vol.10, no.1, pp.145,158, Jan. 2010.

[4] Feng X.; Caneau, C.; LeBlanc, H.P.; Visovsky, N.J.; Coleman, S.; Hughes, L.C.; Chung-en Zah, "Room Temperature CW Operation of Mid-IR Distributed Feedback Quantum Cascade Lasers for O, and NO Gas Sensing," Selected Topics in Quantum Electronics, IEEE Journal of , vol.18, no.5, pp.1605,1612, Sept.-Oct. 2012

[5] Frish, M.B.; Wainner, R.T.; Laderer, M.C.; Green, B.D.; Allen, M.G.; "Standoff and Miniature Chemical Vapor Detectors Based on Tunable Diode Laser Absorption Spectroscopy," Sensors Journal, IEEE , vol.10, no.3, pp.639,646, March 2010.

[6] Jouy, P.; Faist, J.; et al; "Multi-wavelength QCL based MIR spectroscopy for fluids and gases," CLEO, 2013, vol.; no.; pp.1,2, 9-14 June 2013.

[7] Fuchs, et al; "Detection of hazardous substances using broadband-tuneable quantum cascade laser based mid-infrared spectroscopy," CLEO EUROPE/IQEC, 2013, vol.; no.; pp.1,1, 12-16 May 2013

[8] Alpes Lasers QCL FAQ List (http://www.alpeslasers.ch/alfaq.pdf)

[9] W. Zeller *, L. Naehle, P. Fuchs, F. Gerschuetz, L. Hildebrandt and J. Koeth; "DFB Lasers Between 760 nm and 16 μm for Sensing Applications"; Laser Spectroscopy and Sensing (2010)

[10] Faist, J.; Tredicucci, A.; Capasso, F.; Sirtori, Carlo; Sivco, Deborah L.; Baillargeon, James N.; Hutchinson, A.L.; Cho, Alfred Y., "High-power continuous-wave quantum cascade lasers," in Quantum Electronics, IEEE Journal of , vol.34, no.2, pp.336-343, Feb 1998

[11] Lee, B. G.; et al; "Broadband Distributed-Feedback Quantum Cascade Laser Array Operating From 8.0 to 9.8 \mu m" Photonics Technology Letters, IEEE , vol.21, no.13, pp.914,916, July1, (2009)

[12] Carras, M.; et al; "Advances toward monolithic broadly-tunable QCL sources," Proc. SPIE 8993 (2014)

[13] Maisons, G.; Carras, M.; et al; "Advances toward monolithic tunable source," ISLC (2014)

[14] M. Muneeb, X. Chen, P. Verheyen, G. Lepage, S. Pathak, E. Ryckeboer, A. Malik, B. Kuyken, M. Nedeljkovic, J. Van Campenhout, G. Z. Mashanovich,

and G. Roelkens, "Demonstration of silicon-on-insulator mid-infrared spectrometers operation at 3.8μm," Opt. Express 21(10), 11659-11669 (2013)

[15] R. Soref, "Mid-infrared photonics in silicon and germanium," Nat. Photonics 4(8), 495-497 (2010)

[16] A. Malik, M. Muneeb, S. Pathak, Y. Shimura, J. Van Campenhout, R. Loo, and G. Roelkens, "Germanium-on-silicon mid-infrared arrayed waveguide grating multiplexers," IEEE Photon. Technol. Lett. 25(18), 1805-1808 (2013)

[17] A. Malik, M. Muneeb, Y. Shimura, J. Van Campenhout, R. Loo and G. Roelkens, "Germanium-on-silicon planar concave grating wavelength (de)multiplexers in the mid-infrared," Appl. Phys. Lett. 103, 161119 (2013)

[18] S. Adachi, "Model dielectric constants of GaP, GaAs, GaSb, InP, InAs and InSb," Phys. Rev. B 35(14), 7454-7463 (1987)

[19] L. H. Peng, T. Broekaert, W. Y. Choi, C. Fonstad, and V. Jones, "Defect activated infrared multiphonon excitation in iron-doped semi-insulating indium phosphide," Appl. Phys. Lett. 59(5), 564-566 (1991)

[20] Lycett, R.J.; Gallagher, D.F.G.; Brulis, V.J.; "Perfect Chirped Echelle Grating Wavelength Multiplexor: Design and Optimization," Photonics Journal, IEEE , vol.5, no.2, pp.2400123,2400123, April 2013

[21] L. J. Orbe, G. Carpintero, G. Maisons, M. Carras, "QCL-based photonic integrated circuits on InP and other platforms," IPRM (2014)

[22] L. J. Orbe, C. Gordon, G. Carpintero, G. Maisons, M. Carras, "InGaAs/InP-based Echelle mirror multiplexer using dual Rowland circle

gratings for DFB QCL arrays in the mid-long infrared range," SPIE Photonics West (2014)

[23] Feng, D.; Qian, W.; Liang, H. ; Kung, C.; Fong, J.; Luff, B.J.; Asghari, M.; "Fabrication Insensitive Echelle Grating in Silicon-on-Insulator Platform," Photonics Technology Letters, IEEE , vol.23, no.5, pp.284,286, March1, 2011

[24] Lee, D.C.; Dazeng Feng; Cheng-Chih Kung; Fong, J.; Wei Qian; Xuezhe Zheng; Cunningham, J.E.; Krishnamoorthy, A.V.; Asghari, M.; "Monolithic chip-to-chip WDM optical proximity coupler utilizing echelle grating multiplexer/demultiplexer integrated with micro mirrors built on SOI platform," Photonics Society Summer Topical Meeting Series, 2010 IEEE , vol.; no.; pp.215,216, 19-21 July 2010

[25] Janz, S.; Balakrishnan, A.; Charbonneau, S.; Cheben, P.; Cloutier, M.; Dela^ge, A.; Dossou, K.; Erickson, L.; Gao, M.; Krug, P.A.; Lamontagne, B.; Packirisamy, M.; Pearson, M.; Xu, D.-X.; "Planar waveguide echelle gratings in silica-on-silicon," Photonics Technology Letters, IEEE , vol.16, no.2, pp.503,505, Feb. 2004

[26] Tolstikhin, V. I.; Densmore, A.; Logvin, Y.; Pimenov, K.; Wu, F.; LaFramboise, Sylvain, "44-channel optical power monitor based on an echelle grating demultiplexer and a waveguide photodetector array monolithically integrated on an InP substrate," Optical Fiber Communications Conference, 2003. OFC 2003 , vol.; no.; pp.PD37,P1-3 vol.3, 23-28 March 2003

[27] Sciancalepore, C.; Lycett, R.J.; Dallery, J.A.; Pauliac, S.; Hassan, K.; Harduin, J.; Duprez, H.; Weidenmueller, U.; Gallagher, D.F.G.; Menezo, S.;

Ben Bakir, B.; "Low-Crosstalk Fabrication-Insensitive Echelle Grating Demultiplexers on Silicon-on-Insulator," Photonics Technology Letters, IEEE , vol.27, no.5, pp.494,497, March1, 1 2015

[28] C. Gilles, L. J. Orbe, G. Carpintero, G. Maisons, M. Carras, "Mid-infrared wavelength multiplexer in InGaAs/InP waveguides using a Rowland circle grating," Optics Express (accepted)

[29] L. J. Orbe, G. Carpintero, C. Gilles, F. Boulila, G. Maisons, M. Carras, "Characterization of an InGaAs/InP-based Echelle Mirror Multiplexer for Widely Tunable Mid-IR Sources Based on Quantum Cascade Lasers," SPIE Photonics West (2015)

[30] L. J. Orbe, G. Carpintero, G. Maisons, C. Gilles, F. Boulila, M. Carras, "MIR Photonic Integrated Circuits for Laser Spectroscopy," MIOMD (2014)

Fabrication and Experimental Results for InGaAs/InP Passive Optical Functions and Multiplexer Structures

4.1 - Overview of the MIRIFISENS fabrication procedure

The fabrication of the samples was performed at III-V LAB, using their fabrication facilities from wafer growth on a Molecular Beam Epitaxy (MBE) to wafer processing. III-V LAB already produces DFB-QCLs, using an active epitaxial layer structure. We aim to develop a passive epitaxial layer structure that allows the monolithic integration on InP of an active DFB-QCL array and a passive multiplexer.

The multiplexer designs detailed in the previous chapters had to be validated previously to attempting a monolithic integration with the DFB-QCL array. We established the following set of steps for their development:

1.- Fabrication and processing of wafers with passive epilayer only, following the proposed designs. Passive wafers do not require the growth complex and time consuming quantum cascade epilayer.

2.- Processing the passive wafers to fabricate passive test structures and components. Two wafers including only the passive layers were fabricated and processed.

3.- Experimental measurements of the basic passive components (waveguides, bents, Y-junctions) in order to assess their performance. These are very basic components and provide the elemental building blocks on a photonic integration platform. Their validation, through the comparison of the measurements against simulation results to validate the design procedure allows us to compare the performance of these elements on the MIR

platform. The experimental results were discussed in order to feed back into epitaxial and component design.

4.- Once that the basic building blocks of the platform have been characterized, we move to the design of different multiplexer structures, mainly using echelle grating multiplexers. The tested building blocks allow us to propose different configurations to accommodate the requested number of inputs (30 and 60 emitter arrays).

4.- Processing the multiplexer structures

4.2 - Fabrication and processing of wafers for passive components

A) Test mask design

The first step was to provide a mask design with different designs to assess the design parameters of each component. We allocated a test area within one half of a two inches diameter InP wafer. The areas allocated for the test designs are shown in Figure 4.1. The process separates the Echelle grating multiplexer designs from the other BBs, as they require additional steps for their fabrication.

A general description of the design layout of the mask is provided so that the resulting mask can be adequately considered.

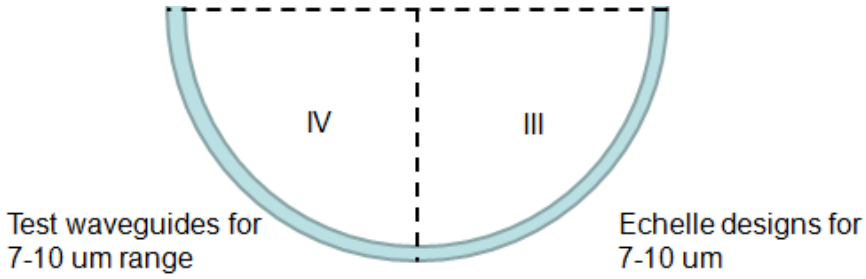

Figure 4.1. Distribution diagram of the integrated test mask design for fabrication

This division allowed for the integration of a large number of BB; the details of the basic parameter of such blocks are mentioned in the following table.

Building Block	Waveguide width (µm)	Bending radius (µm)	Wafer location
Straight waveguides	6, 7, 8, 9	-	IV
Cosine S-bend	6, 7, 8, 9	150, 170, 200	IV

Sine S-bend	6, 7, 8, 9	150, 170, 200	IV
Cosine S-bend Y-junction (de)multiplexer	6, 7, 8, 9	170	IV
Sine S-bend Y-junction (de)multiplexer	6, 7, 8, 9	170	IV
7-8.5 μm Dual Echelle grating (de) multiplexer	6 μm	170, 200	III
7-10 μm Dual Echelle grating (de) multiplexer	6 μm	170, 200	III

Table 4.1. Detail of the BBs in the integrated test mask design

Figure 4.2(a) shows the overall distribution of the designs over the test mask in order to fit the wafer space. Two details of the mask design are shown in Figure 4.2(b) and 4.2(c). The first shows the detail for the design distribution of the straight and bent waveguides and the design of both the Y-junction based and the former the dual Echelle grating multiplexer BBs.

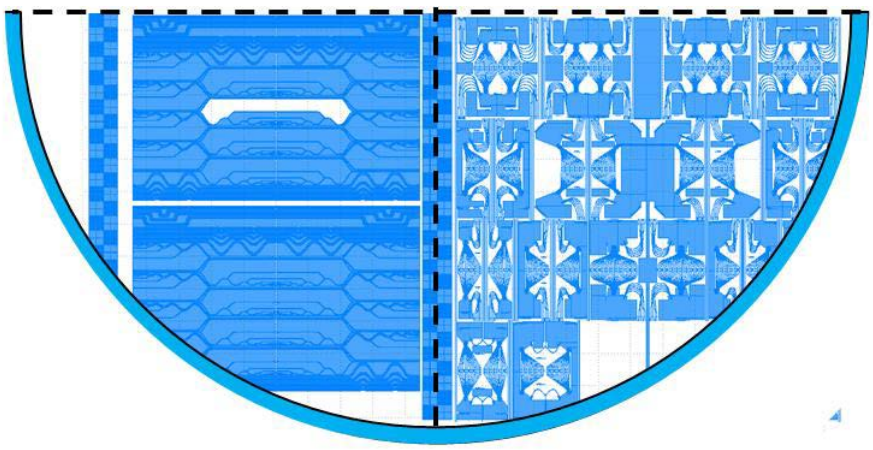

(a)

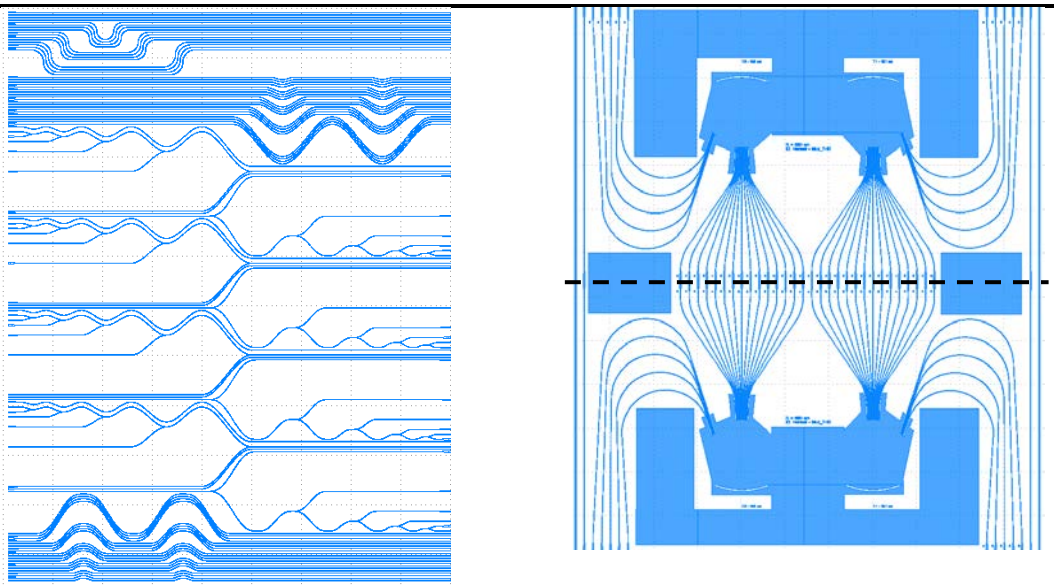

(b) (c)

Figure 4.2. (a) Mask design for the MIRIFISENS process. (b) Detail of the Mask for the straight, bent waveguides and Y-Junction multiplexers in an individual sample. (c) Detail of the Mask for a dual Echelle grating multiplexer

B) Device fabrication procedure

The initial epitaxial design for the passive components was proposed by III-V LAB, based on an Iron doped InP wafer (InP:Fe), selected over a Sulfide doped (InP:S) alternative to avoid MIR radiation resonance with the substrate free carriers[1] [2] . In the InP:Fe case, there are no free carriers and the absorption is very low[1] .

The vertical optical confinement properties of the epitaxy are ensured by the refractive index difference between the InGaAs waveguide , which presents a refraction index of 3.458 and the InP cladding and buffer layers, with a refraction index of 3.0792 (Chapter II).

The horizontal confinement, however, depends on the selected waveguiding structure according to a waveguiding analysis in order to obtain basic parameters such as etching

depth and waveguide width that are compatible with the wavelength range to propagate through them. Figure 4.3 shows the different possible variations for waveguide design as a function of the refractive index contrast, which ensures better horizontal mode confinement when this contrast value is high[3] .

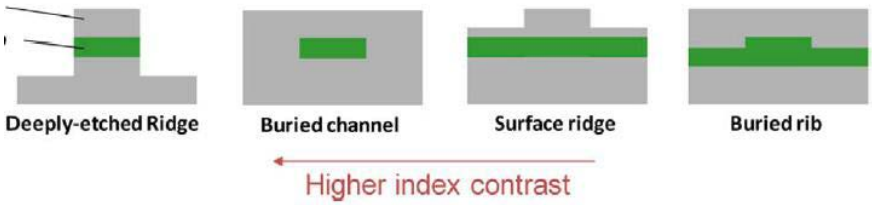

Figure 4.3. Variations for waveguide definition as a function of the index contrast

In previous chapters, a waveguiding analysis was presented for the III-V Lab epilayer. Results showed low propagation losses for etching values between 3.5 and 4.5 μm, which could have corresponded to either a deep etch or buried channel waveguide design. However, the III-V Lab platform fabrication process does not include an InP regrowth stage after the waveguide etching and therefore, a deep etch approach was selected.

The lateral confinement is ensured by air, through deep etching. The waveguide width is defined by the spacing among trenches, as shown in Figure 4.4.

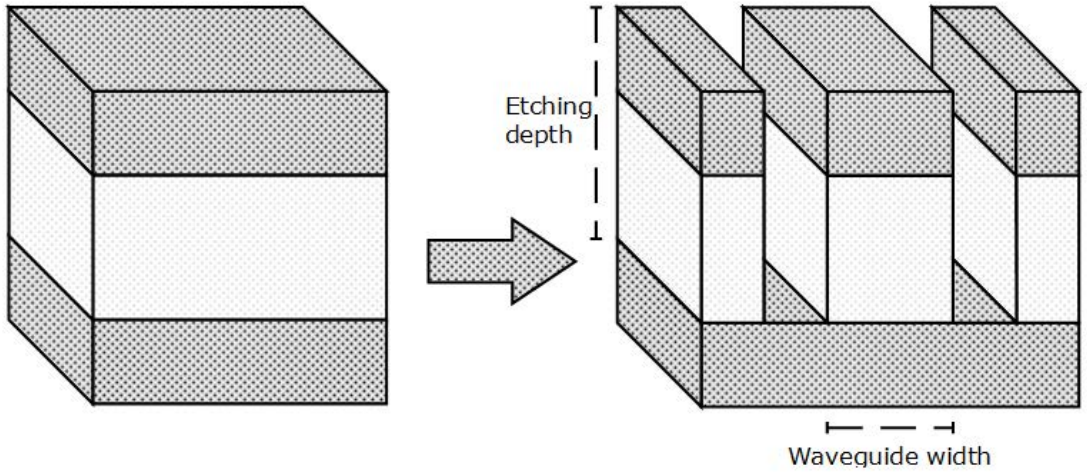

Figure 4.4. Schemes of the definition of a waveguide

The processing of the waveguide depends on the technological etching method that is selected. The selected method must enable to define the desired waveguide width as well as provide smooth sidewalls to reduce losses. If the waveguide width is not controlled or constant for all the waveguide structure, the effective index of the waveguide will vary, and modal confinement variations will occur. As some of the design details are small, size control is mandatory; therefore, any roughness in the sidewalls of the waveguides must be much smaller than the minimal pattern size in order to not to introduce undesired losses and confinement variations [4] [5] . Within the development of this thesis, two different etching processes were tested:

- **Wet chemical etching**. This process was done by etching the semiconductor material with a chemical reaction with an acidic solution (HCl based). An important drawback of this technique is that the process is isotropic, with no preferential etching direction. The resulting grooves have therefore a circular shape, creating under-etching in the ridges. The groove depth and the ridge

width cannot be individually controlled. The main advantage is that it creates smooth sidewalls (Figure 4.5(left)).

- **Dry physical etching**. This etching technique of the semiconductor material is based on physical bombardment of the material with ions emitted from plasma created between two electrodes which create an electrical field accelerating the ions. This etching procedure is anisotropic and the grooves present vertical walls, however at the expense of producing defects that cause sidewall roughness (Figure 4.5(right)).

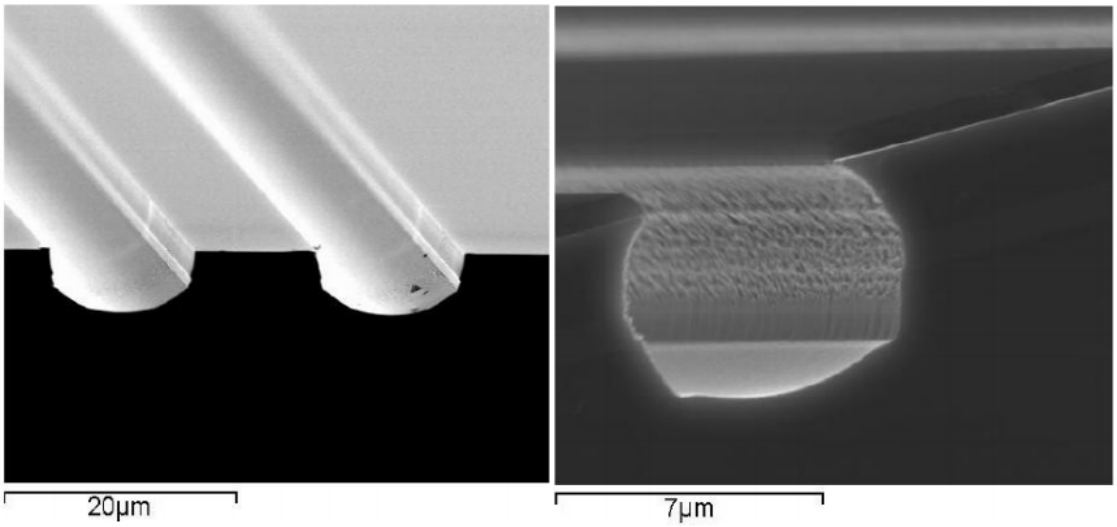

Figure 4.5. Example of etching procedures under the MIRIFISENS fabrication process, wet chemical etching (left) and dry physical etching (right).

Sample development was performed at III-V Lab for the validation of the Building Blocks described in previous chapters using the dry etching approach, as precise control to obtain vertical etched surfaces was needed. The samples were fabricated in two separate fabrication runs. The first one was focused in the optimization of the etching quality. Direct observation of the samples using a Scanning Electron Microscope (SEM) was the chosen method for the observation of the final devices. These observations revealed that

this run produced undesirable quality defects in the finished samples either of incomplete etching Figure 4.6(a), bad quality of the vertical etching (Figure 4.6 b and d) and missing transfer of the designs into the wafers (Figure 4.6 c) due to imperfections in the chromium mask or in the photoresist.

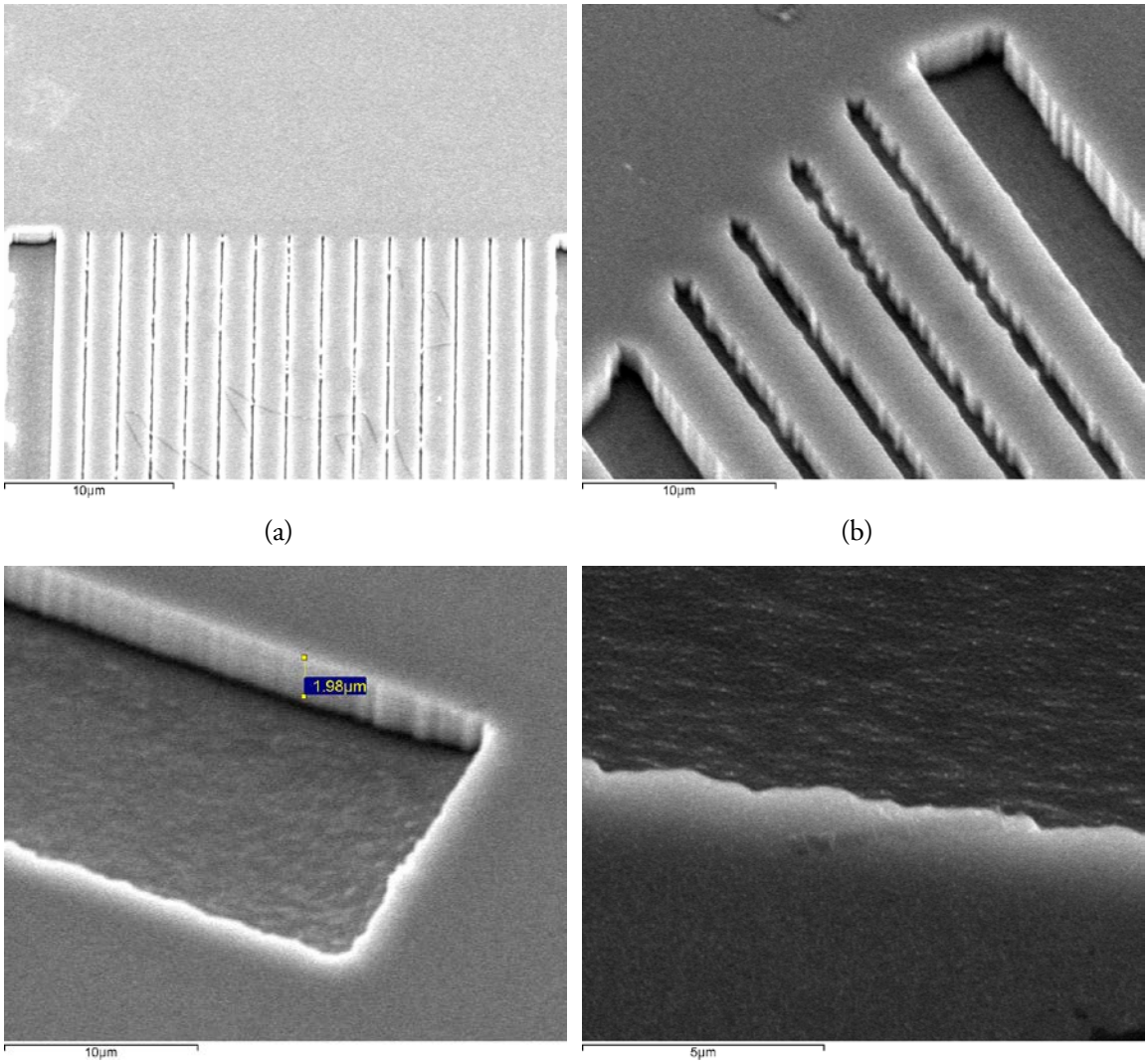

(a) (b)

(c) (d)

Figure 4.6. Fabrication errors in samples. Chromium mask defects (top) and definition errors due to poor optimization of the dry etching procedure (bottom)

A second fabrication run was necessary, which used the same mask design. In this run, careful optimization of the fabrication steps resulted in a good waveguide profile with

rectangular shape of the grooves. Sidewall roughness is still present but other defects such as incomplete etching and transfer irregularities had been removed. Figure 4.7 shows the resulting quality of this improved fabrication procedure.

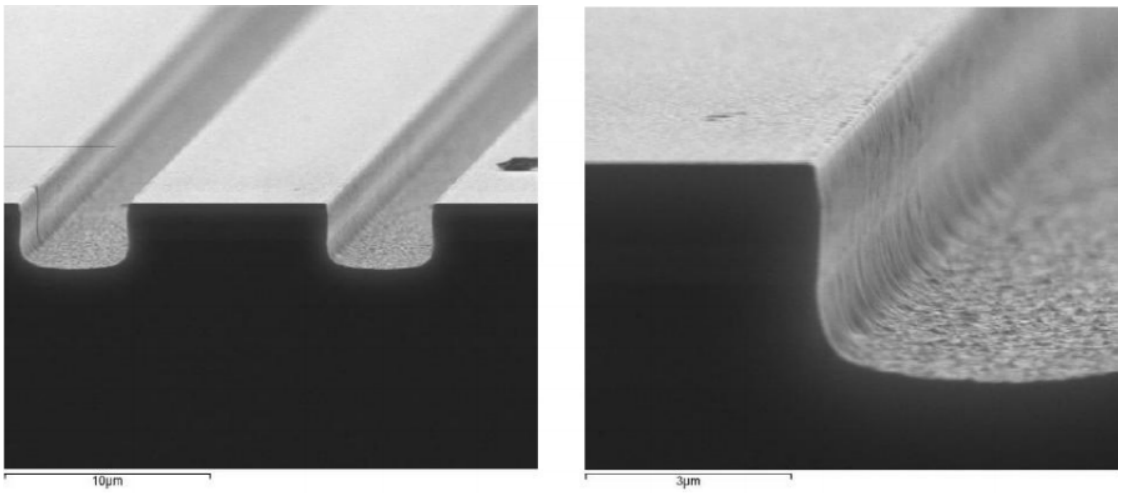

Figure 4.7. SEM pictures of straight waveguides realized with the optimized fabrication process

4.3 - Experimental measurements of the basic passive components

4.3.1 - Experimental setup

The characterization process was performed at III-V MIR Laboratory by injection of MIR light directly into the samples with the use of lenses, which provided a beam size smaller than the waveguide width (6 μm) at a focus length of about 500 μm. A pulsed current driver controlling a number of DFB-QCLs working at different wavelengths covering the 7-10 μm wavelength range was used for straight and bent waveguides, as well as the Y-Junction multiplexer optical functions.

The basic scheme of the optical bench used to characterize the samples is shown at Figure 4.8(a). The bench distribution is shown in Figure 4.8(b) and a close-up of a sample placing between two lenses is shown at Figure 4.8(c)

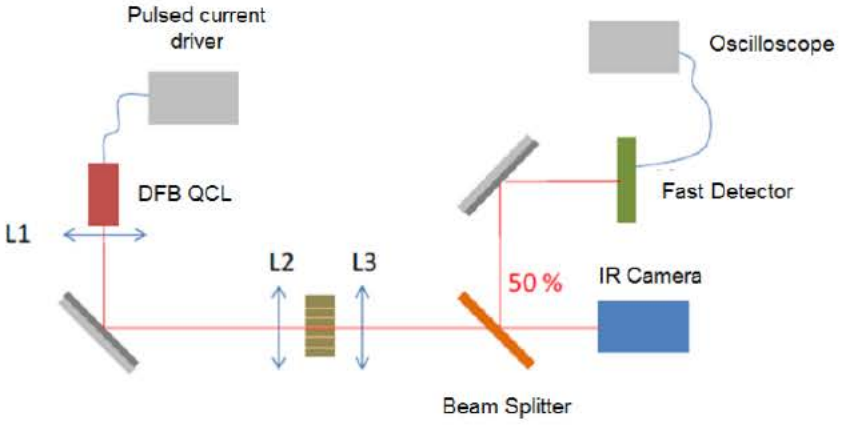

(a)

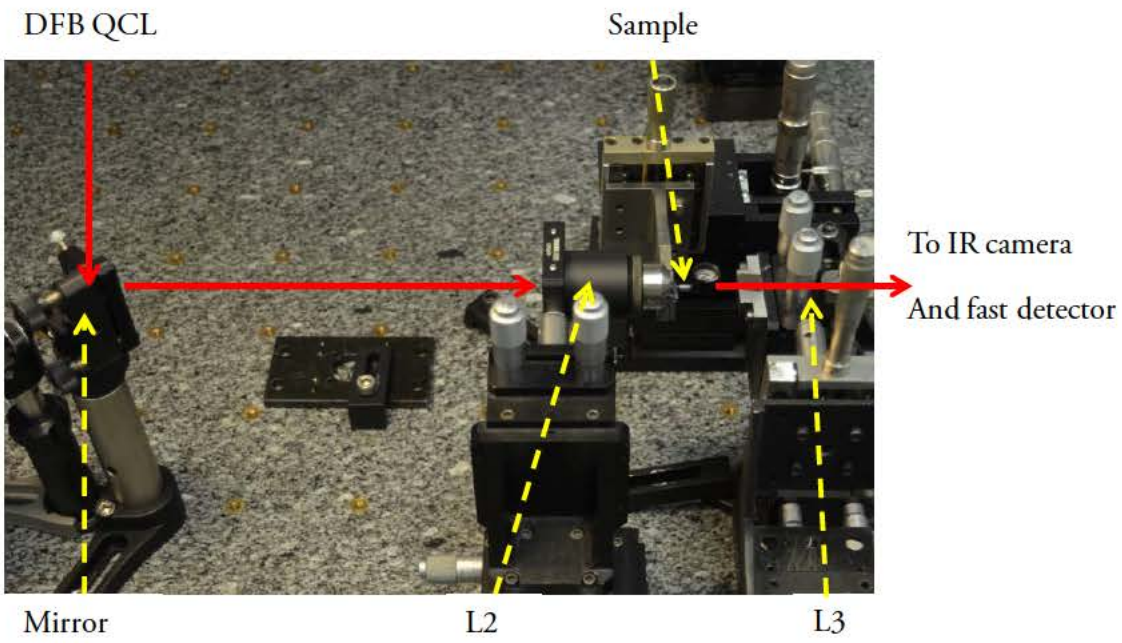

(b)

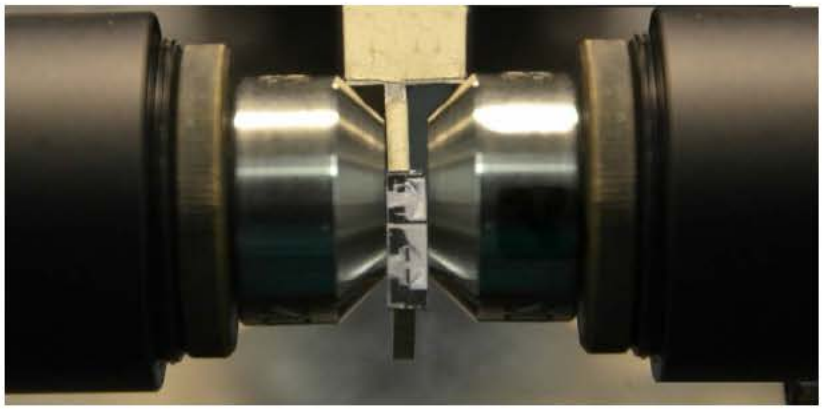

(c)

Figure 4.8. Scheme of the optical bench used to measure the losses into the waveguides; the sample is placed between L2 and L3 (a). Bench distribution of the workspace (b). Close-up of a sample placing between two lenses for light injection and gathering (c)

The samples were placed into a five-axis precision positioner, allowing for fine alignment and placement to maximize the injection of light. Output light in the exiting side of the samples was collected by other lenses and guided to a fast detector by a series of mirrors. Alignment and verification of the light injection into the samples was done by

using an IR camera for direct observation of the waveguides (Figure 4.9). The light is then captured and observed for later processing into a digital oscilloscope.

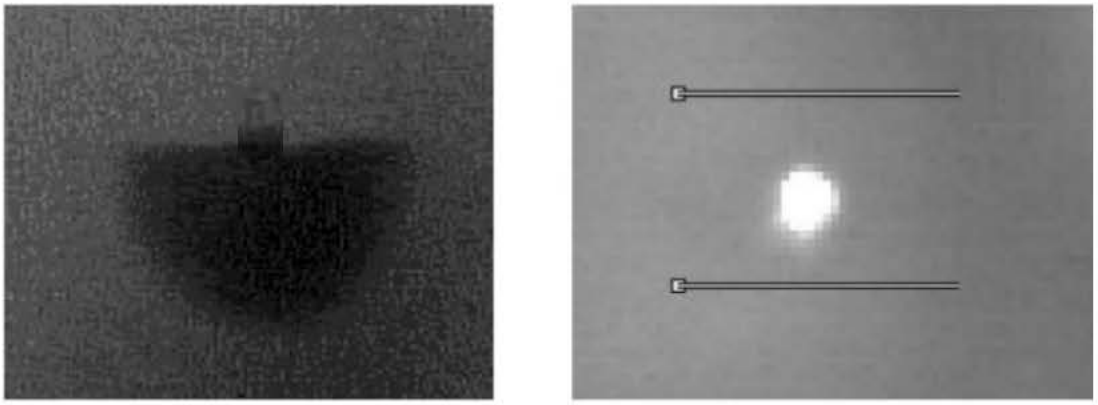

Figure 4.9. QWIP camera pictures: the sample (left) and the output light from a waveguide (right)

A variation of this scheme was introduced for the spectral characterization of the Echelle grating multiplexers (Figure 4.18). This variation introduced the use of an optic fiber to collect the light from the samples and to guide it into a Fourier Transform InfraRed (FTIR) spectroscope and a tunable light source in order to do channel width measurements.

These variations are resumed in the following Table 4.2 as a function of the characterization procedure for different samples, where the instrumental details involved in the characterization are also introduced regarding the type of BB.

Instrument	Straight, S-bend waveguides	Y-junction based (de)multiplexers	Echelle grating multiplexers
Agilent 8114A Pulse Generator	X	X	X
Newport 350B Laser thermoelectric temperature controller	X	X	X
Cascade Technologies 4-laser PW driver			X
IAF EC-QCL 7.3-8.6 µm tunable source			X
Phoenix QWIP 9803 IR camera	X	X	X
Vigo Systems Fast detector module VPAC-1000F	X		
Tektronix TDS 2014B digital oscilloscope	X		
Bruker Vertex 80 FTIR interferometer			X

Table 4.2. Configuration of the characterization bench as a function of the kind of produced samples

4.3.2 - Characterization of straight and bent waveguides

The first step in the characterization effort was to measure the propagation losses in straight and bent waveguides, as they are the most basic components to study in any platform. Their waveguiding analysis and simulation results allowed for the identification of the three major design parameters (etching depth, waveguide width and minimum bending radius) which are used as base for more complex designs. For that reason, the fabrication of these waveguides as a proof of concept was necessary.

These components are enlisted in Table 4.1, which provides a list of the fabricated components (BBs) and their design parameters. Figure 4.10 provides a view of the distribution and the mask inset for the BBs in a single sample.

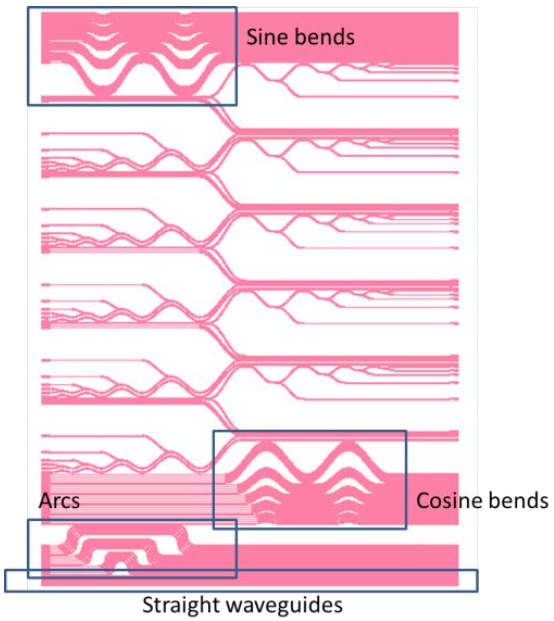

Figure 4.10. Inset of the design mask depicting the structure layout of the sample containing the straight and bent waveguides and the Y-junction based multiplexers

The characterization process began with the injection of two fixed wavelengths, at 7.4μm and at 8.7 μm using two different single mode DFB-QCLs. The losses were evaluated by measuring the transmission contrast of the Fabry-Perot fringes inside the cavity formed by the opposite cleaved facets of individual waveguides along the sample, following the technique described in [6] and [7] . This technique requires the use of a reference measurement using a cavity of a predefined length; this was obtained from a one inch mirrored cavity with an accuracy of +/- 3%. The facet reflectivity is estimated from the measurements in samples with different lengths.

Figure 4.11 shows the experimental propagation loss as a function of the waveguide width, which range from 2.1 to 3.4 dB/cm at 7.4 μm wavelength and 3.3 to 4.1 dB/cm at 8.7 μm wavelength. A decreasing trend is observed in this set of measurements, corresponding with an expected decrease in losses when the waveguide width increases.

.

Figure 4.11.Propagation losses for various ridge waveguides for a λ = 7.4 μm and a λ = 8.7 μm DFB QCL

The measurement at a wavelength of 8.7 μm shows additional losses due to the decreasing mode field overlap with the ridge walls, suggesting that scattering due to the roughness is a major source of propagation loss in our waveguides. It was not possible to obtain valid data for waveguide widths of 6 and 7 μm when injecting light at 8.7 μm due to the high insertion losses of the waveguides.

The analysis of cosine and sine bents aimed to validate the minimum bending radius and minimize bend losses, as simulations show the bending radius as a major source of loss.

Experimental attenuation losses per S-Bend were measured using the same technique as the straight waveguides for four different test samples. The results are presented as a function of the multiplexer level n, as discussed in Chapter III.

A depiction of the offset comparison between different values of the multiplexer level **n** is shown in Figure 4.12. In this figure, each value of n is correspondent to an offset level, as described in Figure 3.5 and different values of waveguide width (6, 7, 8 and 9 μm) are presented for each value of **n**.

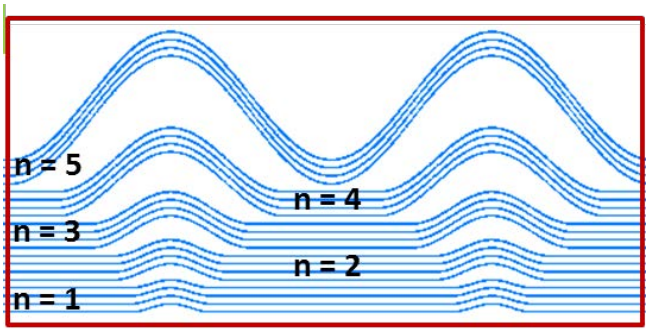

Figure 4.12. Diagram of the S-bend test structure grouped by multiplexer level n

The result of such attenuation measurements are shown individually for both Sine and Cosine S-bend functions for all the possible values of the multiplexer level **n** value at Table 4.3; these results show the attenuation loss for the entire segment, comprised by four S-bend segments and a straight waveguide. Given some fabrication defects, not all the samples were available for measurement. In the figure, each kind of marker represents an individual sample, for a total of four.

Mux level n	Cosine bends + Straight segment	Sine bends + Straight segment
1	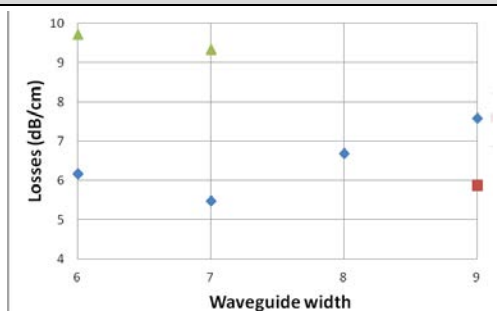	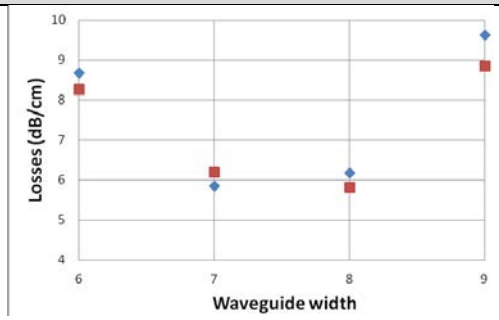
2	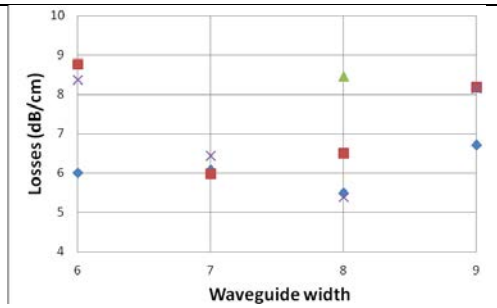	No data available
3	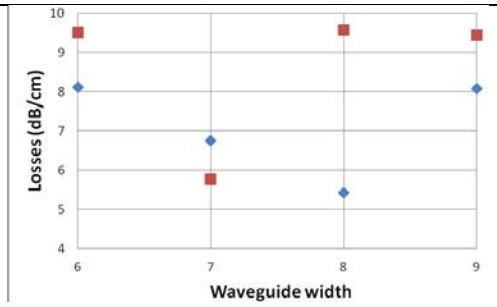	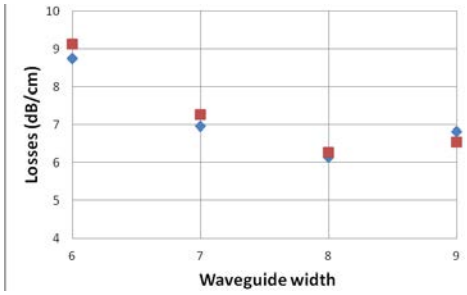
4	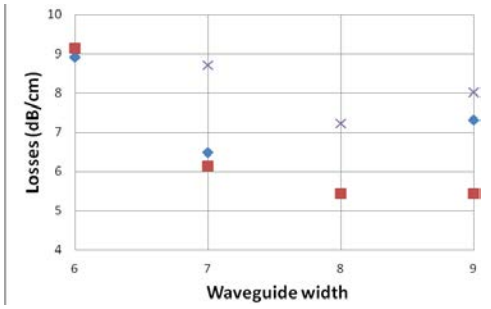	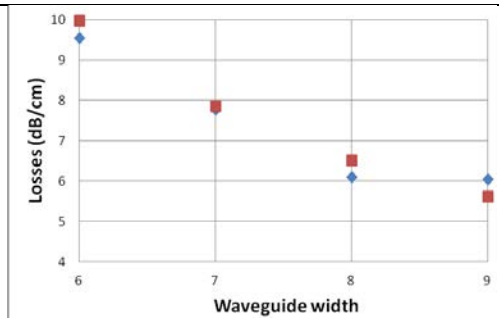
5	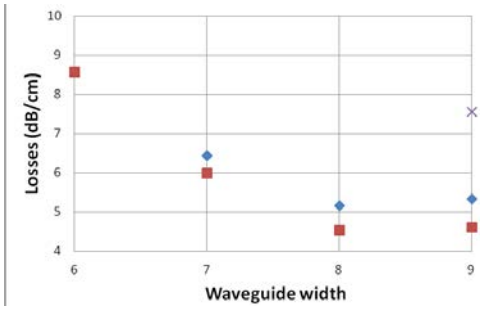	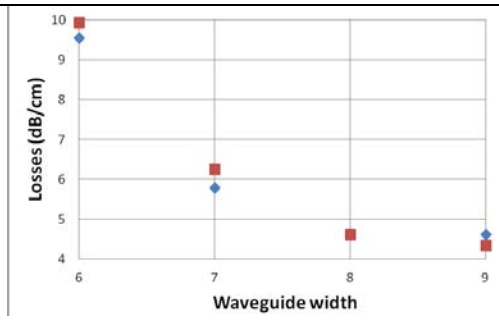

Table 4.3. Experimental measurements of the Bend+Straight section waveguide schemes

From this table, the attenuation per bend is extracted for a more clear characterization.

Table 4.4 shows the results for the individual S-bend losses for the Cosine function model. The results are divided as a function of the waveguide width in order to show the variations in magnitude for the different multiplexer levels and are shown in a different color set matching a different fabricated sample (identifiers D1, D2, D3 and D4).

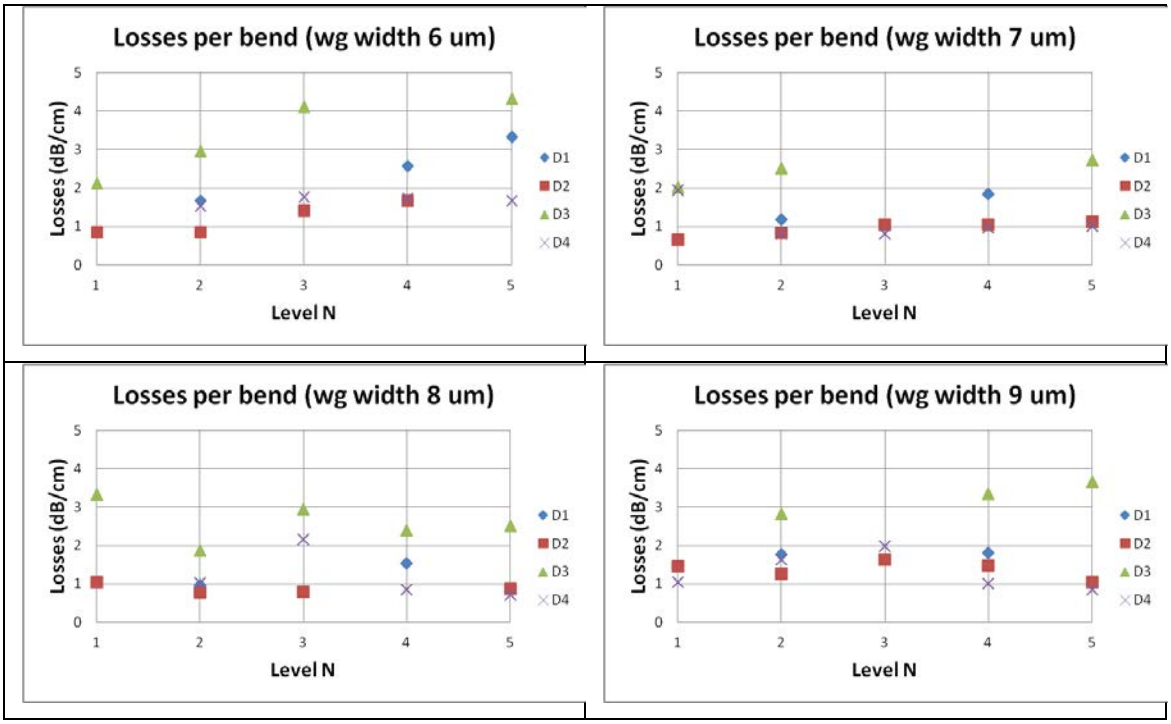

Table 4.4. Experimental measurements of the losses per Cosine bend as a function of the multiplexer level n

The results in Table 4.4 show losses per bend values between 0.7 and 2.3 dB and an ascending trend proportional to the multiplexer value **n,** which indicates a larger optical path, as the offset increases. These values were carefully selected as sample D3 presented major defects on the wall roughness of the waveguides.

Figure 4.13 presents the modeled attenuation per Sine S-bend. These results are shown separately from the Cosine function model (presented in Table 4.4) due to the low number

of measurements, as only two of the four fabricated samples contained viable Sine S-bend model waveguides. The results are shown in different code matching a waveguide width value ranging from 6 to 9 μm and combine the losses per bend as measured in all the valid samples.

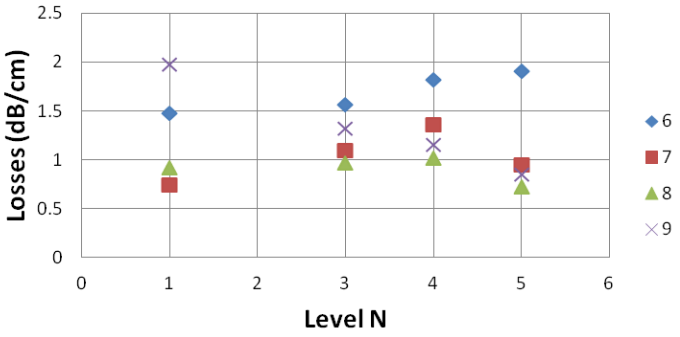

Figure 4.13. Experimental measurements of the losses per Sine bend as a function of the multiplexer level n

Results show losses per bend values between 0.67 and 2.0 dB, revealing a trend of increasing loss proportional to the multiplexer value **n**. Experimental results for the fabricated optical functions are in agreement with design and simulation results, confirming the feasibility of an InGaAs / InP epilayer structure to fabricate photonic building blocks to operate in the Mid-IR range

Complementary, Figure 4.14 shows the characterization results for the individual S-bend losses for both the Sine and Cosine function models for a waveguide width value of 6 μm. This value is important as it corresponds to the waveguide width selected for the multiplexer structures, both Y-junction and Echelle grating based.

The results are divided as a function of the multiplexer level in order to show the variations in magnitude for the different offset values and are shown in a different color set

matching the Sine and Cosine functions. The results were selected from the previously discussed results in Table 4.3 to match the multiplexer design parameters.

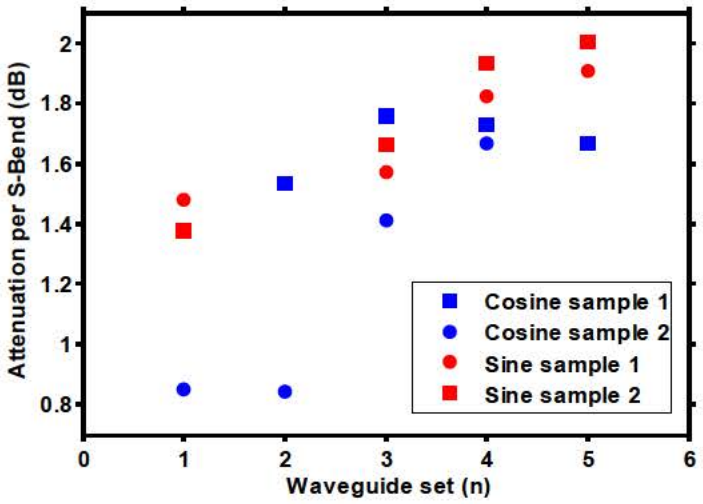

Figure 4.14. Experimental attenuation results for the S-bend structures

For the particular subset of results in Figure 4.14, attenuation per bend losses range from 1.37 to 2.0 dB. The results show an increasing trend in attenuation as the optical path for each bend increases. These results are in agreement with the simulated approach, discussed in Chapter II, and were expanded for higher values of **n**, showing an increasing trend in propagation losses. In the figure, two measurements present low attenuation which are not in agreement with the expected level of losses for individual bends, but their low value is not representative of the measurement set as closer inspection showed part of the light was being propagated through the substrate of the sample.

Based on this comparison, fewer transmission losses were observed in the cosine bends due to the smoothness of the curve in comparison to the sine bend model.

4.4 - Multiplexer scheme characterization

4.4.1 - Y-Junction based multiplexer structures

The Y-junction are 2-to-1 coupler BBs can are used to build optical (de)multiplexers that combine the light of two separated S-bend BBs. However, their BB design provides scalability in order to couple multiple inputs into a single output. Their use as customizable BBs allow for the design of more complex (de)multiplexer structures based on a tree configuration, where different Y-junction BBs are placed on a sequence (Figure 3.2 and Figure 3.5).

The objective is to design a monolithically capable 30-to-1 (de)multiplexer structure for its use as a de-risk design for the multiplexing of a DFB-QCL array with 30 emitters with a fixed spacing between them (QCLpitch) of 100 μm, as describe in Figure 3.2 and Figure 3.5.

Figure 4.15 shows the designed test structure in order to characterize the propagation losses for **n** value ranging from 1 to 5. This test structure is based in scalable 1:2 (1-to-2) S-bend Y-junction multiplexers that converge into a single output waveguide per (de)multiplexing level **n**. This design is used to calculate the cumulative propagation losses for the integrated multiplexer (Figure 3.2). The propagating light gets divided a maximum of 5 times (n=5), in correspondence to a (de)multiplexing ratio of 1:32 (1-to-32).

The fabricated samples included (de)multiplexer schemes using Cosine S-bend as that scheme presents a reduced free propagation region in the area where the two bent waveguides overlap in comparison with the Sine S-bend function. Each set is composed of

bent waveguides with specified bending radiuses required by a Y-junction tree to compel with a QCL pitch of 100 μm. We have analyzed the orders from the multiplexer level values n = 1 to n = 5.

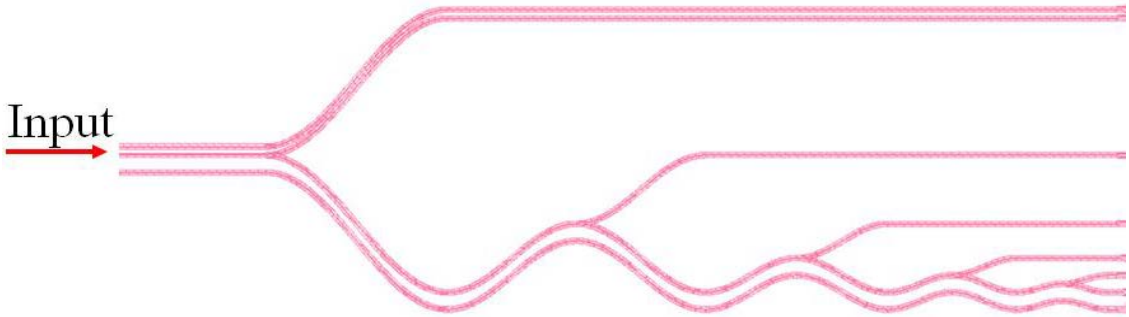

Figure 4.15.Inset of the Y-junction mux/demux test structure

The characterization was done in a demultiplexer orientation, where light was coupled from a QCL to the common input and was expected to propagate through both S-bends arms after splitting. Preliminary results were consistent with the individual bent losses and splitting losses were close to the theoretical value of 3 dB for each case.

The attenuation results for the (de)multiplexer scheme as well as their comparison with the simulated results and the power deviation per output are shown in Figure 4.16. They were obtained measuring the light intensity at each output when light from a λ=7.4 μm QCL source was injected at the common input. The results are normalized to the minimum loss value sets as the theoretical expected losses when n=1. However, the results show the relative attenuation between cumulative multiplexing levels for both theoretical and experimental results. Measurements follow the expected trend and the variation in the slope gradient, in comparison with the simulation, is due to additional loss coming from waveguide definition during processing and mode field overlap with the sidewall roughness,

as mentioned in previous results. The deviation per bend shows the deviation between the experimental characterization and theoretical models for every output, representing different multiplexing levels.

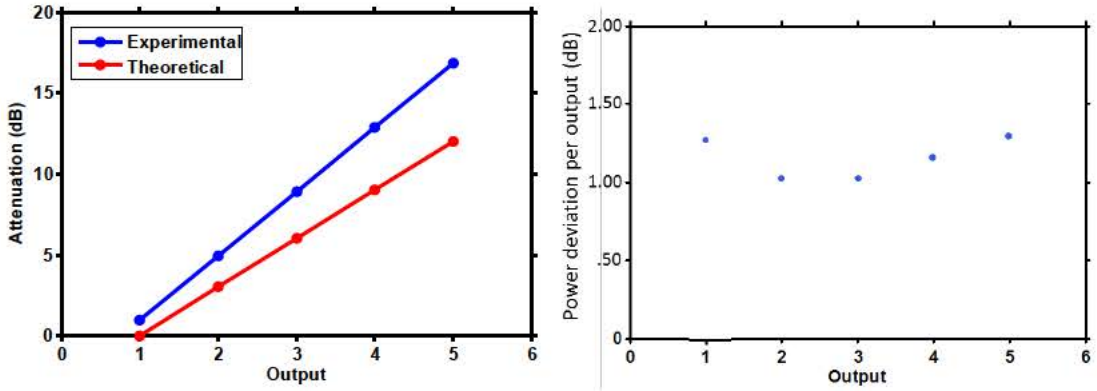

Figure 4.16. Comparison between experimental and theoretical attenuation for the mux/demux test structure (left) and deviation per output (right)

Experimental results for the fabricated optical functions are in agreement with design and simulation results. Scalability of such functions is also proven for structures such as multiplexer/demultiplexer. However, the propagation losses are considered too high for a monolithic integration with DFB-QCLs, as previous simulations had shown high losses for higher values of the input wavelength, which could result in higher power consumption of the integrated device as more power would be needed from the MIR sources.

4.4.2 - Echelle mirror characterization results for the 7 - 8.5 μm wavelength range

The last characterization effort was applied to the Echelle grating based (de)multiplexer BB designs. For this, a number of samples covering the 7-8.5 μm and 7-10 μm wavelength ranges were fabricated by following the same fabrication procedure as for the passive components with an additional step introducing a metallization procedure, which added a layer of Gold with a thickness of 50 nm to the facets of the grating in order to increase reflectivity. The final result of this added step can be observed in Figure 4.17.

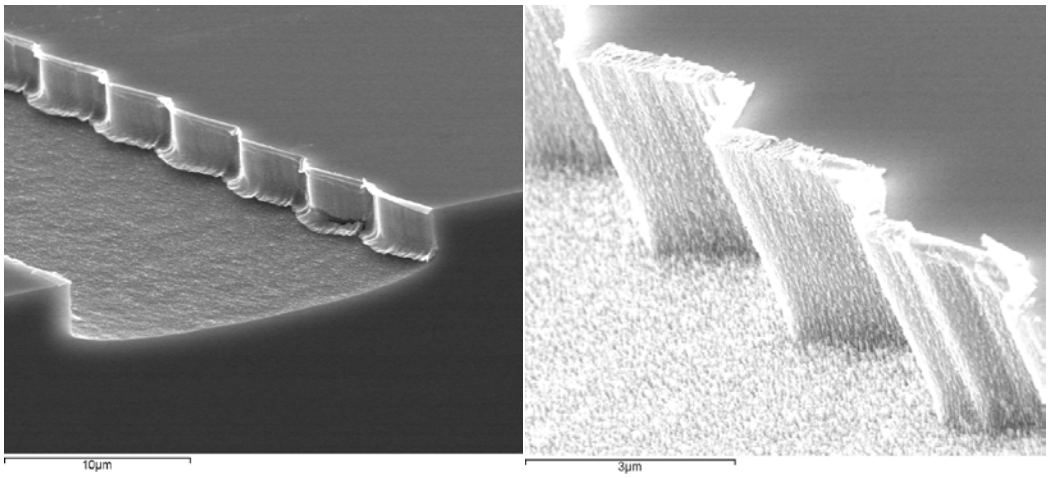

Figure 4.17.SEM pictures of the metallization of the Echelle grating

For the characterization of echelles, light was injected into the samples through the common output. Depending on the input light wavelength, the output power has to exit through the corresponding waveguide channel (Figure 4.20). The second step included the gathering of the light coming out of the device and channeled to an FTIR spectroscope in order to obtain spectral and transmission data for individual channels. Due to restrictions in the wavelength range of the input light source, the second step was only applied to the

samples of dual Echelle grating (de)multiplexer BBs working in the 7-8.5 μm wavelength range.

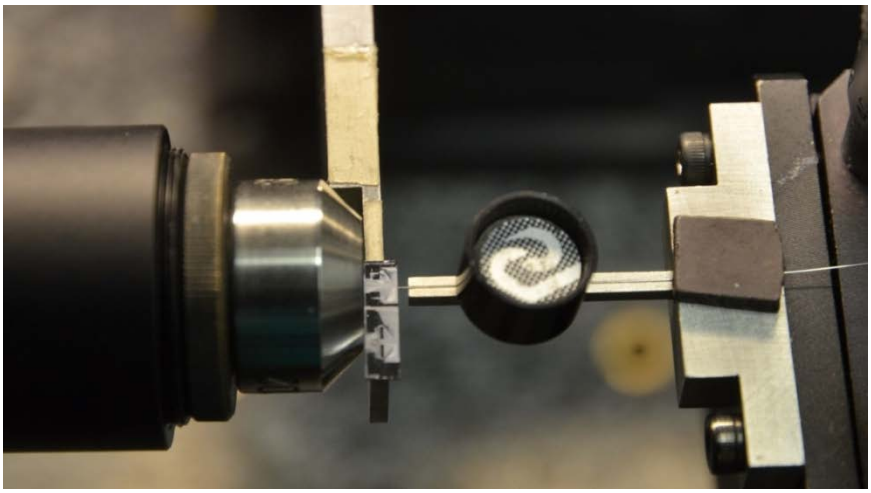

Figure 4.18. Close up of the bench showing an optic fiber used to collect the light coming out from a dual Echelle grating based multiplexer sample

As an additional design step, a series of output waveguides were added to the sides of the multiplexer output for every design. These additional output waveguides were introduced as a de-risk design procedure in the case the main output presents some error and were mentioned as input parameters in Table 4.5and Table 4.7 for the 7.-8.5 and 7-10 μm wavelength ranges respectively. However, as the main output waveguide is located in a focal position in relation to the grating, the wavelength range of these waveguides is directly proportional to the diffraction angle of the input waveguides. As a result, the wavelength of each output is shifted Δλ from the original wavelength spectrum of the design and the focal point may not be compatible for all the positions of the new introduced output waveguides. For identification purposes, these new output waveguides are named in a iΔλ fashion, where **i** is the waveguide identifier. The original output is represented with a value of i=0.

Figure 4.19 allows the identification of the spectral spacing between adjacent output waveguides (Δλ) on an Echelle grating (de)multiplexer BB. This value is not fixed and should be selected taking into account different design parameters. For the III-V Lab platform, the selected value corresponds to approximately the spectral separation between two adjacent channels in a certain (de)multiplexer design, and in the case of the dual Echelle grating BB, this spectral spacing must be double the value of the same design if a single Echelle grating model was selected.

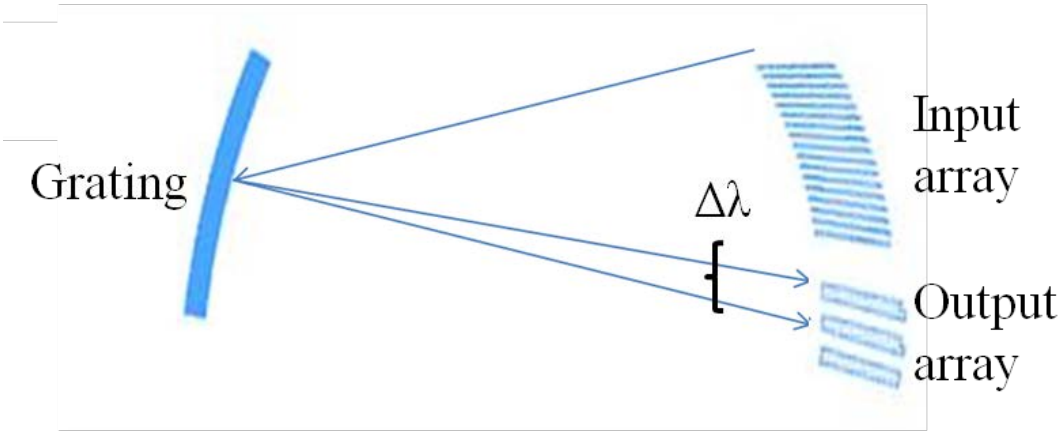

Figure 4.19. Depiction of the spectral spacing between adjacent output waveguides in an Echelle grating based (de)multiplexer

The introduced design parameter Δλ is selected as 0.1 μm and 0.2 μm for each of the subdesigns conforming a dual Echelle grating (de)multiplexer BB in the 7-8.5 and 7-10 μm wavelength range respectively.

Figure 4.20 shows the layout of a single Echelle grating (de)multiplexer BB, with the addition of the multiple output wavelengths, for a total of five. The figure also hints the propagation direction of the light for measurement purposes.

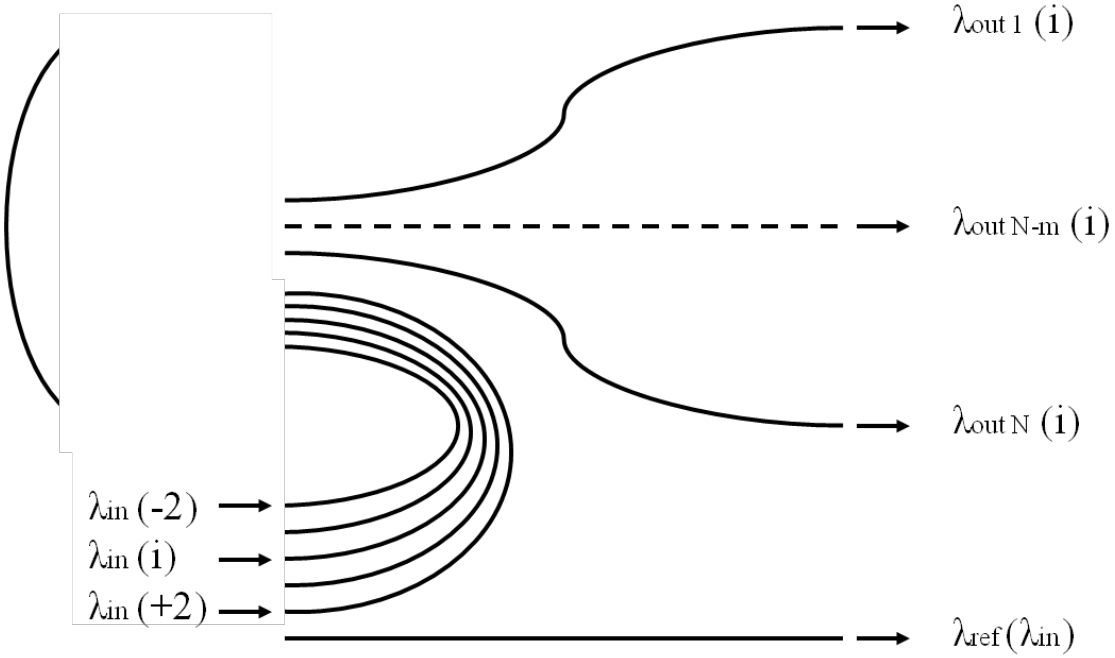

Figure 4.20. Depiction of the identification of the input/output waveguides in an Echelle grating based (de)multiplexer

As it has been mentioned, the first step in the characterization procedure was the coupling of light into the output waveguides of a sample BB with the use of a microscope objective. The light source was a DBF-QCL device with a broad wavelength peak working at 7.4 μm. The light was captured by direct observation with the IR camera at each of the inputs of the structure (Figure 4.9).

Table 4.5 shows the results of this characterization procedure. The first table of the column shows the expected central wavelength for each of the fifteen input waveguides as a function of the output waveguide (**i**) where light was introduced. The visual detection of light from a certain output is highlighted, confirming the multiple output array as a de-risk design technique.

λout(i)	λout(-2)	λout(-1)	λout(0)	λout(+1)	λout(+2)
7.0 + Δλ*i	6.8	6.9	7.0	7.1	7.2
7.1 + Δλ*i	6.9	7.0	7.1	7.2	7.3
7.2 + Δλ*i	7.0	7.1	7.2	7.3	7.4
7.3 + Δλ*i	7.1	7.2	7.3	7.4	7.5
7.4 + Δλ*i	7.2	7.3	7.4	7.5	7.6
7.5 + Δλ*i	7.3	7.4	7.5	7.6	7.7
7.6 + Δλ*i	7.4	7.5	7.6	7.7	7.8
7.7 + Δλ*i	7.5	7.6	7.7	7.8	7.9
7.8 + Δλ*i	7.6	7.7	7.8	7.9	8.0
7.9 + Δλ*i	7.7	7.8	7.9	8.0	8.1
8.0 + Δλ*i	7.8	7.9	8.0	8.1	8.2
8.1 + Δλ*i	7.9	8.0	8.1	8.2	8.3
8.2 + Δλ*i	8.0	8.1	8.2	8.3	8.4
8.3 + Δλ*i	8.1	8.2	8.3	8.4	8.5
8.4 + Δλ*i	8.2	8.3	8.4	8.5	8.6

Table 4.5. Experimental results for subdesign A of a dual Echelle grating (de)multiplexer BB in the 7-8.5 μm range. Highlighted cells indicate light detection in the outputs

The resulting table shows the detection of light in other input waveguides surrounding the input that corresponds to the introduced wavelength. The cause of this effect lies in the roughness of the grating facets, as minimum deviations directly affect the diffraction angle of the incident light, and a secondary reason is that focal point of the design is cannot be optimized for all output waveguides working at the same moment. However, given that the introduction of light via the output waveguides is just for testing measurements; this effect does not affect the multiplexer capabilities of the structure. Future optimization stages may introduce new techniques to reduce this effect.

As introduced in 0, the device characterization for these structures was also done by the use of an EC-QCL tunable from 7.3 to 8.6 μm, coupled into the output waveguides of the design using a microscope objective. Light was collected in the input waveguides using a

multimode AsSe fiber and then focused on a pyroelectric deuteraded triglycine sulfate (DTGS) detector and spectrally analyzed by Fourier transform infrared spectroscopy.

Constant voltage, frequency, duty cycle and temperature were applied to the EC-QCL to have a constant output power at a given position of the EC grating. The laser was operated at a temperature of 20°C in pulsed regime (1% duty cycle and 300 kHz repetition rate). Under these experimental conditions and preliminary tests, constant input power is ensured from one waveguide to another. Transmission loss can therefore be directly estimated by comparing the power levels of multiplexer outputs and out of the reference waveguide, located next to the multiplexer (Figure 4.20).

Since the linewidth of the EC-QCL is narrower than the transmission window of one channel, the wavelength is scanned over the achievable tuning of the EC-QCL source in order to span the transmission window of one channel. In that way, each transmission spectrum is reconstructed taking all maxima over the entire wavelength range.

Figure 4.22 (a) shows the measured transmission spectrum of thirteen adjacent input channels of a single subdesign of a double Echelle grating (de)multiplexer BB for a TE polarized input MIR source. The two remaining channels could be not measured at lower wavelength because their central wavelength fell outside the tuning range of the laser source. The channel spacing is about 98±20 nm. Wavelength channels present transmission losses ranging from -18 dB to -24 dB and the channel crossing is about 3 dB. Channel transmission linearly decreases between 7.3 and 8.2 μm, from -18 to -21 dB, this effect is attributed to higher propagation losses.

Beyond the 8.3 μm wavelength, the channel transmission collapses in direct association to operation near cut-off wavelength of the bent waveguides.

In addition, Figure 4.22 (b) shows the measured transmission spectra of twelve adjacent channels covering the wavelength range of 7.3 to 8.3 μm for a TM polarized input MIR source. Channel thirteen could not be measured wavelengths values higher than 8.3 μm due to low level collected power, lower than the experimental noise. The channel spacing is about 97±27 nm, which is a good agreement with the target value of 100 nm. The figure also shows a slight deviation in the central wavelength of 29 nm at 7.7 μm, as well as the experimental linear dispersion coefficient of 85.6 μm/μm. This deviation effect is attributed to the deviation of refractive indexes due to uncertainties in the alloy composition $InGa_xAs_{1-x}$ and the deviation from the exact geometry due to fabrication tolerances and can therefore be optimized in following designs. Channel crossing was measured to appear at about 2 dB and guarantees good power regularity among the channels. However, insertion losses are higher than the simulated value of -1.9 dB and rank from -18 to -31 dB; this difference in losses can be caused by a number of reasons; roughness and angled facets in the grating are the most plausible. In order to illustrate that, a variation in the setup was done so the IR camera was placed facing the sample surface when different wavelengths were introduced, Figure 4.21 confirms that the scattered light is a major source of loss and is proportional to the input wavelength. An additional source of loss is the bend losses as a function of the wavelength, as higher values of the propagating wavelength present higher attenuation (Chapter II).

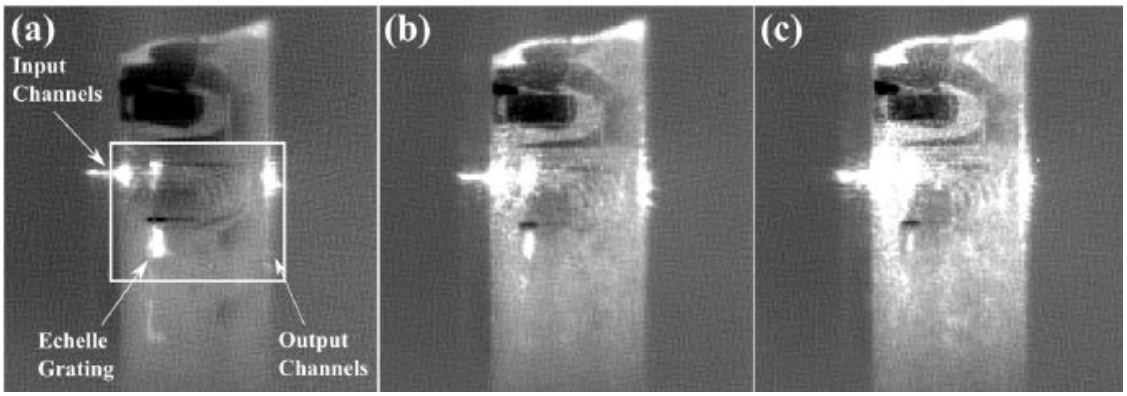

Figure 4.21. Images captured by the IR camera of the scattered light from the multiplexer waveguides. The coupled light is (a) 7.83 μm, (b) 8.13 μm and (c) 8.40 μm

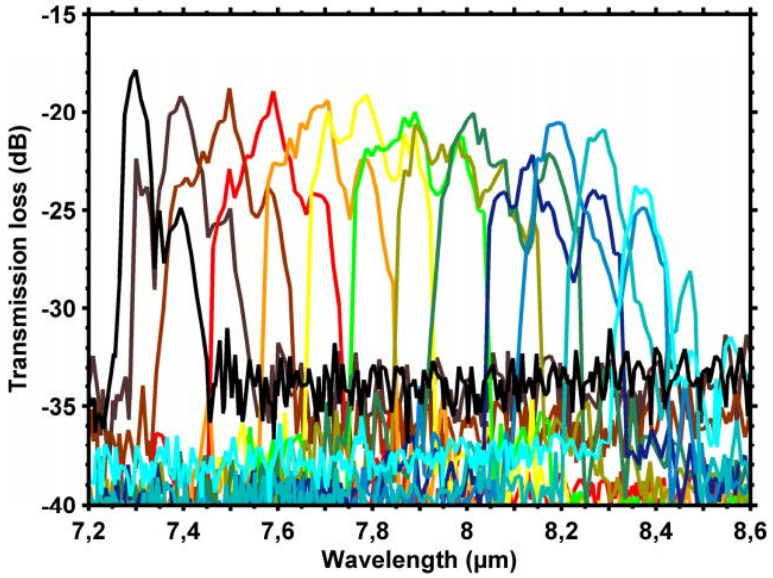

(a)

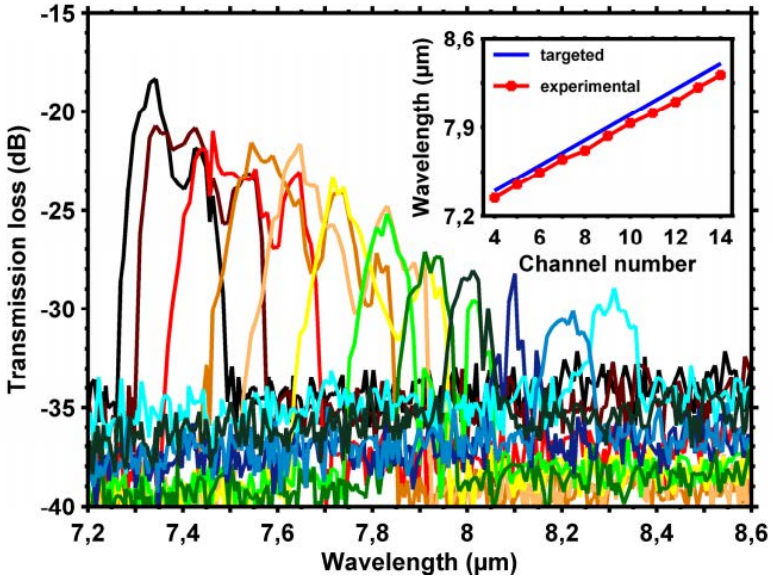

(b)

Figure 4.22. Spectral responses of thirteen of fifteen multiplexer input channels for TE polarized light (a). Spectral responses of twelve of fifteen multiplexer input channels for TM polarized light (b). Inset: comparison between the experimental central wavelengths and expected values over the input waveguide array

4.4.3 - Echelle mirror characterization results for the 7 – 10.0 μm wavelength range

The last experimental characterization has been the measurement of samples with dual Echelle grating (de) multiplexers in the 7-10 μm range. This characterization effort follows the same preliminary procedure for the testing of the 7-8.5 μm (de) multiplexer BBs where light sources were injected in the common output of the device in a demultiplexer orientation and depending on the input light wavelength; the output power has to exit through the corresponding waveguide channel.

The light sources were DBF-QCLs working at 7.4 and 8.2 μm and the light was captured by direct observation with the IR camera at each of the inputs of the structure in the same fashion as detailed in 0.

The introduction of this new 8.2 μm wavelength source is done so that light propagation is proven for longer wavelengths; however, injection of longer wavelengths was not possible, as the device presented high insertion losses confirming the cut-off frequency of the waveguide and the epilayer structures for a wavelength value of 8.5 μm.

Table 4.6 and Table 4.7 show the light detection results for two different dual Echelle grating (de) multiplexer BB samples, the tables are divided in two different subdesigns with the central wavelength of the input channel clearly marked as a function of the output channel in which the light is injected.

Results with darker color indicate light detection. In order to introduce a grade of variation, the minimum radius between the two samples is different; while sample 1 presents a minimum radius of 200 μm, sample 2 uses a 170 μm.

λout(i)	λout(-2)	λout(-1)	λout(0)	λout(+1)	λout(+2)
7.0 + Δλ*i	6.6	6.8	7.0	7.2	7.4
7.2 + Δλ*i	6.8	7.0	7.2	7.4	7.6
7.4 + Δλ*i	7.0	7.2	7.4	7.6	7.8
7.6 + Δλ*i	7.2	7.4	7.6	7.8	8.0
7.8 + Δλ*i	7.4	7.6	7.8	8.0	8.2
8.0 + Δλ*i	7.6	7.8	8.0	8.2	8.4
8.2 + Δλ*i	7.8	8.0	8.2	8.4	8.6
8.4 + Δλ*i	8.0	8.2	8.4	8.6	8.8
8.6 + Δλ*i	8.2	8.4	8.6	8.8	9.0
8.8 + Δλ*i	8.4	8.6	8.8	9.0	9.2
9.0 + Δλ*i	8.6	8.8	9.0	9.2	9.4
9.2 + Δλ*i	8.8	9.0	9.2	9.4	9.6
9.4 + Δλ*i	9.0	9.2	9.4	9.6	9.8
9.6 + Δλ*i	9.2	9.4	9.6	9.8	10.0
9.8 + Δλ*i	9.4	9.6	9.8	10.0	10.2
λout(i)	**λout(-2)**	**λout(-1)**	**λout(0)**	**λout(+1)**	**λout(+2)**
7.1 + Δλ*i	6.7	6.9	7.1	7.3	7.5
7.3 + Δλ*i	6.9	7.1	7.3	7.5	7.7
7.5 + Δλ*i	7.1	7.3	7.5	7.7	7.9
7.7 + Δλ*i	7.3	7.5	7.7	7.9	8.1
7.9 + Δλ*i	7.5	7.7	7.9	8.1	8.3
8.1 + Δλ*i	7.7	7.9	8.1	8.3	8.5
8.3 + Δλ*i	7.9	8.1	8.3	8.5	8.7
8.5 + Δλ*i	8.1	8.3	8.5	8.7	8.9
8.7 + Δλ*i	8.3	8.5	8.7	8.9	9.1
8.9 + Δλ*i	8.5	8.7	8.9	9.1	9.3
9.1 + Δλ*i	8.7	8.9	9.1	9.3	9.5
9.3 + Δλ*i	8.9	9.1	9.3	9.5	9.7
9.5 + Δλ*i	9.1	9.3	9.5	9.7	9.9
9.7 + Δλ*i	9.3	9.5	9.7	9.9	10.1
9.9 + Δλ*i	9.5	9.7	9.9	10.1	10.3

Table 4.6. Experimental results of sample 1 of a dual Echelle grating (de)multiplexer BB in the 7-10.0 μm range. Highlighted cells indicate light detection in the outputs

λout(i)	λout(-2)	λout(-1)	λout(0)	λout(+1)	λout(+2)
7.0 + Δλ*i	6.6	6.8	7.0	7.2	7.4
7.2 + Δλ*i	6.8	7.0	7.2	7.4	7.6
7.4 + Δλ*i	7.0	7.2	7.4	7.6	7.8
7.6 + Δλ*i	7.2	7.4	7.6	7.8	8.0
7.8 + Δλ*i	7.4	7.6	7.8	8.0	8.2
8.0 + Δλ*i	7.6	7.8	8.0	8.2	8.4
8.2 + Δλ*i	7.8	8.0	8.2	8.4	8.6
8.4 + Δλ*i	8.0	8.2	8.4	8.6	8.8
8.6 + Δλ*i	8.2	8.4	8.6	8.8	9.0
8.8 + Δλ*i	8.4	8.6	8.8	9.0	9.2
9.0 + Δλ*i	8.6	8.8	9.0	9.2	9.4
9.2 + Δλ*i	8.8	9.0	9.2	9.4	9.6
9.4 + Δλ*i	9.0	9.2	9.4	9.6	9.8
9.6 + Δλ*i	9.2	9.4	9.6	9.8	10.0
9.8 + Δλ*i	9.4	9.6	9.8	10.0	10.2
λout(i)	λout(-2)	λout(-1)	λout(0)	λout(+1)	λout(+2)
7.1 + Δλ*i	6.7	6.9	7.1	7.3	7.5
7.3 + Δλ*i	6.9	7.1	7.3	7.5	7.7
7.5 + Δλ*i	7.1	7.3	7.5	7.7	7.9
7.7 + Δλ*i	7.3	7.5	7.7	7.9	8.1
7.9 + Δλ*i	7.5	7.7	7.9	8.1	8.3
8.1 + Δλ*i	7.7	7.9	8.1	8.3	8.5
8.3 + Δλ*i	7.9	8.1	8.3	8.5	8.7
8.5 + Δλ*i	8.1	8.3	8.5	8.7	8.9
8.7 + Δλ*i	8.3	8.5	8.7	8.9	9.1
8.9 + Δλ*i	8.5	8.7	8.9	9.1	9.3
9.1 + Δλ*i	8.7	8.9	9.1	9.3	9.5
9.3 + Δλ*i	8.9	9.1	9.3	9.5	9.7
9.5 + Δλ*i	9.1	9.3	9.5	9.7	9.9
9.7 + Δλ*i	9.3	9.5	9.7	9.9	10.1
9.9 + Δλ*i	9.5	9.7	9.9	10.1	10.3

Table 4.7. Experimental results of sample 2 of a dual Echelle grating (de)multiplexer BB in the 7-10.0 μm range. Highlighted cells indicate light detection in the outputs

Sample 1 presented a number of defects in one of the output waveguides; specifically the one for the i=-2 waveguide, making the propagation of light not possible.

The results show an observable difference in the intensity of the gathered light between the two samples for the light source of 8.2 μm, which was severely reduced in the case of sample 2. The reason of his difference in power is the effect of the bending as a major source of loss when the wavelength value increases along the studied range. This effect was observed in the spectral characterization of the 7-8.5 μm samples for both TE and TM polarizations (Figure 4.22).

The second step in the characterization procedure was not followed for this wavelength range. The reason for this is that the EC-QCL has a narrower tuning range in comparison with the multiplexer range (7-10 μm), and it was determined that further optimization of the epilayer structure and the waveguide parameters was necessary in order to increase the cut-off frequency of this devices.

4.5 - Discussion and Remarks

In this chapter, the fabrication and characterization efforts for passive Building Block samples in the scope of the MIRIFISENS project are discussed. This work seeks to provide a proof of concept for the BB designs in Chapters II and III as a preliminary step before the monolithic integration of such designs into a widely tunable MIR source along with DFB-QCL arrays.

The first step is the description of the test mask design including necessary passive optical functions. This mask was a necessary starting point for the fabrication process that followed and the designs contained on it are detailed.

The device fabrication procedure was done by III-V Lab and consisted in two separate attempts. The first of them allowed for the optimization of the fabrication process, as defects such as bad quality of the vertical etching and missing transferred patterns from the mask were noticed. The second attempt provided successful results and with them, the characterization efforts on the fabricated samples took place.

The characterization process was done by the injection of MIR light into the samples with the use of microscopic lenses. For this, two different light sources were used according to the kind of passive device of the sample; those sources were a pulsed current driver controlling a number of individual pulsed DFB-QCLs and a widely tunable EC-QCL source. The light was then collected from the samples and guided to a fast detector or to a

FTIR with a MIR fiber. To ensure correct insertion and collection of the light, a QWIP IR camera was used for direct observation of the waveguides.

The characterization results for the straight and bent waveguides were obtained by measuring the transmission contrast of the Fabry-Perot fringes inside the cavity formed by opposite cleaved facets of the waveguides. The results showed good accordance with the simulated waveguiding analysis approach detailed in Chapter II and are summarized in the following table.

	Propagation loss for all waveguide width values	Propagation loss for wg width = 6 μm
Straight waveguides	2.1 – 3.4 dB/cm @ 7.4 μm 3.3 – 4.1 dB/cm @ 8.7 μm	3.0 dB/cm @ 7.4 μm
Bent Waveguides: Sine Cosine	0.70 – 2.0 dB/bend @ 7.4 μm 0.67 – 2.0 dB/bend @ 7.4 μm	1.37 – 2.0 dB/bend @ 7.4 μm

Table 4.8. Summarization of the propagation loss for the straight and bent waveguides

A series of multiplexer structure including Y-junction and Echelle grating based structures were also fabricated and characterized. Both schemes were studied in a demultiplexer orientation.

The characterization results for the Y-junction scheme follow the expected trend in attenuation and the variation in the slope gradient is due to additional loss coming from the waveguide definition (sidewall roughness). However, this scheme is not recommended for the final application as the resulting footprint is too large (1.5×10^7 μm^2) and the level of losses increases drastically as a function of the propagating wavelength (Chapter II).

The last step in the characterization process was done to Echelle grating based multiplexers covering two different wavelength ranges:

- 7.00 – 8.50 μm (1176.5 – 1428 cm^{-1})
- 7.00 to 10.00 μm (1000 - 1428 cm^{-1})

For both ranges, a 7.4 μm DFB-QCL source was injected in the outputs in order to observe light coming out from the correct input waveguides. With this, the correct channel multiplexing was confirmed for the devices. An additional 8.7 μm DFB-QCL source was used in the 7-10 μm device, as the multiplexer range is greater.

A widely tunable EC-QCL pulsed MIR source was then used to inject light into the central output for the spectral characterization of one of the subdesigns of the 7.0 – 8.5 range multiplexer. Wavelength channels observed in the FTIR presented losses ranging from 18 to 24 dB and a channel crossing of 3 dB for the TE polarization of the input light. TM polarization results showed losses ranging from 18 to 31 dB and the channel crossing was about 2 dB. The difference in losses in comparison with the simulated model is caused by sidewall roughness of the waveguides and diffraction errors due to the grating facets.

With this, MIR multiplexing was demonstrated for the first time in the 7 – 10 μm range in a InGaAs/InP platform. The work demonstrates the potential to monolithically integrate light generation and passive optical functions within a single device, despite the high losses.

4.6 - References

[1] L. J. Orbe, G. Carpintero, C. Gilles, F. Boulila, G. Maisons, M. Carras, "Characterization of an InGaAs/InP-based Echelle Mirror Multiplexer for Widely Tunable Mid-IR Sources Based on Quantum Cascade Lasers," SPIE Photonics West (2015)

[2] L. J. Orbe, C. Gordon, G. Carpintero, G. Maisons, M. Carras, "InGaAs/InP-based Echelle mirror multiplexer using dual Rowland circle gratings for DFB QCL arrays in the mid-long infrared range," SPIE Photonics West (2014)

[3] Coldren,L.; Corzine,S.; Mashanovitch, M.; "Diode Lasers and Photonic Integrated Circuits" (Second ed.), Wiley (2012)

[4] M. Carras ; G. Maisons ; B. Simozrag ; V. Trinite ; M. Brun ; G. Grand ; P. Labeye ; S. Nicoletti; "Monolithic tunable single source in the mid-IR for spectroscopy"; Proc. SPIE 8631, Quantum Sensing and Nanophotonic Devices X, 863113 (February 4, 2013)

[5] Maisons, G.; Carras, M.; et al; "Advances toward monolithic tunable source," ISLC (2014)

[6] R. G. Walker, "Simple and accurate loss measurement technique for semiconductor optical waveguides," Electronics Letters 21(13), 581-583 (1985).

[7] D. G. Revin et al, "Measurements of optical losses in mid-infrared semiconductor lasers using Fabry–Pérot transmission oscillations", JAP95(12) (2004).

Conclusions and Future Work

5.1 - Final conclusions

Within this thesis, we have developed the design, simulation and characterization of new passive components to implement optical functions leading to implement optical multiplexing for Quantum Cascade Laser (QCL) arrays in the mid-infrared (MIR) frequency range. This work aims to develop widely tunable sources for sensing applications.

As has been described in this work, the current state-of-the-art on this topic provides a few alternative options with promising results based on External Cavity Quantum Cascade Lasers (EC-QCLs) [18] . However, these solutions usually require external instrumentation, leading to bulky and complex systems. Some of these efforts have aimed to miniaturization, through monolithic active/passive integration, achieving narrow bandwidths ranging only up to a couple of microns [2] [3] . This is the problem that we have addressed, developing a design methodology based on Building Blocks (BBs) that provides scalability and improves the bandwidth.

The detailed methodology is based on the mid-infrared Quantum Cascade Laser epitaxy developed by III-V Lab, one of the foundries producing these kinds of components. The active/passive integration technology for this QCL platform has been developed within the framework of project FP7-MIRIFISENS.

Based on this epitaxy, we have demonstrated for the first time to our knowledge, passive optical functions in an InP/InGaAs platform for the MIR range. Experimental results were in accordance with the simulation approach, providing insight in the effect of

the propagation losses as a function of the design parameters and propagating wavelength in the MIR.

These results were the base for the design of MIR broadband multiplexers. The designs were presented in two different approaches: First, a Y-junction based multiplexer was introduced and its characterization results confirmed the scalability properties of a BB based design. However the increased propagation losses due to the bent waveguides and large footprint encouraged the introduction of other multiplexer approaches.

The second approach was the design and demonstration for the first time of InP/InGaAs MIR broadband Echelle grating based multiplexers in the 7 – 10 μm (1000 – 1428 cm^{-1}) wavelength range. These designs were optimized in order to potentiate channel crosstalk and reduce the total area of the optical circuit.

The experimental results of these devices confirm the potential of Echelle grating multiplexers to be used in widely tunable MIR sources when combining with DFB-QCL arrays in monolithically integrated designs, and serve as the base for future optimization efforts.

5.2 - Future work

The methodology and results in this document correspond to the first and second fabrication test runs in the framework of the FP7-MIRIFISENS project. The project planning contemplates further optimization procedures in the design stages and future multiplexer designs. The main focus of the incoming work will be centered in the optimization of the Echelle grating multiplexers, along with any fabrication process this optimization would need.

Further optimization efforts over the basic bending blocks is also needed, as the performance of the Echelle multiplexers can be considerably enhanced with careful design of bends and waveguide spacing in order to prevent from radiation and coupling losses respectively.

Further designs have been proposed for a third fabrication test run; however, they have not been included in this work, as their fabrication and characterization efforts have not started yet. These designs introduce changes in the waveguide thickness and bending radius in order to decrease insertion losses in the input and output waveguides. Other design variations include output waveguide placements and waveguide crossings.

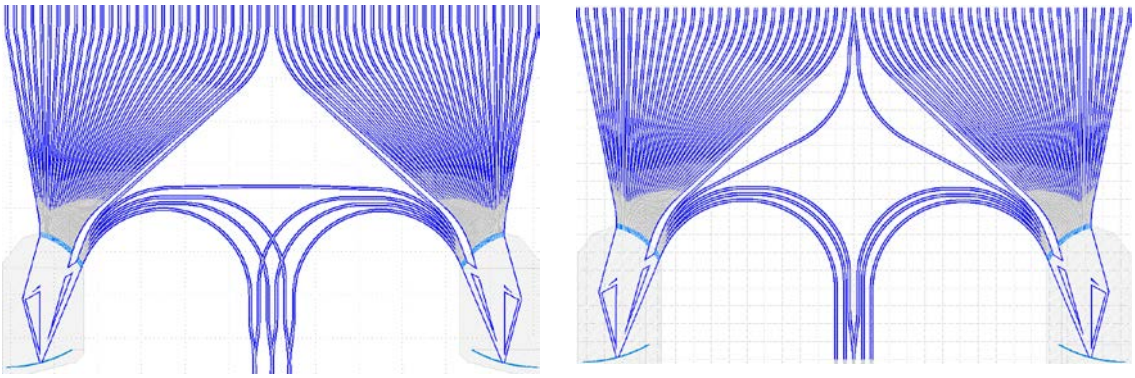

Figure 5.1. Second stage dual Echelle grating (de)multiplexer designs: crossed output scheme (left) and bilateral output scheme (right)

The introduction of distributed Bragg reflectors for the grating facets is a secondary proposed line of work. This effort will suggest the development of a complete numerical model which includes major loss mechanisms for improvement of the multiplexer performance.

At the moment, no further characterization efforts are expected for the presented devices; however, future fabrication runs will follow the presented methodology and a comparison of the performance between the different runs will be achieved.

5.3 - Acknowledgements

This work has received funding from the European Union Seventh Framework Program (FP7/2007-2013) under grant agreement n°317884, the collaborative Integrated project MIRIFISENS.

III-V Lab would like to acknowledge das Fraunhofer-Institute für Angewandte Festkörperphysik for the external cavity quantum cascade laser used during characterization of the 7-8.5 µm Echelle grating (de)multiplexer.

5.4 - References

[1] Hugi, A., et al.,"External Cavity Quantum cascade laser Tunable from 7.6 to 11.4 μm", Appl. Phys. Lett., 95, pg. 061103 (2009).

[2] Hugi, A.; Wittmann, A.; Bonetti, Y.; Gini, E.; Beck, M.; Faist, J., "Broadband external cavity quantum cascade laser," in *Lasers and Electro-Optics 2009 and the European Quantum Electronics Conference. CLEO Europe - EQEC 2009. European Conference on* , vol., no., pp.1-1, 14-19 June 2009

[3] Tsai, T.; Wysocki, G., "Fast wavelength tuning of external cavity quantum cascade lasers," in *Lasers and Electro-Optics, 2009 and 2009 Conference on Quantum electronics and Laser Science Conference. CLEO/QELS 2009. Conference on* , vol., no., pp.1-2, 2-4 June 2009

Publications and Collaborations Based on this Work

Design and Experimental Characterization of Mid Infra-Red (MIR) Photonic Integrated Circuit Building Blocks

L. J. Orbe,*[1] C. Gilles,[2] G. Maisons,[2] G. Carpintero,[1] M. Carras[2]

Submitted to OSA Optics Letters

We report the design, fabrication and characterization of Photonic Integrated Circuit components based on an InP/InGaAs platform to develop a Mid-Infrared (Mid-IR) monolithically integrated system. The components were optimized for the spectral range from 7 to 10 μm, demonstrating basic Building Blocks in this platform realizing functionalities from straight waveguides, Sine and Cosine S-Bends to Y-junctions. We present the main design parameters and the overall losses, key elements to be addressed for the design of an optical multiplexer which will be monolithically integrated with a Quantum Cascade Laser (QCL) array to achieve a broadband tunable Mid-IR source. Experimental characterization data shows losses as low as 2.4 dB/cm at λ=7.4 μm and 3.3 dB/cm at 8.7 μm for straight waveguides. Experimental results for basic photonic functions are reported, demonstrating their potential for monolithic integration in MIR systems for spectroscopic applications.

Mid-infrared wavelength multiplexer in InGaAs/InP waveguides using a Rowland circle grating

C. Gilles, L. J. Orbe, G. Carpintero, G. Maisons, M. Carras

Submitted to OSA Optics Express

We report the monolithic integration of a 15-channel multiplexer on indium phosphide. It covers the 7.1-to-8.5 μm wavelength range suitable for combining the outputs of several individual lasers. The fabrication is compatible with the growth of active layers, therefore enabling a fully integrate broadband laser source in the mid-infrared spectral range. Channels are accurately spaced in wavelength (97 nm) in good agreement with design.

Characterization of an InGaAs/InP-based Echelle Mirror Multiplexer for Widely Tunable Mid-IR Sources Based on Quantum Cascade Lasers

L. J. Orbe*[a], G. Carpintero[a], C. Gilles[b], F. Boulila[b], G. Maisons[b], M. Carras[b]

SPIE PHOTONICS WEST 2015, Proc. SPIE. 9002, Novel In-Plane Semiconductor Lasers XIV

We present the experimental characterization results of a 15-to-1 wavelength multiplexer for a Distributed Feedback Quantum Cascade Laser (DFB QCL) array operating in the 7-8.5 μm (mid-long) infrared (IR) range. This design is customized for its use to combine the output from a DFB QCL array with a 0.1 μm wavelength channel

spacing for spectroscopy applications, and it is proposed in order to achieve a continuous tuning range overcoming the limited tunability of a single QCLs, required for multi-gas or complex molecule detection.

This multiplexer is based on an Echelle diffraction mirror grating scheme, in which multiple output waveguides are deliberately implemented in the design to de-risk for wavelength deviations in the fabrication process. We optimized the location of the input and output guides in order to allow for monolithic integration of the DFB QCL arrays, which would provide for a number of advantages such as a higher stability, less complexity and lower cost over other technologies such as external cavities.

We discuss the effects over the device performance of the design, such as the diffraction effects, input channel width overlapping/crosstalk and input channel profile, which are very important to address in order to avoid unaccounted transmission losses. Other parameters such as the profile of the input and output waveguides and fabrication limitations are also discussed as their effect on the device is observed.

A series of characterization tests are presented in order to compare the simulation results to the experimental data, which suggests that these multiplexers are a suitable option compared to other IR multiplexer schemes in terms of size and power transmission.

MIR Photonic Integrated Circuits for Laser Spectroscopy

L. J. Orbe, G. Carpintero, G. Maisons, C. Gilles, F. Boulila, M. Carras

MIOMD - Mid-IR Optoelectronics : Materials and Devices 2014

In laser-based optical stand-off spectroscopy, laser radiation interacts with gas chemical substances which have absorption lines over the Mid-Infrared (MIR) spectrum. Low-cost, small-footprint and widely tunable laser sources in this range can potentially have a huge impact on the development of Tunable Diode Laser Spectroscopy instruments.

Quantum Cascade Lasers (QCL) are coherent light sources in the MIR range, attracting great interest in covering the MIR for sensing applications. Currently, Distributed Feedback (DFB) QCLs provide a narrow-linewidth single-mode emission spectrum which is perfectly suited for trace gas detection, requiring wavelength tuning of a few tens of wavenumbers to detect multiple gas species. DFB QCLs have demonstrated wide wavelength range operation from the MIR to the Terahertz and achieve high output powers in continuous-wave operation at room temperature. The only drawback is that a single DFB QCL has a limited tuning range. In order to overcome this issue, arrays of DFB QCL, composed of tenths of emitters have been developed as a solution for broad tunability.

The main objective of is to develop a MIR Photonic Integrated Circuit (PIC) through the monolithic integration of the QCL array and a multiplexer scheme achieving a widely tunable source in the MIR range suitable for laser spectroscopy. In order to pursue that objective, we present our recent advances in passive multiplexer schemes in order to achieve

monolithic integration with the DFB QCL array, which include a comparison between numerical simulations and experimental results for all of the components of the PIC toolbox, a waveguiding analysis and multiplexer schemes, such as Y-junction and Echelle grating based multiplexers. Experimental results show propagation losses as low as 2 dB/cm at 7.4 μm for straight waveguides. Experimental results over Y-junction and Echelle multiplexers were also obtained and compared to the expected values.

We will highlight the use of Echelle gratings as the optimum multiplexer solution, as they present advantages such as size reduction and minimized diffraction aberrations as well as size advantage in comparison to other multiplexer schemes; which make them ideal for compact low cost applications.

Advances toward monolithic tunable source

Autores: G. Maisons, C. Gilles, B. Simozrag, M. Carras, M. Brun, P. Labeye, P. Barritault, S. Nicoletti, L. J. Orbe, G. Carpintero

ISLC 2014 – IEEE 24TH INTERNATIONAL SEMICONDUCTOR LASER CONFERENCE

We present the realizations of an array of Distributed Feedback (DFB) Quantum Cascade Lasers (QCL) and passive Multiplexers (MUX) based on Silicon or Indium Phosphide wafers. The aim of these preliminary results is to realize a monolithic, widely tuneable, source in the Mid-InfraRed (MIR) for laser spectroscopy. In the MIR region the DFB Quantum Cascade Lasers (QCL) are among the favoured sources for the Laser

Spectroscopy [1]. In order to detect complex molecules or a set of simple molecules, one needs a narrowlinewidth tunable source suitable to scan few tens of wavenumbers. Single DFB QCL have a limited tuning range (< 10 cm^{-1}) and can only be used for one or two simple molecules. External cavities are widely tunable [2] however they could suffer from mechanical vibrations and are not relevant for miniaturized spectroscopic system. To achieve a broadband source, a DFB array needs tens of emitters. This configuration is not suitable for integration in a spectroscopic system and optical sources have to be multiplexed to get only one beam. External solution could be use [3] however, for the same reasons external cavities have been dismissed, a monolithic approach is preferable to combine all optical beams. These optical multiplexing needs low losses passive waveguide which cover all the spectral range. Monolithic tuneable sources [Fig. 1] are very appealing for spectroscopy applications because of the compactness, the robustness and the usability.

QCL-based photonic integrated circuits on InP and other platforms – Invited Talk

Autores: L. J. Orbe, G. Carpintero, G. Maisons, M. Carras

IPRM - International Conference on Indium Phosphide and Related Materials / 2014

We will present our work toward the realization of a monolithic broadly tunable source in the mid infrared (MIR) based on quantum cascade laser sources (QCL). We'll start by presenting the development on distributed feedback (DFB) QCL laser arrays; introduce the design, optimization, simulation and experimental characterization. Then we will focus on

the passive components, namely a 30-to-1 wavelength multiplexer operating in the 7-8.5 μm (mid-long) infrared (IR) range based on an Echelle mirror using a dual Rowland circle grating scheme. These designs are proposed in order to achieve a continuous tuning range overcoming the limited tunability of individual QCLs.

InGaAs/InP-based Echelle mirror multiplexer using dual Rowland circle gratings for DFB QCL arrays in the mid-long infrared range

Authors: L. J. Orbe; C. Gordon; G. Carpintero; G. Maisons; M. Carras

SPIE PHOTONICS WEST, Proc. SPIE. 9002, Novel In-Plane Semiconductor Lasers XIII

In this work we introduce the design, optimization, simulation and experimental characterization results of a 30 -to-1 wavelength multiplexer for a Distributed Feedback Quantum Cascade Laser (DFB QCL) laser array operating in the 7-8.5 μm (mid-long) infrared (IR) range based on an Echelle mirror using a dual Rowland circle grating scheme. This design is proposed in order to achieve a continuous tuning range overcoming the limited tunability of individual QCLs. The design is based on a DFB-QCL array with wavelength spacing of 0.05 μm, aiming to reducing coupling between the slab waveguides to a minimum.

We discuss the design parameters such as the order of diffraction, the operation wavelength range in the slab waveguides and the position of both the input and output waveguides are optimized for obtaining higher output power in the overall wavelength

range of the multiplexer device than in a single Rowland circle grating scheme, providing an improvement in channel transmission.

Other design characteristics, such as the structure scalability and reduction in size for these devices are considered and studied, including the input/output waveguide optimization as a function of parameters such as waveguide width, etching depth and wavelength.

A systematic process is presented for all steps in the design of these devices, comparing both simulated and experimental results, placing them as suitable options when compared to other IR multiplexer schemes in terms of size and transmission.

Advances toward monolithic broadly-tunable QCL sources – Invited Paper

Autores: M. Carras, G. Maisons, B. Simozrag, V. Trinite, M. Brun, P. R. Labeye, S. Nicoletti, F. Boulila, L. J. Orbe, G. Carpintero

SPIE PHOTONICS WEST, Proc. SPIE 8993-43 Quantum Sensing and Nanophotonic Devices XI / 2014

Annexes

Annex A - Quantum cascade Lasers

Quantum cascade lasers (QCLs) are semiconductor lasers that emit in the mid- to far-infrared portion of the electromagnetic spectrum. QCLs are unipolar and laser emission is achieved through the use of intersubband transitions in a repeated stack of semiconductor multiple quantum well heterostructures [1] .

The operation of these devices differs from ordinary semiconductor diode lasers. In a diode laser transitions occur between the conduction band and the valence band of the semiconductor material. In contrast, in a QCL the lasing transition occurs between states within a given quantum well, consisting of a periodic series of thin layers of varying material composition forming a superlattice, which introduces a varying electric potential across the length of the device, meaning that there is a varying probability of electrons occupying different positions over the length of the device [2] . This is referred to as one-dimensional multiple quantum well confinement and leads to the splitting of the band of permitted energies into a number of discrete electronic subbands.

By suitable design of the layer thicknesses it is possible to engineer a population inversion between two subbands in the system which is required in order to achieve laser emission [1] , and since the position of the energy levels in the system is primarily determined by the layer thicknesses and not the material, it is possible to tune the emission wavelength of QCLs over a wide range in the same material system. In a unipolar QCL, once an electron has undergone an intersubband transition and emitted a photon in one

period of the superlattice, it can tunnel into the next period of the structure where another photon can be emitted.

This proves as an advantage, as this construction scheme allows for the electron responsible for the emission of the photon to tunnel into the next quantum well, and as a result, multiple photons can be generated by a single electron, increasing their efficiency, hence the naming [1] . A visualization of the comparison between interband transitions for conventional semiconductor lasers and quantum cascade structures is shown in Figure A.1.

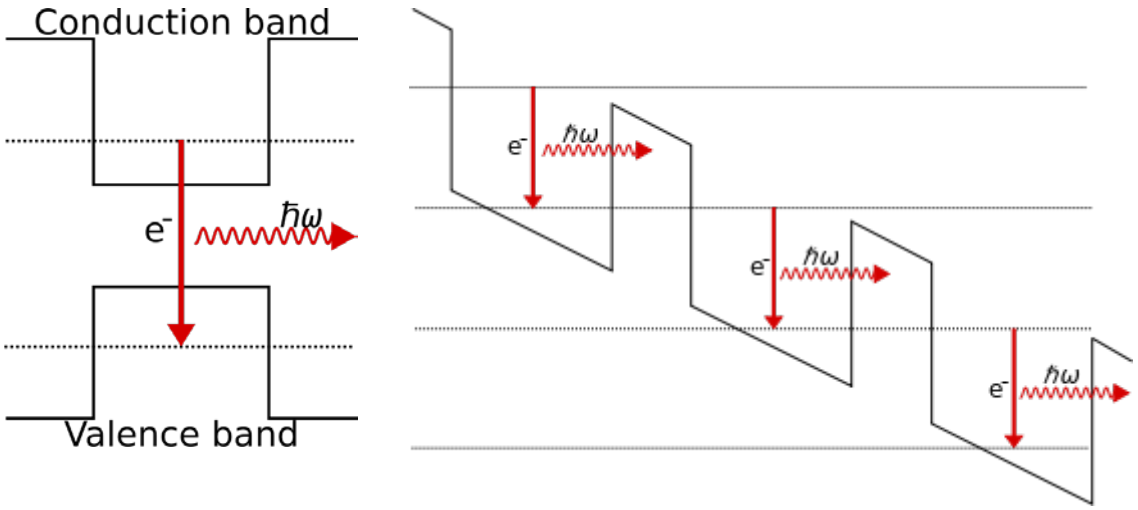

Figure A.1. Interband transitions in conventional semiconductor laser (left). Quantum cascade structure showing the tunneling effect of the electrons to successive periods of the structure

Quantum well engineering makes possible the design of QCLs with wavelengths as short as 2.75 μm[3] [4] and as long as 161 μm (1.9 THz)[5] [6] . Special interest is shown for the mid-infrared (2.5 to 25 μm)[7] and the Terahertz spectrum (60 to 150 μm).

Annex B - Light propagation in semiconductors

Optical confinement of light can be defined as when the light gets "trapped" when propagating through a medium of a certain refractive index which is embedded or surrounded by a different medium of lower refractive index. As this effect facilitates the confinement of light it can be exploited to fabricate guides that transport light from one end to another. An optical waveguide is then defined using the same description as a light conduit consisting of a slab, strip or cylinder of dielectric material surrounded by another dielectric material of lower refractive index [8] known as the cladding. The light propagates through the inner medium material without radiating into the surrounding medium material [9] .

Light propagation in semiconductor materials is the basis for all optical integration, even though the composition and optical properties of each vary from one to another, as well as their overall effect when in combination with other materials. In order to study those properties we the first step is to describe light propagation in the form of guided electromagnetic waves while traveling through a homogeneous medium.

Saleh and Teich [10] present an approach based on Maxwell's equations where $J = \rho = 0$. The proposed equations for a harmonic field become

$$\nabla \times E = i\omega B \qquad \text{Eq. B.1} \quad \text{(a)}$$

$$\nabla \times H = -i\omega D \qquad \text{Eq. B.1} \quad \text{(b)}$$

$$\nabla \cdot \mathrm{B} = 0 \qquad \text{Eq. B.1} \quad \text{(c)}$$

$$\nabla \cdot \mathrm{D} = 0 \qquad \text{Eq. B.1} \quad \text{(d)}$$

Given that the propagation medium is homogenous the wave plane wave solutions can be expressed as a function of the wave vector $\mathbf{k}$ as $e^{i\mathbf{k}r}$. Since all complex field vectors ($\mathbf{E}$, $\mathbf{H}$, $\mathbf{B}$ and $\mathbf{D}$) present spatial dependence $e^{i\mathbf{k}r}$, the basic relations for plane wave propagation in source-free homogeneous media can be expressed as

$$\mathrm{k} \times E = \omega B \qquad \text{Eq. B.2} \quad \text{(a)}$$

$$\mathrm{k} \times H = -\omega D \qquad \text{Eq. B.2} \quad \text{(b)}$$

$$\mathrm{k} \cdot \mathrm{B} = 0 \qquad \text{Eq. B.2} \quad \text{(c)}$$

$$\mathrm{k} \cdot \mathrm{D} = 0 \qquad \text{Eq. B.2} \quad \text{(d)}$$

Where we see that the wave vector $\mathbf{k}$ is always perpendicular to $\mathbf{B}$ and $\mathbf{D}$, moving at an angular frequency $\boldsymbol{\omega}$, but it is not possible to assert its perpendicularity to $\mathbf{H}$ and $\mathbf{E}$ unless the propagation media is isotropic.

Light propagation in isotropic media

In any given isotropic media, the premise is that $\mathbf{D}$ is always parallel to $\mathbf{E}$ $(D = \varepsilon E)$, and $\mathbf{B}$ is parallel to $\mathbf{H}$ $(B = \mu H)$, henceforth the equations satisfied by plane waves in isotropic medium become

$$\mathrm{k} \times E = \omega \mu H \qquad \text{Eq. B.3} \quad \text{(a)}$$

$$\mathrm{k} \times H = -\omega \varepsilon E \qquad \text{Eq. B.3} \quad \text{(b)}$$

$$\mathrm{k} \cdot \mathrm{H} = 0 \qquad \text{Eq. B.3} \quad \text{(c)}$$

$$\mathrm{k} \cdot \mathrm{E} = 0 \qquad \text{Eq. B.3} \quad \text{(d)}$$

Where $\boldsymbol{\varepsilon}$ is the electric permittivity of the medium and $\boldsymbol{\mu}$ is the magnetic permeability of the medium.

Exploiting the perpendicularity of the vectors $\mathbf{E}$, $\mathbf{H}$ and $\mathbf{k}$ we can obtain the definition of the wave number $\boldsymbol{k}$ by following the relations

$$\mathrm{k} \times (\mathrm{k} \times E) = \omega \mu k \times H = (\mathrm{k} \cdot E)\mathrm{k} - k^2 E = -k^2 E \qquad \text{Eq. B.4} \quad \text{(a)}$$

$$-k^2 E = \omega \mu k \times H = \omega \mu (-\omega \varepsilon E) \qquad \text{Eq. B.4} \quad \text{(b)}$$

Obtaining as a result

$$(k^2 - \omega^2 \mu \varepsilon) E = 0 \qquad \text{Eq. B.4} \quad \text{(c)}$$

From where the solution $k^2 = \omega^2 \mu \varepsilon$ describes the dispersion relation in an isotropic medium. If the material definition of the refractive index of any material is given by the equation

$$n = \sqrt{\frac{\mu\varepsilon}{\mu_0\varepsilon_0}} \qquad \text{Eq. B.5}$$

Where $\boldsymbol{\mu_0} = 4\pi \times 10^{-7}\ H/m$ and $\boldsymbol{\varepsilon_0} = 8.854 \times 10^{-12}\ F/m$; and the speed of light in free space is described as $c = 1/\sqrt{\mu_0\varepsilon_0} \simeq 3 \times 10^8\ m/s$ we have

$$k = \frac{\omega}{c}n \qquad \text{Eq. B.6}$$

Where the wavenumber $\boldsymbol{k}$ is redefined as a relation to the speed of light through a medium with a refractive index **n**

Light propagation through planar-mirror waveguides

In order to translate the light propagation theory into practice, a good first approach is the study of planar-mirror waveguides, made of two parallel infinite planar mirrors separated by a distance **d** which are assumed ideal (they reflect light without loss), Figure B.1. A light ray is then applied in the z axis and it reflects in-between the mirrors while being guided along that plane.

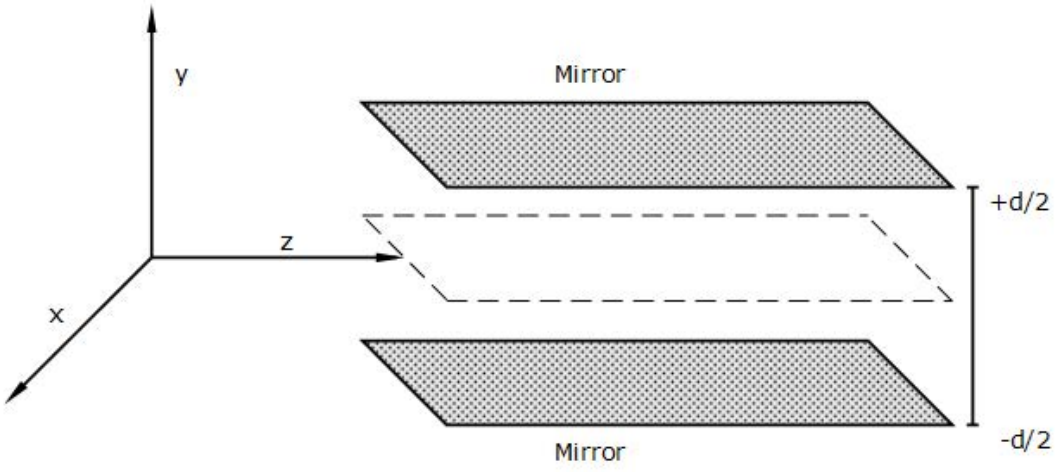

Figure B.1. Scheme of a planar mirror waveguide

The most basic approach to introduce electromagnetic analysis is to associate with each optical ray being propagated a Transverse Electromagnetic (TEM) plane wave [11] . The total electromagnetic field can be defined as the sum of all the plane waves being propagated in the same direction. The basic schematic of this model is shown in Figure B.2.

Considering a monochromatic TEM plane wave of wavelength $\lambda = \lambda_0/n$, wavenumber $k = k_0 n$, where $k_0 = \omega_0/c_0$ and phase velocity $c = c_0/n$, where **n** is the refractive index of the medium in-between the mirrors. Since the electric field is parallel to the mirror, the amplitude and polarization of such are not changed.

Imposing a self-consistency condition of requiring that as the wave reflects twice, it reproduces itself, so that we have only two distinct plane waves. Any field that can satisfy this condition is called **eigenmode**, or waveguide mode. **Modes** are fields that maintain the same transverse distribution and polarization at all distances along the waveguide axis.

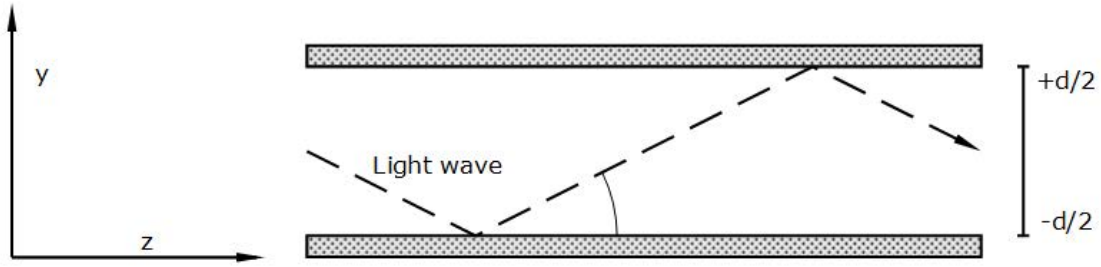

Figure B.2. Light reflections inside a planar mirror waveguide

The self consistency condition is therefore satisfied only for certain angles $\theta = \theta_m$ satisfying

$$\sin\theta_m = m\frac{\lambda}{2d} \qquad \text{Eq. B.7}$$

Where **m** corresponds to an angle $\boldsymbol{\theta_m}$and the corresponding field is known as the $\boldsymbol{m}$th mode; however, the maximum allowed value of m is the greatest integer smaller than $2d/\lambda$, therefore we can define the number of modes of the waveguide as.

$$.M = \frac{2d}{\lambda} \qquad \text{Eq. B.8}$$

The number of modes increases with the distance in-between the mirrors (**d**) and the **cutoff wavelength** is defined as longest wavelength that can be propagated through the medium, and is defined as $\lambda_{max} = 2d$.

The guided wave is composed of two different plane waves traveling at angles $\pm\theta$ within the z-axis in the y-z plane, therefore their wavevectors have components $(0,k_y,k_z)$ and $(0,-k_y,k_z)$. Their propagation constant can be defined then as $\beta = k_z = \mathrm{k}\cos\theta$, therefore $\beta_m = k\cos\theta_m$. Using trigonometric identities we obtain then the relation

$$\beta_m^2 = k^2(1-\sin^2\theta_m) = k^2 - \frac{m^2\pi^2}{d^2} \qquad \text{Eq. B.9}$$

Higher-order modes are propagated through the medium with smaller propagation constants.

Light propagation through planar dielectric waveguides

Planar mirror waveguides are useful to understand the basic concepts of the propagation of electromagnetic waves, however, their fabrication is extremely complex and therefore their use is limited. A planar dielectric waveguide is a slab of dielectric material surrounded by other material of lower refractive indices; the basic symmetric dielectric slab waveguide scheme is composed by a slab or "core" of width d and refractive index n_1 and surrounded by a cladding and a substrate of a smaller refractive index n_2, Figure B.3. The main difference regarding planar mirror waveguides is that the existence of propagating modes outside of the core is mathematically possible [8] [12] .

To determine such waveguide modes, we part from the basic geometry showing wave propagation in the z-axis and following the development of solutions to Maxwell's equations [9] . A solution to this problem is given in terms of Transverse-Electric-Magnetic (TEM) plane waves as they propagate within the model.

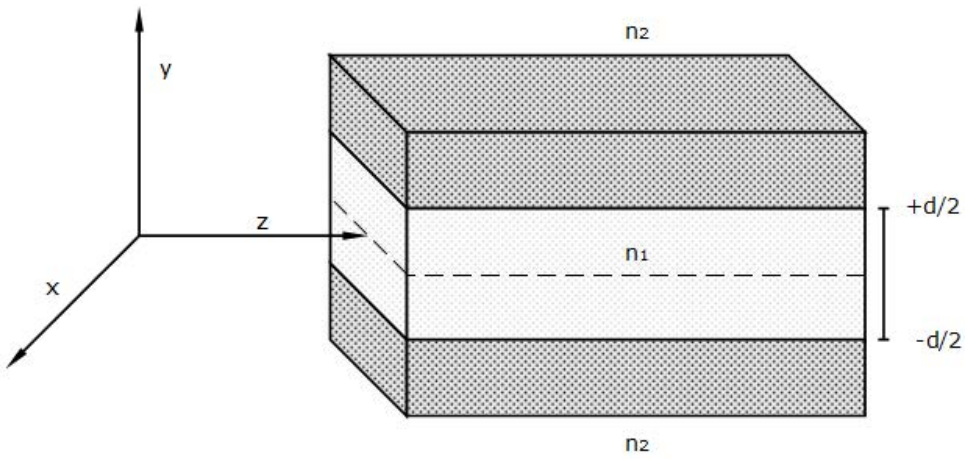

Figure B.3. Scheme of a dielectric waveguide

In analogy to the planar mirror model we can also define the formulation for the number of modes, however, the introduction of different diffraction indexes have to be taken into account, therefore

$$M = 2\frac{d}{\lambda_0}NA \qquad \text{Eq. B.10}$$

$$NA = (n_1^2 - n_2^2)^{1/2} \qquad \text{Eq. B.11}$$

Where NA is the **numerical aperture** of the waveguide.

The wavenumber ***k*** can also be defined as a complex number by describing it in terms of the complex refractive index $\tilde{n} = n(\omega) + i\kappa(\omega)$, where **n** and **κ** represent the dispersive effects of the real and the imaginary parts for any given material. By using this concept we can relate it to Equation B.6 and express it in terms of a complex refractive index.

$$k = \frac{\omega}{c}\tilde{n}(\omega) = \frac{\omega}{c}[n(\omega) + i\kappa(\omega)] \qquad \text{Eq. B.12}$$

Where the imaginary part of the complex term is half of the absorption coefficient **α**

$$\alpha(\omega) = 2 \cdot Im(k) = 2\frac{\omega}{c}\kappa(\omega) = \frac{4\pi}{\lambda}\kappa(\omega) \qquad \text{Eq. B.13}$$

However, so far we have just described the associated characteristics of a planar dielectric waveguide regarding the basic planar mirror model; the description of the optical modes had to be taken as an expansion of the Maxwell's equations satisfied by plane waves in isotropic medium. Henceforth, we can obtain the solutions for the fields everywhere

from Equation B.4c, those solutions correspond to a waveguide mode with all of the boundary conditions satisfied [13] ,[14] .

Chuang states those solutions as a function of the polarization. For TE polarization, the electric field only has an Ey component

$$E = \hat{u}_y E_y \qquad (E_x = E_z = 0) \qquad \text{Eq. B.14} \quad \text{(a)}$$

$$H = \frac{1}{i\omega\mu_i}\left(-\hat{u}_x i k_z E_y + \hat{u}_z \frac{\partial}{\partial x} E_y\right) \qquad \text{Eq. B.14} \quad \text{(b)}$$

$$\mu_i = \mu_1 inside\ the\ waveguide, \mu_i = \mu\ outside$$

$$\left(\frac{\partial^2}{\partial x^2} + \frac{\partial^2}{\partial z^2} + \omega^2\mu\varepsilon\right) E_y \qquad \text{Eq. B.14} \quad \text{(c)}$$

Where $\hat{\mathbf{u}}_\mathbf{k}$ is a unitary vector pointing to a direction k. The solutions to these equations have to be divided into even and odd modes.

TE even modes

$$E_y = C_1 e^{ik_z z} \begin{cases} \cos\left(\frac{d}{2}\right) e^{-\alpha\left(x-\frac{d}{2}\right)} & x \geq \frac{d}{2} \\ \cos k_x x & |x| \leq \frac{d}{2} \\ \cos\left(\frac{d}{2}\right) e^{\alpha\left(x+\frac{d}{2}\right)} & x < \frac{d}{2} \end{cases} \qquad \text{Eq. B.14} \quad \text{(d)}$$

TE odd modes

$$E_y = C_1 e^{ik_z z} \begin{cases} \sin\left(k_x \frac{d}{2}\right) e^{-\alpha\left(x-\frac{d}{2}\right)} & x \geq \frac{d}{2} \\ \sin k_x x & |x| \leq \frac{d}{2} \\ -\sin\left(k_x \frac{d}{2}\right) e^{\alpha\left(x+\frac{d}{2}\right)} & x < \frac{d}{2} \end{cases} \qquad \text{Eq. B.14} \quad \text{(e)}$$

Where

$$C_1 = \left(\frac{4\omega\mu_1}{k_z d}\right)^{1/2} \Big/ \left[1 + \frac{\sin k_x d}{k_x d} + \left(\frac{\mu_1}{\mu}\right)\left(\frac{2}{\alpha d}\right) cos^2(k_x d/2)\right]^{1/2}. \qquad \text{Eq. B.14} \quad \text{(f)}$$

For TM polarization, we can apply the duality principle and replace the field solutions $\mathbf{E}$ and $\mathbf{H}$ of the TE modes by $\mathbf{H}$ and $-\mathbf{E}$ respectively, $\boldsymbol{\mu}$ by $\boldsymbol{\varepsilon}$ and $\boldsymbol{\varepsilon}$ by $\boldsymbol{\mu}$; this is because since the boundary conditions in which the tangential components of the electric and magnetic fields are continuous across the dielectric interfaces and stay the same, the simultaneous replacements also give solution to Maxwell's equations.

$$H = \hat{u}_y H_y \qquad (H_x = H_z = 0) \qquad \text{Eq. B.15} \quad \text{(a)}$$

$$E = \frac{1}{i\omega\varepsilon_i}\left(-\hat{u}_x i k_z H_y + \hat{u}_z \frac{\partial}{\partial x} H_y\right) \qquad \text{Eq. B.15} \quad \text{(b)}$$

$$\varepsilon_i = \varepsilon_1 inside\ the\ waveguide, \varepsilon_i = \varepsilon\ outside$$

$$\left(\frac{\partial^2}{\partial x^2} + \frac{\partial^2}{\partial z^2} + \omega^2\mu\varepsilon\right) E_y \qquad \text{Eq. B.15} \quad \text{(c)}$$

TM even modes

$$H_y = C_1 e^{ik_z z} \begin{cases} \cos\left(k_x \frac{d}{2}\right) e^{-\alpha\left(x - \frac{d}{2}\right)} & x \geq \frac{d}{2} \\ \cos k_x x & |x| \leq \frac{d}{2} \\ \cos\left(k_x \frac{d}{2}\right) e^{\alpha\left(x + \frac{d}{2}\right)} & x < \frac{d}{2} \end{cases} \qquad \text{Eq. B.15} \quad \text{(d)}$$

TM odd modes

$$H_y = C_1 e^{ik_z z} \begin{cases} \sin\left(k_x \frac{d}{2}\right) e^{-\alpha\left(x - \frac{d}{2}\right)} & x \geq \frac{d}{2} \\ \sin k_x x & |x| \leq \frac{d}{2} \\ -\sin\left(k_x \frac{d}{2}\right) e^{\alpha\left(x + \frac{d}{2}\right)} & x < \frac{d}{2} \end{cases} \qquad \text{Eq. B.15} \quad \text{(e)}$$

Where

$$C_1 = \left(\frac{4\omega\varepsilon_1}{k_z d}\right)^{1/2} \Big/ \left[1 + \frac{\sin k_x d}{k_x d} + \left(\frac{\varepsilon_1}{\varepsilon}\right)\left(\frac{2}{\alpha d}\right) cos^2(k_x d/2)\right]^{1/2}. \qquad \text{Eq. B.15} \quad \text{(f)}$$

However, as we can observe, this model proposes the solutions for all of the modes of a certain waveguide plane, including those outside the center of the structure, which are by definition "not guided". A graphic representation of the guided modes can be related to a propagation representation of the electric and magnetic fields, as shown in Figure B.4.

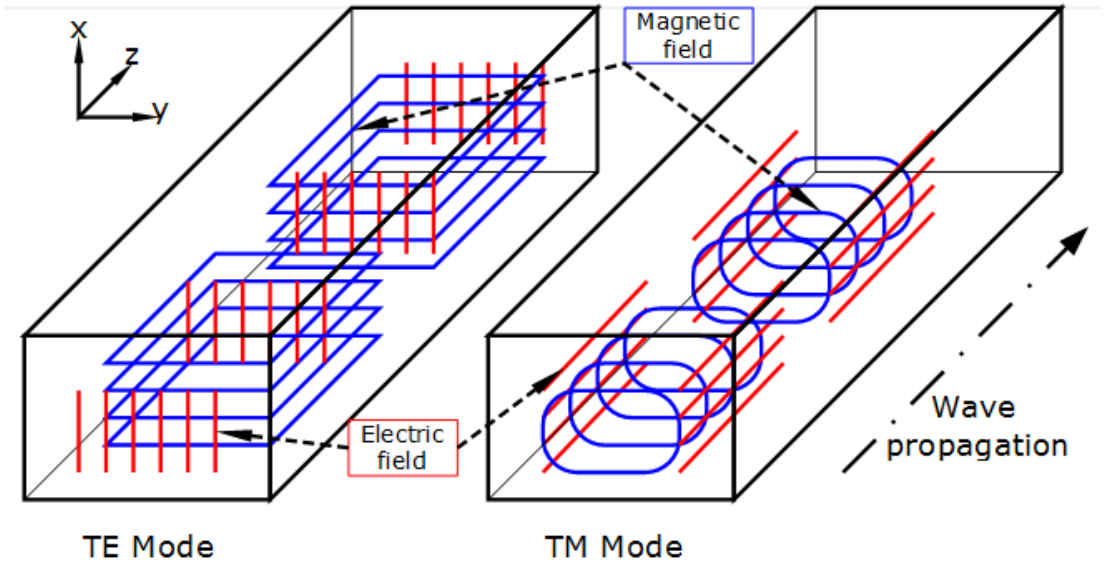

Figure B.4. Propagation of the TE and TM modes through a dielectric waveguide

Annex C - Numerical models for the simulation of optical structures

Finite-Difference Time-Domain Method

The finite-difference time-domain (FDTD) method is seen as the most popular numerical technique especially because of its flexibility in handling material dispersion [15] [16] as well as heterogeneous structures and anisotropic materials.

This method is a grid-based differential numerical modeling method in which the time-dependent Maxwell's equations are discretized using central-difference approximations to the space and time partial derivatives. This approach allows for the user to discretize a desired optical structure into space differentials (grid) Figure C.1.The resulting equations are solved so that the electric field vector components in a plane or a space are solved at a given instant in time; after that, the magnetic field vector components of the same plane or space are solved for the next instant in time; this process is repeated until the steady-state electromagnetic field behavior is reached.

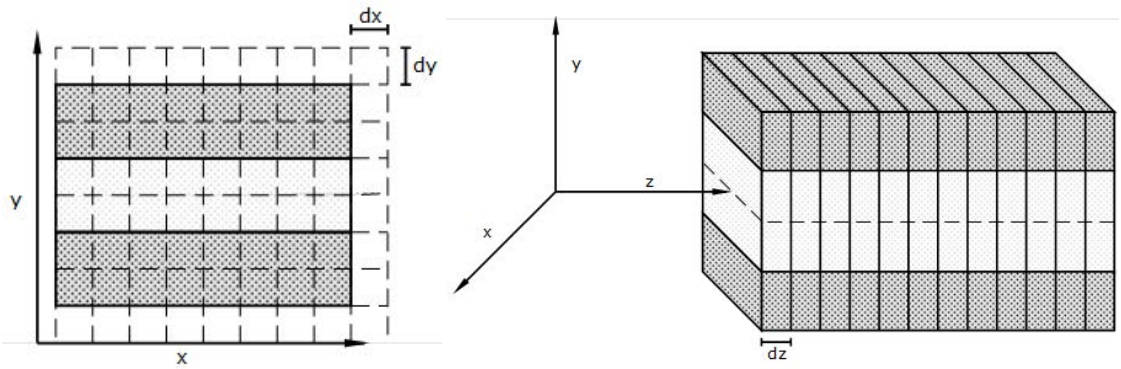

Figure C.1. Discretization of a dielectric waveguide

The numerical calculations for mode propagation are done by adding the waveguide modes in an individual form, so that each waveguide mode takes the form

$$\begin{aligned} \hat{u} \cdot E\,(x,y,z) &= \hat{u} \cdot A(x,y)e^{ikz} = M_{te}(x,y)e^{ikz} \\ \hat{u} \cdot H(x,y,z) &= \hat{u} \cdot B(x,y)e^{ikz} = M_{tm}(x,y)e^{ikz} \end{aligned} \qquad \text{Eq. C.1} \quad \text{(a)}$$

$$\begin{aligned} \frac{\partial\,(\hat{u} \cdot E)}{\partial z} &= M_{te}(x,y)\frac{\partial}{\partial z}(e^{ikz}) + e^{ikz}\frac{\partial}{\partial z}\big(M_{te}(x,y)\big) \\ \frac{\partial\,(\hat{u} \cdot E)}{\partial z} &= ikM_{te}(x,y)e^{ikz} = ik(\hat{u} \cdot E) \\ \frac{\partial(\hat{u} \cdot H)}{\partial z} &= M_{tm}(x,y)\frac{\partial}{\partial z}(e^{ikz}) + e^{ikz}\frac{\partial}{\partial z}(M_{tm}(x,y)) \\ \frac{\partial\,(\hat{u} \cdot H)}{\partial z} &= ikM_{te}(x,y)e^{ikz} = ik(\hat{u} \cdot H) \end{aligned} \qquad \text{Eq. C.1} \quad \text{(b)}$$

Simplifying the equations we obtain the relation $\frac{\partial}{\partial y} = ik$, which allows us to obtain the reduction for the Maxwell's Equation for the fields in every direction over the propagation axis z as a function of the electric permittivity and the magnetic permeability. Also, by introducing the effective refractive index of the studied geometry we can introduce Equation B.12 and normalize the grid in the x-axis direction as a function of the complex propagation constant k, so that $x' = k_0 x$

For the Ez modes

$$\begin{aligned} M_{te_x} = M_{te_z} = M_{tm_y} = 0 \\ \frac{\partial(M_{tm_z})}{\partial x} - ikM_{tm_x} = i\omega\frac{\varepsilon_{yy}}{c_0}M_{te_y} \\ ikM_{te_y} = -i\omega\frac{\mu_{xx}}{c_0}M_{tm_x} \\ -\frac{\partial(M_{te_y})}{\partial x} = -i\omega\frac{\mu_{zz}}{c_0}M_{tm_z} \end{aligned} \quad \rightarrow \quad \begin{aligned} \frac{\partial(M_{tm_z})}{\partial x'} - in_{eff}M_{tm_x} = i\varepsilon_{yy}M_{te_y} \\ n_{eff}M_{te_y} = -i\mu_{xx}M_{tm_x} \\ \frac{\partial(M_{te_y})}{\partial x'} = i\mu_{zz}M_{tm_z} \end{aligned} \qquad \text{Eq. C.2} \quad \text{(a)}$$

For the Hz modes

$$M_{tm_x} = M_{tm_z} = M_{te_y} = 0 \qquad \text{Eq. C.2} \quad \text{(b)}$$

$$\frac{\partial(M_{te_z})}{\partial x} - ikM_{te_x} = -i\omega\frac{\mu_{yy}}{c_0}M_{tm_y} \quad \rightarrow \quad \frac{\partial(M_{te_z})}{\partial x'} - in_{eff}M_{te_x} = i\mu_{yy}M_{tm_y}$$

$$ikM_{tm_y} = i\omega\frac{\varepsilon_{xx}}{c_0}M_{te_x} \quad \rightarrow \quad n_{eff}M_{tm_y} = i\varepsilon_{xx}M_{te_x}$$

$$-\frac{\partial(M_{tm_y})}{\partial x} = i\omega\frac{\varepsilon_{zz}}{c_0}M_{t\varepsilon_z} \quad \rightarrow \quad -\frac{\partial(M_{tm_y})}{\partial x'} = i\varepsilon_{zz}M_{te_z}$$

The magnitude of the TE and TM modes can be calculated using these set of equations regarding the **x** and **y** axis; the propagation axis z is already taken into account, as it is affected by the same effects as the propagation constant for a certain mode describes. The propagation effects can then be expanded for modal propagation in the form

$$\hat{u} \cdot T_e(x,y,z) = \hat{u}_x \cdot M_{te_x} + \hat{u}_y \cdot M_{te_y} + \hat{u}_z \cdot M_{te_z} \qquad \text{Eq. C.3} \quad \text{(a)}$$

$$\hat{u} \cdot T_m(x,y,z) = \hat{u}_x \cdot M_{tm_x} + \hat{u}_y \cdot M_{tm_y} + \hat{u}_z \cdot M_{tm_z}$$

The vectorial expansion can be presented considering the directional components so that the specific weight of each vector is accounted. A graphic representation of the grid and the spatial coordinates is presented at Figure C.2. The final equation set allows for the application of the method in the entire designed structure as a set of "slices" of the TE and TM fields over the x-y plane; the z-axis is introduced as the propagation effects, directly affected by the cumulated values of the propagating fields.

$$\hat{u} \cdot T_e(x_x, y_y, z_z) = \hat{u}_x M_{te_x}(x_x, 0,0) + \hat{u}_y M_{te_y}(0, y_y, 0) + \hat{u}_z M_{te_z}(0,0,z_z) \sum_1^z e^{ik(z-1)} \qquad \text{Eq. C.3} \quad \text{(b)}$$

$$\hat{u} \cdot T_m(x_n, y_n, z_n) = \hat{u}_x M_{tm_x}(x_x, 0,0) + \hat{u}_y M_{tm_y}(0, y_y, 0) + \hat{u}_z M_{tm_z}(0,0,z_z) \sum_1^z e^{ik(z-1)}$$

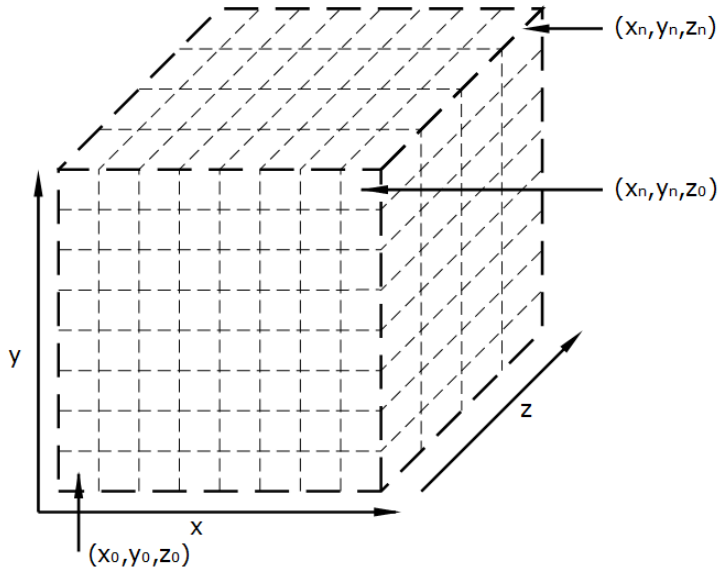

Figure C.2. Spatial grid model of the tridimensional space for modal propagation

Beam Propagation Method (BPM)

The beam propagation method (BPM) is an approximation technique for simulating the propagation of light in slowly varying optical waveguides. It is a split-step method in which an input field is propagated under scalar approach in alternating steps through a defined map of refractive index [17] .

The beam propagation method essentially decomposes a mode into a superposition of plane waves, each traveling in a different direction. These individual plane waves are propagated through a finite predetermined distance through the wave guide until the point where the field needs to be determined has arrived. At this point, all the individual plane waves are numerically added in order to get back the spatial mode.

The algorithm transports the optical fields within one propagation step from a transverse plane at the longitudinal coordinate **z** to a transverse plane at $z + \Delta z$, taking into account the variation in the refractive index between both planes.

The first step in the method is the transformation of the mode input field into angular spectrum. A propagation of the angular spectrum is performed using the Fourier transform up to $z + \Delta z$. Using the inverse Fourier transform the field returns to the position space, and the phase portrait is corrected according to the refractive index step. The output field is then used for the next step iteration in the method.

The entire process for a single iteration can be described by the following equations and it is done for both TE and TM modes.

$$I.\quad M_{Te,Tm}(a_x, a_y, z) = F\{M_{Te,Tm}(x, y, z)\} \qquad \text{Eq. C.4}$$

$$II.\quad M_{Te,Tm}(a_x, a_y, z + \Delta z) = M_{Te,Tm}(a_x, a_y, z + \Delta z)e^{\frac{i(a_x^2 + a_y^2)\Delta z}{2k_0}}$$

$$III.\quad M_{Te,Tm}(a_x, a_y, z + \Delta z) = F^{-1}\{M_{Te,Tm}(a_x, a_y, z + \Delta z)\}$$

$$IV.\quad M_{Te,Tm}(a_x, a_y, z + \Delta z) = M_{Te,Tm}(a_x, a_y, z + \Delta z)e^{i\Delta n k_0 \Delta z}$$

$$V.\quad M_{Te,Tm}(x, y, z) = M_{Te,Tm}(a_x, a_y, z + \Delta z)$$

Where a is the angular representation of the mode.

Film Mode Matching (FMM) Method

The Mode Matching Method models an arbitrary waveguide by a list of vertical slices, each uniform laterally, but composed vertically of a number of layers. A 2D mode is built up from the TE and TM 1D modes of each slice. The waveguide mode field T is expanded into a superposition of the TE and TM film modes of the planar slab waveguide in each slice. The amplitudes of the modes are then obtained by matching the field distributions and their normal derivative at each interface between the two adjacent slices [18] .

During the mode solving procedure, the mode profile at each rectangular sub-area is presented in the form

$$C^{(x_n,y_n)}(x,y) = \sum_{i=0}^{\infty}\left[\hat{u}_{h_i}^{(x_n)}(x)T_{sh_i}^{(x_n,y_n)}(y) + \frac{\partial}{\partial x}\hat{u}_{h_i}^{(x_n)}(x)T_{ah_i}^{(x_n,y_n)}(y)\right] + \sum_{i=0}^{\infty}\left[\hat{u}_{e_i}^{(x_n)}(x)T_{se_i}^{(x_n,y_n)}(y) + \frac{\partial}{\partial x}\hat{u}_{e_i}^{(x_n)}(x)T_{ae_i}^{(x_n,y_n)}(y)\right] \quad \text{Eq. C.5}$$

Where C represents any of the electrical or magnetic mode field components $E_xE_yE_zH_xH_yH_z$, following the previously used nomenclature, the superscripts x_n and y_n represent the x_n^{th} slice and the y_n^{th} layer, respectively, $T_{sp_i}^{(x_n,y_n)}(y)$ represents the symmetric ith-order film mode components in the rectangular sub-area (x_n, y_n).with TE or TM polarization (**p** stands for polarization and can take an **e** or an **h** value accordingly), and $F_{ap_i}^{(x_n,y_n)}(y)$ the anti-symmetric ones; $\hat{u}_{p_i}^{(x_n)}(x)$is the corresponding film mode amplitude in the x_n^{th} slice.

The symmetric and anti-symmetric modes (T) can be obtained from the wave equation of a multi layer slab dielectric waveguide, following the procedure as detailed in II.II.I.

The method is theoretically exact for an infinite number of 1D modes. The modeled area may be bound by either perfect metallic or magnetic walls or with periodic boundary conditions. The FMM Solver support polymer multi-layers (PMLs), impedance or transparent boundary conditions.

References

[1] Faist, J.; et al; "Quantum cascade laser". Science, Vol. 264, No. 5158, pg. 553, 22 Apr (1994)

[2] Kazarinov, R.F; Suris, R.A. (April 1971). "Possibility of amplification of electromagnetic waves in a semiconductor with a superlattice". Fizika i Tekhnika Poluprovodnikov 5 (4): 797–800

[3] Devonson, J.; Cathabard, O.; Baranov, A.N.; "InAs/AlSb quantum cascade lasers emitting at 2.75-2.95 μm," Appl. Phys. Lett.; vol. 91, pg. 251102 (2007), and "InAs/AlSb quantum cascade lasers emitting below 3 μm," J. Devenson, R. Teissier, O. Cathabard, and A.N. Baranov, Appl. Phys. Lett.; vol. 90, pg. 111118 (2009)

[4] Cathabard, O.; Teissier, R.; Devenson, J.; Moreno, J.C.; Baranov, A.N. "Quantum cascade lasers emitting near 2.6 μm". Applied Physics Letters 96 (14)

[5] Kumar, S.; Williams, B.S.; Hu, Q.; Reno, J.L.; "1.9 THz quantum-cascade lasers with one-well injector," Appl. Phys. Lett.; Vol. 88, pg. 121123 (2006)

[6] Walther, C.; Fischer, M.; Scalari, G.; Terazzi, R.; Hoyler, N.; Faist, J. "Quantum cascade lasers operating from 1.2 to 1.6 THz". Applied Physics Letters 91 (13)

[7] Razeghi, Manijeh (2009). "High-Performance InP-Based Mid-IR Quantum Cascade Lasers" (ABSTRACT). IEEE Journal of Selected Topics in Quantum Electronics 15 (3): 941–951

[8] Marcuse D.; "Theory of Dielectric Optic Waveguides," Academic, New York (1974)

[9] Born, M.; Wolf, E.; "Principles of Optics," Pergamon, Oxford UK (1975)

[10] Saleh, B. E. A.; Teich, M. C.; "Fundamentals of Photonics" Wiley, (2001)

[11] Chuang, S. L.; "Physics of Optoelectronic Devices," Wiley (1995)

[12] Snyder, A. W; Love, J. D.; "Optical Waveguide Theory," Chapman & Hall, London (1983)

[13] Yariv, A.; "Optical Electronics," 3rd Ed. Holt-Rinehart & Winston, New York (1985)

[14] Kong, J. A.; "Electromagnetic Wave Theory," Wiley, New York (1990)

[15] Zhao, Y.; Hao, Y.; "Finite-Difference Time-Domain Study of Guided Modes in Nano-Plasmonic Waveguides," Antennas and Propagation, IEEE Transactions on , vol.55, no.11, pp.3070,3077, Nov. (2007)

[16] Taflove, A.; "Computational Electrodynamics: The Finite Difference Time Domain Method. Norwood," MA: Artech House, (1995)

[17] Tsuji, Y.; Koshiba, M.; Takimoto, N.; "Finite element beam propagation method for anisotropic optical waveguides," Lightwave Technology, Journal of , vol.17, no.4, pp.723,728, Apr (1999)

[18] Sudbo, A. S.; "Film mode matching: a versatile numerical method for vector mode field calculations in dielectric waveguides," Pure Appl. Opt 2 211 (1993)